



Universiteit  
Leiden  
The Netherlands

## Applications of graphene in nanotechnology : 1D diffusion, current drag and nanoelectrodes

Vrbica, S.

### Citation

Vrbica, S. (2018, December 12). *Applications of graphene in nanotechnology : 1D diffusion, current drag and nanoelectrodes. Casimir PhD Series*. Retrieved from <https://hdl.handle.net/1887/68258>

Version: Not Applicable (or Unknown)

License: [Licence agreement concerning inclusion of doctoral thesis in the Institutional Repository of the University of Leiden](#)

Downloaded from: <https://hdl.handle.net/1887/68258>

**Note:** To cite this publication please use the final published version (if applicable).

Cover Page



Universiteit Leiden



The handle <http://hdl.handle.net/1887/68258> holds various files of this Leiden University dissertation.

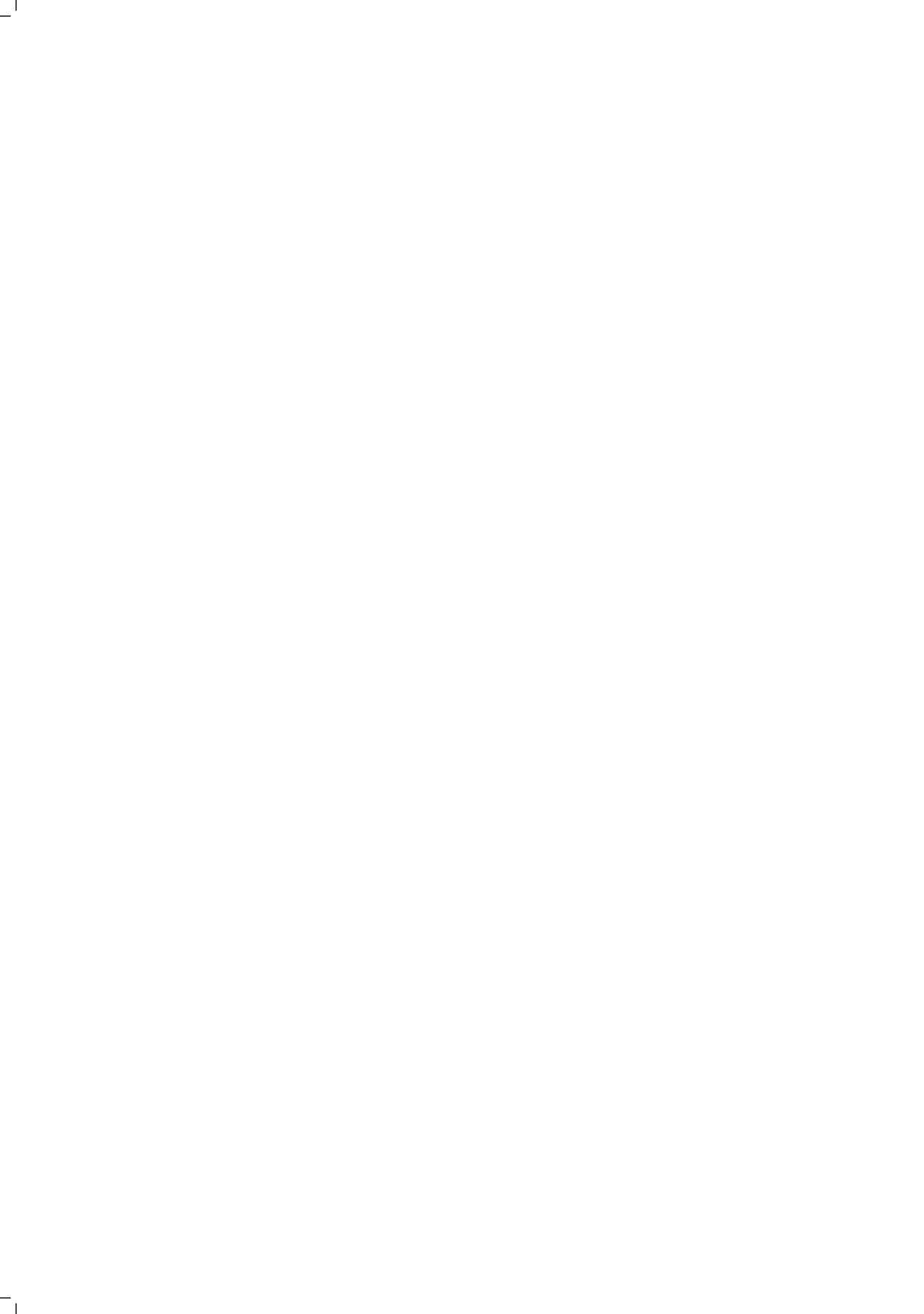
**Author:** Vrbica, S.

**Title:** Applications of graphene in nanotechnology : 1D diffusion, current drag and nanoelectrodes

**Issue Date:** 2018-12-12

# **APPLICATIONS OF GRAPHENE IN NANOTECHNOLOGY**

1D DIFFUSION, CURRENT DRAG AND NANOELECTRODES



# **APPLICATIONS OF GRAPHENE IN NANOTECHNOLOGY**

1D DIFFUSION, CURRENT DRAG AND NANOELECTRODES

**Proefschrift**

ter verkrijging van  
de graad van Doctor aan de Universiteit Leiden,  
op gezag van Rector Magnificus prof. mr. C.J.J.M. Stolker,  
volgens besluit van het College voor Promoties  
te verdedigen op woensdag 12 december 2018  
klokke 12.30 uur

door

**Sasha VRBICA**

geboren te Belgrado, Servië  
in 1986

Promotor: Prof. dr. J. M. van Ruitenbeek

Promotiecommissie: Prof. dr. A. F. Otte (Technische Universiteit Delft)  
Prof. dr. J. Repp (Universität Regensburg, Germany)  
Prof. dr. E. R. Eliel  
Prof. dr. ir. T. H. Oosterkamp  
Dr. G. Schneider

Casimir PhD series, Delft-Leiden 2018-44

ISBN 978-90-8593-374-8

An electronic version of this thesis can be found at  
<http://openaccess.leidenuniv.nl/>.

This work is part of the research program with project number 12QIM05, which is (partly) financed by the Netherlands Organisation for Scientific Research (NWO). The research of this thesis was performed at Leiden University, Delft University of Technology and University of Regensburg, Germany.



*Printed by:* Gildeprint

*Cover:* Designed by Boris Junkovic <http://borisjunkovic.artstation.com>  
Front cover photo illustrates gold STM tip and Co adatoms on GNRs grown on gold.  
Back cover photo illustrates two graphene nanoelectrodes (top) and a droplet of ionic liquid on graphene (bottom)

Copyright © 2018 by S. Vrbica

*To my family and Asuna*



# CONTENTS

<b>1</b>	<b>Introduction</b>	<b>1</b>
1.1	Outline of the thesis. . . . .	3
	References . . . . .	5
<b>2</b>	<b>One-dimensional diffusion of Co adatoms on graphene nanoribbons</b>	<b>7</b>
2.1	Introduction . . . . .	8
2.1.1	Non-conservative wind force and Berry force . . . . .	10
2.2	Graphene . . . . .	11
2.2.1	Graphene nanoribbons (GNRs) . . . . .	12
2.3	Scanning tunneling microscopy. . . . .	12
2.4	Atomic force microscopy and Kelvin probe force microscopy . . . . .	14
2.5	Experimental setups . . . . .	16
2.5.1	JEOL room-temperature UHV STM . . . . .	16
2.5.2	SPECS low-temperature UHV STM. . . . .	17
2.5.3	Createc low-temperature UHV STM . . . . .	17
2.6	First experiment: CVD grown graphene on Si/SiO <sub>2</sub> in room-temperature JEOL STM . . . . .	19
2.7	Second experiment: CVD grown graphene on Si/SiO <sub>2</sub> in low-temperature SPECS STM . . . . .	20
2.8	Third experiment: Graphene nanoribbons in low-temperature Createc STM. . . . .	22
2.8.1	Current-induced manipulation of Co adatoms. . . . .	25
2.8.2	Results . . . . .	30
2.8.3	Temperature-dependent diffusion measurements . . . . .	40
2.9	Discussion . . . . .	42
2.9.1	GNR conductance . . . . .	43
2.9.2	Hopping rate and diffusion barrier. . . . .	46
2.9.3	Vertical Co displacement. . . . .	47
2.9.4	Atom as a local thermometer? . . . . .	48
2.9.5	Co on Au(111) . . . . .	48
2.10	Conclusion & Outlook. . . . .	50
	References . . . . .	52

<b>3</b>	<b>Inducing voltage by moving a droplet of liquid along graphene</b>	<b>59</b>
3.1	Introduction . . . . .	60
3.1.1	Drawing potential and formation of a pseudocapacitor . . . . .	62
3.1.2	Sodium benzenesulfonate (NaBSA) and Benzenesulfonic acid (HBSA) . . . . .	64
3.2	Experimental details . . . . .	65
3.3	Results . . . . .	67
3.3.1	Sodium chloride (NaCl) . . . . .	67
3.3.2	Sodium benzenesulfonate (NaBSA) and Benzenesulfonic acid (HBSA) . . . . .	69
3.4	Discussion . . . . .	71
3.4.1	NaBSA . . . . .	71
3.4.2	HBSA . . . . .	72
3.4.3	Signal with deionized water . . . . .	74
3.5	Electromigration forces on a NaCl droplet . . . . .	77
3.5.1	Experimental setup and results . . . . .	77
3.5.2	Discussion . . . . .	78
3.6	Conclusion and Outlook . . . . .	80
	References . . . . .	81
<b>4</b>	<b>Dynamic tunneling junction at the intersection of two graphene edges</b>	<b>85</b>
4.1	Introduction . . . . .	86
4.2	Experimental techniques . . . . .	88
4.2.1	Atomic force microscopy (AFM) . . . . .	88
4.2.2	Scanning electron microscopy (SEM) . . . . .	89
4.2.3	Raman spectroscopy . . . . .	90
4.2.4	Electrical measurements . . . . .	90
4.2.5	Graphene film deposition . . . . .	91
4.3	First approach: breaking of polymer-covered graphene . . . . .	91
4.3.1	Results and discussion . . . . .	92
4.4	Second approach: breaking of bare graphene . . . . .	93
4.4.1	Results and discussion . . . . .	93
4.5	Third approach: plasma etching of suspended graphene . . . . .	95
4.5.1	Results and discussion . . . . .	96
4.5.2	Conclusion & Outlook . . . . .	101
	References . . . . .	103
<b>A</b>	<b>Appendix</b>	
	<b>Diffusion of Co adatoms</b>	<b>107</b>
A1	1D random walk probability distribution for Co on GNR . . . . .	107
A2	2D random walk probability distribution for Co on Au . . . . .	108

---

<b>B Appendix</b>	
<b>Graphene electrodes</b>	<b>111</b>
B1 Simmons model for symmetric barrier . . . . .	111
B2 Graphene-Gold Tunnel Junction . . . . .	112
B3 Tunneling junction controller. . . . .	114
B4 Sheet resistance and point contact resistance. . . . .	114
<b>Summary</b>	<b>116</b>
<b>Samenvatting</b>	<b>118</b>
<b>Curriculum Vitæ</b>	<b>120</b>
<b>List of Publications</b>	<b>121</b>
<b>Acknowledgements</b>	<b>122</b>



# 1

## INTRODUCTION

*A poet once said, "The whole universe is in a glass of wine." We will probably never know in what sense he meant that, for poets do not write to be understood. But it is true that if we look at a glass of wine closely enough, we see the entire universe.*

**R. P. Feynman [1]**

**T**he surface of the wine in a glass appears calm to the naked eye. However, if we magnify it a billion times, the world of tiny particles will emerge and we will see all kinds of atoms and molecules moving around. The world down there, at the atomic scale, is quite different from what we experience in our macroworld. If we try to apply classical mechanics to it, it will lead to contradictions between theory and experiment. Atomic phenomena are, instead, governed by the laws of quantum mechanics which has a lot of peculiar implications. It unifies the idea of particles and waves into one [2], and introduces the concept of the wave function. Events that are forbidden in classical mechanics have a finite probability of happening in quantum mechanics. One such example is the phenomenon of quantum tunneling, in which a particle overcomes a potential barrier that classically would not be allowed. This concept was utilized in 1981 to image single atoms and molecules with a technique known as scanning tunneling microscopy (STM) [3, 4]. This was the birth of nanotechnology - engineering, technology and science carried out at the nanoscale. Studying properties of matter at nanoscale can offer insights into fundamental principles and answer many important questions. Questions of this kind that we will be addressing in this thesis are "what is the exact nature of electromigration?" or "can a liquid flowing over the surface of a conductor generate a voltage?". Answers to

these questions will not only satisfy scientific curiosity, they will pave the way for inventions such as the creation of nanoelectrodes necessary for transport experiments through nanostructures, transport of nanomaterial or harvesting of electric power. Other practical applications may take advantage of enhanced properties of materials at the nanoscale (higher strength, lighter weight, better conductivity, atomic thickness, etc.) One of the most attractive approaches at this day and age is arguably the field of molecular electronics, which aims to incorporate molecular components as elements in electronic devices. Since the 1999 silicon industry has reduced channel length of transistor from 800 nm to 10 nm. The use of nanometer-sized molecules is therefore very appealing for electronic purposes. In 1974 a molecule was proposed that could work as a rectifier for the current when contacted by two electrodes [5]. Given the hard experimental task of fabricating molecular-scale electrodes, the first direct electrical measurement of a single molecule arrived only two decades later, when a current was sent through a single  $C_{60}$  molecule using an STM in UHV [6]. In 2000 researchers used the electromigration technique to sandwich the same molecule between two gold electrodes [7]. By applying a voltage on a third gate, the current between the source and the drain could be regulated, which resulted in the first single-molecule transistor. Applications could go as far as designing current-driven molecular motors or light-emitting gas sensors.

Advances in techniques for probing single molecules will also have a profound impact in the field of DNA sequencing. The sequence of the nucleobases in DNA encodes the genetic information, necessary for many applications in medicine, biology and other life sciences. With the motivation to find an efficient and inexpensive method for the whole genome analysis, the field of nanopore research has gained a lot of interest in the past two decades. In 1996, Kasianowicz *et al.* [8] first demonstrated translocation of single-stranded DNA molecules through a biological nanopore. DNA is a highly charged molecule, so it can be driven in a solution through the nanopore in a head-to-tail fashion by an electric field. When DNA enters the nanopore, the ionic current is reduced because the liquid volume that carries the ionic current is partially blocked by the translocating DNA. If the passage of each nucleotide of DNA produces a characteristic modulation of the ionic current, the sequence of current modulations would reflect the sequence of bases in DNA. However, single nucleotide discrimination could not be achieved with this technique because the ion-current blockades were found to be the consequence of several nucleotides (rather than a single nucleotide). Great effort has been made to find alternative materials to obtain thinner solid-state nanopores (such as SiN and  $SiO_2$ ) with higher spatial resolution, ultimately reaching single-base resolution. Graphene is considered to be the most promising candidate, as the membrane thickness (0.34 nm) is comparable to the height of a nucleotide, which makes single nucleotide discrimination possible [9]. Initial experiments [10, 11] provided proof of concept that it is possible to realize and use graphene nanopores for DNA translocation. Recently, it was proposed that characterization of single nucleotides in DNA

could be done via transverse electron tunneling through a nanogap between two graphene electrodes [12].

Despite significant progress during the last three decades, nanometer-scale electron transport still faces challenges. All current techniques for contacting molecules (STM, mechanically controllable break junction (lithographic and notched-wire), electromigration, ultra-high electron-beam lithography, focused ion-beam lithography, etc.) have some drawbacks. The biggest hindrance so far is the lack of reliable and easily reproducible way to create a gap between electrodes comparable to the size of the nanostructure itself.

## 1.1. OUTLINE OF THE THESIS

The initial motivation and the main aim of our research was electromigration at the atomic scale. Knowledge gained from such experiments would give clues to many unanswered questions about current-induced forces. Graphene on an insulating substrate was the first choice for the substrate material since the current would be confined within an atomic layer. Graphene on Si/SiO<sub>2</sub> that we initially used, however, came with a few limitations which inspired us to utilize graphene nanoribbons instead. Electromigration was also the motivation for the second part of the research presented in this thesis. The fact that drawing a droplet of ionic liquid along graphene induces a voltage [13] inspired us to ask the question: would it be possible to do the opposite? This approach required knowledge on adsorption of ions, formation of electric double layer and a pseudocapacitor, which was an incentive to expand the experiment and investigate voltages induced with several different types of ionic liquids. And as it often happens when doing scientific research, looking into certain problems sometimes leads to gaining knowledge (and interest) on concepts that are far from the initial objective. After doing many experiments with graphene, we were motivated to take it a step further and attempt to design atomically thin nanoelectrodes with a reproducible and reliable fabrication method. This project was particularly attractive in having a prospect for applications such as transport measurements on single molecules and sequencing of biopolymers.

The research in this thesis is accordingly split into three parts:

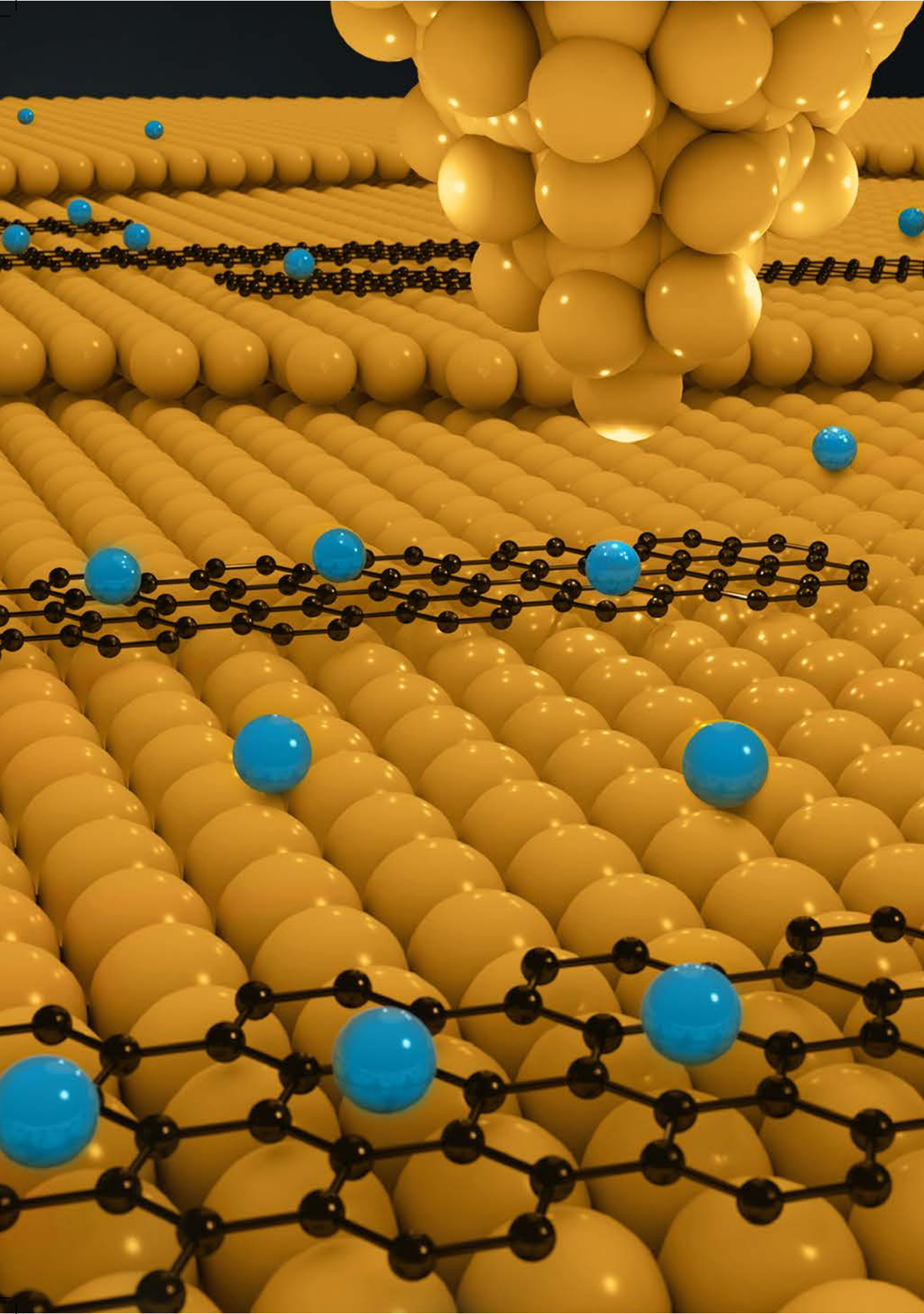
- **Chapter 2** (*One-dimensional diffusion of Co adatoms on graphene nanoribbons*) focuses on the investigation of electromigration forces at the scale of single atoms. This is realised with Co adatoms on graphene nanoribbons (GNR) on a Au(111) substrate with the use of an STM technique. We find that the presence of a potential barrier at the edges of GNR confines Co adatoms to a GNR and provides a path for one-dimensional diffusion. We study current-induced migration of single Co adatoms on GNR and on Au(111), and look for evidence of directional asymmetry related to the presence of electromigration forces.

Comparison of Co migration on GNR and on Au(111), together with results from temperature-dependent diffusion measurements, gives information on relative diffusion barriers of the two substrates.

- **Chapter 3** (*Inducing voltage by moving a droplet of liquid along graphene*) discusses the concept of an electrical double layer formed at the interface of a liquid and graphene on polyethylene terephthalate (PET), so-called "pseudocapacitor", which is responsible for a voltage signal induced in graphene when a droplet of liquid is set into motion. Experiments with different ionic liquids give information on the type of ions which dominantly adsorb to graphene. We find that certain types of ions adhere to graphene/PET so strongly that they leave the droplet and form a layer of charges on graphene. This is detected by the induced voltage signal when moving a droplet of distilled water along charged graphene surface. We find that the reason for this is the polarizability of water which has a large contribution to the voltage signal. Additionally, we attempt to induce motion of an ionic liquid droplet by applying a voltage across graphene, however no electromigration-induced motion of the droplet occurs. The reason lies in the additional layer of charges above the pseudocapacitor which neutralizes the charges, making the whole system neutral and unable to experience a net direct force. Our estimates show that the so-called *wind force* is much smaller than our detection limit.
- **Chapter 4** (*Dynamic tunneling junction at the atomic intersection of two twisted graphene edges*) demonstrates a method for creating two atomically thin graphene electrodes on Si/SiO<sub>2</sub>. All techniques used to characterize graphene edges (Raman spectroscopy, SEM, AFM and electrical measurements) unanimously confirm that graphene reaches up to the edge within the respective resolutions of each of the techniques. Using a modified STM and a twisted-sample approach, we created the first tunable tunneling nanogap between graphene electrodes. The nanogap size is detected with STM and can be tuned by moving the electrodes closer to each other by means of a piezo actuator. By bringing the crossed edges into contact we determine the single-atom contact resistance between the two graphene edges as  $11 \pm 3 \text{ k}\Omega$ , *i.e.* the quantum of resistance to within the experimental accuracy. This technique could, in principle, be used to probe single molecules via transverse electron tunneling and also achieve resolution of a single nucleotide in a DNA strand.

**REFERENCES**

- [1] Richard P. Feynman, R. B. Leighton, and M. Sands. *The Feynman Lectures on Physics*. Addison–Wesley, 1964.
- [2] Louis De Broglie. Recherches sur la Théorie des Quanta. *PhD Thesis*, 1924.
- [3] G. Binnig, H. Rohrer, Ch. Gerber, and E. Weibel. Surface studies by scanning tunneling microscopy. *Phys. Rev. Lett.*, 49:57–61, 1982.
- [4] G. Binnig and H. Rohrer. Scanning tunneling microscopy—from birth to adolescence. *Rev. Mod. Phys.*, 59:615–625, 1987.
- [5] A. Aviram and M. A. Ratner. Molecular rectifiers. *Chemical Physics Letters*, 29(2):277 – 283, 1974.
- [6] C. Joachim, J. K. Gimzewski, R. R. Schlittler, and C. Chavy. Electronic transparency of a single  $C_{60}$  molecule. *Phys. Rev. Lett.*, 74:2102–2105, 1995.
- [7] H. Park, J. Park, A. K. L. Lim, E. H. Anderson, A. P. Alivisatos, and P. L. McEuen. Nanomechanical oscillations in a single- $C_{60}$  transistor. *Nature*, 57:407, 2000.
- [8] J. J. Kasianowicz, E. Brandin, D. Branton, and D. W. Deamer. Characterization of individual polynucleotide molecules using a membrane channel. *Proc. Natl. Acad. Sci USA*, 93:13770–13773, 1996.
- [9] C. Dekker. Solid-state nanopores. *Nature Nanotechnology*, 2:209 – 215, 2007.
- [10] G. F. Schneider, S. W. Kowalczyk, V. E. Calado, G. Pandraud, H. W. Zandbergen, L. M. K. Vandersypen, and C. Dekker. DNA translocation through graphene nanopores. *Nano Letters*, 10(8):3163–3167, 2010.
- [11] S. Garaj, W. Hubbard, A. Reina, J. Kong, D. Branton, and J. A. Golovchenko. Graphene as a subnanometre trans-electrode membrane. *Nature*, 467:190 – 193, 2010.
- [12] S. J. Heerema and C. Dekker. Graphene nanodevices for dna sequencing. *Nature Nanotechnology*, 11:127 – 136, 2016.
- [13] J. Yin, X. Li, J. Yu, Z. Zhang, J. Zhou, and W. Guo. Generating electricity by moving a droplet of ionic liquid along graphene. *Nature Nanotech.*, 9:378–383, 2014.



# 2

## ONE-DIMENSIONAL DIFFUSION OF CO ADATOMS ON GRAPHENE NANORIBBONS

*It is well known that a flow of electrons through a conductor exerts a force on atoms, which can lead to their displacement. The induced motion of atoms includes two mechanisms: stochastic thermal motion from heat and directional motion from the electron current. In order to allow for a quantitative comparison to theory, the experiment needs to be conducted at the scale of single atoms or single molecules. Here we utilize graphene nanoribbons (GNR) on Au(111) as a current-carrying substrate to demonstrate one-dimensional diffusion of single Co adatoms, by applying voltage pulses with a tip of a low-temperature scanning tunneling microscope (STM). The motion of single adatoms is traced by scanning the surface before and after the voltage pulses. We show statistics for Co displacements for different voltage amplitudes and different initial tip-adatom distances. Our observations reveal that migration of Co is mainly a thermally driven effect. Finally, we compare the data for Co on GNR to the statistics for induced motion of Co on Au(111) and discuss temperature-dependent diffusion measurements, which give information on relative diffusion barriers on GNR and Au(111).*

---

The work is done in collaboration with - Irene Battisti<sup>1</sup>, Ranko Tošković<sup>2</sup>, Sander Otte<sup>2</sup>, Tobias Preis<sup>3</sup>, Nemanja Kocić<sup>3</sup>, Jascha Repp<sup>3</sup> and Jan M. van Ruitenbeek<sup>1</sup>

<sup>1</sup>Huygens-Kamerlingh Onnes Laboratorium, Leiden University, The Netherlands.

<sup>2</sup>Otte Lab, Delft University of Technology, The Netherlands.

<sup>3</sup>Repp group, University of Regensburg, Germany.

## 2.1. INTRODUCTION

A voltage applied across a metal or a semiconductor leads to the displacement of the atoms from their positions in a crystal lattice. This phenomenon is known as electromigration and was first reported in 1861, when Gerardin observed motion of mass in molten alloys of lead-tin and mercury-sodium [1]. Theoretical and experimental work has established that the driving force for electromigration can be separated into contributions arising from the electron wind force ( $\mathbf{F}_w$ ) and direct force ( $\mathbf{F}_d$ ) [2–5]:

$$\mathbf{F}_{em} = \mathbf{F}_d + \mathbf{F}_w = (Z - n l \sigma) e \mathbf{E} \quad (2.1)$$

where  $Z$  is the charge of the adsorbate,  $n$  is the electron density,  $l$  is the electron mean free path,  $\sigma$  is the scattering cross section,  $e$  is the electron charge and  $\mathbf{E}$  is the vector of external DC electric field. In this ballistic model a direct force is taken to be the applied electric field acting on the unscreened ion. The wind force is calculated from the rate of momentum transfer to the ion by the incident electrons. The electrons are treated in the free-electron gas model and the migrating ions are treated as impurity defects<sup>1</sup>. In this approximation, the direction of the wind force coincides with the direction of the electron current. If the net charge of the atom is positive, the direct force acts in the direction opposite of the electron current flow (Figure 2.1). The direction of atom diffusion will depend on the relative magnitudes of these two forces.

Electromigration is known to be the cause of failure of integrated circuits in microelectronics due to the formation of voids and hillocks in the wires [6–13], which poses a limitation on the maximum allowed power through the device (an example is shown in Figure 2.2(a) [13]). Numerous experiments have been performed on various current-carrying substrates in an attempt to learn more about the nature of the effect [14–17]. Initial experimental studies were limited to the collective motion of many atoms or the statistical description of large ensembles. Several decades of experimental work led to the utilization of electromigration for purification of bulk metals [18], controllable atomic-scale mass transport along the surface of a conduc-

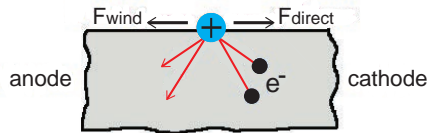


Figure 2.1: **Schematic illustration of two components of electromigration force.** Black balls represent electrons and a blue ball represents a positively charged atom.

<sup>1</sup> Note that this is a simplified model; more advanced descriptions can be found in the review by Sorbello[5]

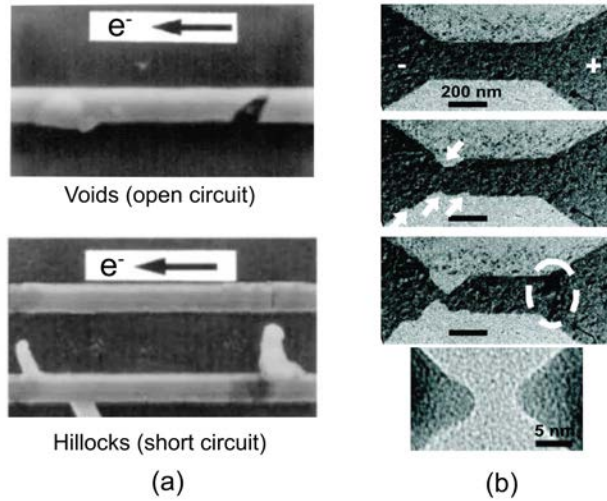


Figure 2.2: **Examples of destructive and constructive effects of electromigration.** (a) Scanning electron microscopy image of a circuit malfunction due to formation of voids (which lead to open circuit) and hillocks (lead to short circuit) in the wires [13]. (b) Electromigration-induced formation of gold nanoelectrodes [23]. After ramping a bias voltage across the 12 nm thick gold wire, voids form at the cathode side (arrows in the second image) while hillocks can be observed at the anode side (circle in the third image). Fourth image shows breaking of the device and formation of a 5 nm gap.

tor [19, 20] and the creation of nanoelectrodes for charge transport studies of individual molecules [21–26]. Figure 2.2(b) shows an example of electromigration-induced fabrication of gold nanoelectrodes on insulating  $\text{Si}_3\text{N}_4$  membranes [23]. The electromigration process is induced by ramping up a voltage across a 12 nm thick gold wire of 600 - 800  $\Omega$  resistance, and starts when the current is of the order of a few milliamperes. Voids form at the cathode side of the wire (indicated by arrows in the second panel) while hillocks are formed at the anode side (circled area in the third panel). The wire narrows down as a function of time and eventually breaks along the grain boundary with a final gap size of 5 nm (fourth panel).

Recent experiments have begun to address the process of electromigration at the nanoscale. Métois *et al.* [27] observed motion of silicon islands of a single atom height on flat terraces along or against the current direction. Tao *et al.* [28] have shown displacement of monoatomic islands of 2 - 50 nm radius on a single-crystal Ag(111) in the direction of electron flow when current is passed through the substrate. The atomic-scale fluctuations at a step edge on a Ag single crystal are directly correlated to the electron wind force [29]. Electromigration is also used to induce motion of the material deposited on the surface of the conductor. As the atoms on the surface (so-called “adatoms”) have smaller binding energy, they are most likely to be electromigrated. Regan *et al.* [19] have demonstrated reversible mass transport of

indium nanoparticles of 50 - 100 nm size along multiwalled carbon nanotubes which are connected to the metal tip on one side and to the sample holder on the other side. By applying a voltage of a few volts between the tip and the sample holder, a current of  $\sim 50 \mu\text{A}$  is established and mass transport between indium nanoparticles along the nanotubes is induced. In one of the first experiments involving single-atom electromigration, Braun *et al.* [30] showed that single Au and Ag adatoms on a Ni(111) surface can be moved by electromigration forces from a scanning tunneling microscope tip. Depending on the amplitude and polarity of the applied bias voltage, atoms are either pulled towards the tip or pushed away. In all the aforementioned experiments it was the voltage gradient, rather than the thermal gradient that determined the direction of mass transport.

Current theories of electromigration that aim for a microscopic description lack proper experiments for testing, and do not always successfully predict the extent and the direction of atom diffusion. Girard *et al.* [31] show in their theoretical study that certain types of adatoms (oxygen (O), fluorine (F) and nitrogen (N)) move under the influence of current-induced forces along a carbon nanotube in the direction of electron flow, while the other adatoms (boron (B) and carbon (C)) move in the opposite direction. The authors argue that there is a loose correlation between the atomic charge of the adsorbates and the direction and strength of the forces. O, F and N are negatively charged and the forces acting on them are in the direction of the electron flow, while B and C are positively charged and are pulled against the electron flow. This directionality indicates the dominance of the direct force over the wind force for these particular adsorbates. Solenov *et al.* [32], on the other hand, show that according to a tight binding model of electromigration of an adsorbate on graphene, the electron wind contribution dominates the electromigration force (except for the smallest  $Z$  or low conductivity). A deeper understanding of current-induced forces is necessary for a proper description of electromigration.

### 2.1.1. NON-CONSERVATIVE WIND FORCE AND BERRY FORCE

One of the holy grails of nanotechnology is the realization and utilization of autonomous nanomachines. A concept of a *molecular waterwheel* - a nanomotor driven by means of a direct current flow (in analogy to a waterwheel driven by a water flow) - is very appealing since it would not require externally supplied cyclic driving. In order to achieve this state, a non-conservative force is required to act between the non-equilibrium electron bath and ions comprising the nanoscale system so that net work is done per revolution. In a recent theoretical paper, Dundas *et al.* [33] analytically showed that the current-induced forces in atomic wires are non-conservative and can, in principle, be used to drive molecular machines. This gives a whole new outlook on the nature of electromigration. The concept of non-conservative wind force was further elaborated in works of several research groups [34–38]. Subsequently, Lü *et al.* [39] showed that interactions between the electrons and the lattice

give rise to another component of electromigration force, the so-called *Berry force*. This force originates from the change of phase (*Berry phase*) of the electronic wave functions due to the atomic motion, and acts just like a Lorentz force: it is perpendicular to the velocity of the ions and keeps them in periodic orbits. Both contributions to the force appear only when the electron gas is driven out of equilibrium (e.g. in the presence of the current flow) and can lead to instabilities (so-called *runaway modes*) that can effectively displace atoms. Truly microscopic experiments probing these forces at the scale of single atoms or molecules have not yet been conducted. The first promising data has been reported recently by Schirm *et al.* [40] on aluminum chains and by Sabater *et al.* [41] on Au and Pt atomic chains, both performed with mechanically controlled break junction techniques.

In the interest of giving a proper description of the electromigration force and closing the gap between theory and experiment, an experiment needs to be designed at the scale of single atoms or single molecules in order to trace their individual motion. In this chapter we start with a brief discussion on graphene as a current-carrying substrate, followed by a description of experimental setups and sample preparation techniques. We report on one-dimensional migration of single Co adatoms along graphene nanoribbons, induced by voltage pulses applied on the nanoribbons with a tip of a scanning tunneling microscope (STM). We are able to trace the motion of Co by scanning the surface of the sample before and after voltage pulses. Later in section 2.8.2 we discuss the migration of Co on the underlying Au(111) surface and compare it to the statistics obtained for the motion of Co on nanoribbons. Finally, we present temperature-dependent diffusion measurements and draw conclusions on the effects of the current on the migration of Co adatoms.

## 2.2. GRAPHENE

Graphene – a single layer of graphite – is a two-dimensional carbon allotrope with carbon atoms arranged in a hexagonal lattice. It was first isolated in 2004 by Geim and Novoselov [42] for which they were rewarded a Nobel prize a few years later. Graphene efficiently conducts heat and electricity [43] and its strong in-plane  $\sigma$  bonds make it one of the strongest materials ever tested [44]. Graphene is also a good candidate for a current-carrying substrate for investigating current-induced forces. It can withstand very high currents while in vacuum without suffering damage and its 2D nature enables a confinement of the current within the atomically thin layer, in contrast to 3D materials where a large portion of the current flows into the bulk. The flat surface of graphene enables the observation of single adatoms deposited on top of it and tracking of their migration under the influence of the current.

### 2.2.1. GRAPHENE NANORIBBONS (GNRS)

Graphene nanoribbons (GNRs) are strips of graphene that can be fabricated with precise widths from chemical precursors. Their electronic and magnetic properties can be fine-tuned by choosing the appropriate width and edge geometry, enabling the fabrication of semiconducting or metallic GNRs. Figure 2.3 shows GNRs with zigzag (a) and armchair (b) edges. Zigzag GNRs are predicted to be half-metallic [45] and reveal spin-polarized edge states [46]. Armchair GNRs (AGNR) can be grouped into three families:  $N = 3p$ ,  $N = 3p+1$  and  $N = 3p+2$ , where  $p$  is an integer and  $N$  is the number of carbon atoms along the GNR width.  $N = 3p$  and  $N = 3p+1$  families have wide bandgaps that decrease with the increase of the ribbon width [47–50]. Models predict the family  $N = 3p+2$  to be metallic [47, 51]. Using GNRs is advantageous compared to using graphene for reasons that will become apparent in later sections.

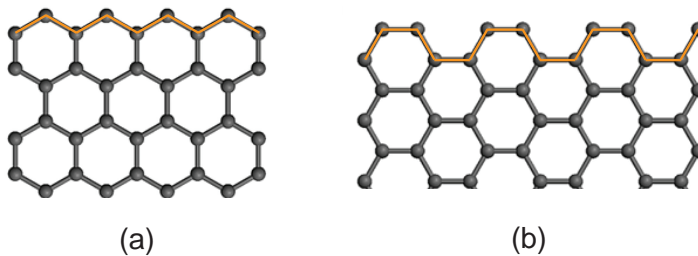


Figure 2.3: **Two different edges of a graphene nanoribbon.** (a) Zigzag and (b) armchair edge.

## 2.3. SCANNING TUNNELING MICROSCOPY

In classical mechanics current cannot flow in an open circuit when the potential barrier of the gap between two conductors is higher than the energy of the electrons. In quantum mechanics, however, electrons are presented with the wave function which decays exponentially within the insulating gap. If the gap is narrow enough, the wave function will reach the other electrode and there will be a nonzero probability for electrons to tunnel through the barrier.

In 1981 Binnig and Rohrer from the IBM Zurich Research Laboratory invented Scanning Tunneling Microscope (STM) based on the concept of quantum tunneling [52]. It was one of the first instruments ever to directly image the topography of a sample with atomic resolution. A probe (tip), usually made of a Au or Pt-Ir alloy wire, is brought into the vicinity of the sample<sup>2</sup> by means of a piezo actuator (Figure 2.4(a)). By applying a positive bias voltage to the sample with respect to the tip ( $V_b$ ),

<sup>2</sup> Typically at around 1-2 nm distance

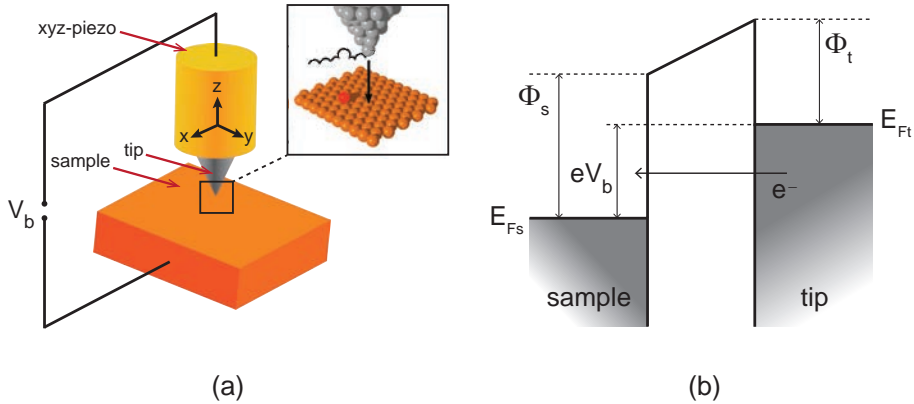


Figure 2.4: **Basic principle of STM.** (a) Schematics of a tip scanning over the surface of the sample with bias voltage  $V_b$  applied between them. A high voltage applied to the piezo actuator (yellow cylinder) serves as a feedback to keep the tunneling current constant. (b) Energy levels of a one-dimensional tunneling barrier. When a bias voltage is applied, tip states between the energy levels  $E_{F_t} - eV_b$  and  $E_{F_t}$  (Fermi energy of the tip) can tunnel to the sample, generating a tunneling current proportional to  $V_b$ .

electrons with the energy between  $E_{F_t} - eV_b$  and  $E_{F_t}$  (Fermi energy of the tip) can tunnel from occupied states in the tip to unoccupied states in the sample, generating a net tunneling current<sup>3</sup> (Figure 2.4(b)). The tunneling current exponentially decays with the distance  $z$  between the sample and the tip as

$$I \propto V_b e^{-kz} \quad (2.2)$$

where  $V_b$  is bias voltage and  $k$  is a decay constant of the tip state near the Fermi level in the barrier region. In the approximation  $eV_b \ll \phi$ ,  $k$  can be expressed as

$$k = \frac{\sqrt{2m_e\phi}}{\hbar} \quad (2.3)$$

where  $m_e$  is the mass of electron,  $\phi$  is the work function of the tip and sample, and  $\hbar$  is the reduced Planck constant. In general, the work function depends not only on the material but also on the crystallographic orientation of the surface<sup>4</sup>.

In constant-current mode, the tunneling current is amplified and converted to voltage by the current amplifier and then compared with the reference value (setpoint). The difference is then amplified to drive the Z-piezo and control the tip-sample distance in order to maintain the setpoint current. This is known as the feedback loop. As the tip scans over the surface of the sample line by line in a raster-like fashion, a Z displacement given by the high voltage applied to the piezo actuator is

<sup>3</sup> For negative bias voltage, tunneling current will flow in the opposite direction

<sup>4</sup> For typical values of the work function of a metal (around 5 eV), change of the tip-sample distance by 0.1 nm results in an order of magnitude change in tunneling current

recorded. The recorded array of equilibrium  $Z$  positions is then displayed as a height image of the sample surface. Bright spots represent high  $z$  values (protrusions), and dark spots represent low  $z$  values (depressions). The contrast in STM images does not depend only on the topography of the sample surface, but also on the electronic structure of the sample<sup>5</sup>. Measurements with STM in ultra-high vacuum environment at low temperatures can yield atomic resolution imaging and spectroscopy.

All experiments in this chapter were carried out with an STM technique using three different types of STM described in section 2.5.

## 2.4. ATOMIC FORCE MICROSCOPY AND KELVIN PROBE FORCE MICROSCOPY

Atomic Force Microscopy (AFM) is another surface imaging technique invented by G. Binnig *et al.* [53]. AFM does not require a conductive probe and sample, as it measures the force between them. The AFM used in experiments in this chapter is based on piezoelectric properties of the mechanical actuator (quartz tuning fork) which serves as the force sensor [54]. In non-contact AFM, the mechanical actuator is excited to oscillate at its resonance frequency  $f_0$ . As the tip on the tuning fork approaches the sample and feels an attractive or repulsive force, a feedback loop ensures that the tuning fork oscillates with a constant amplitude. The deflection signal is routed through a bandpass filter, phase shifted and fed back to the actuator. A phase-locked loop determines the oscillation frequency  $f = f_0 + \Delta f$ , and the frequency shift  $\Delta f$  is used as the signal.

We used AFM to determine a difference in work functions between the sample and the tip (Figure 2.5). When two bodies are in electrical contact, electrons flow from the metal with the higher Fermi energy (lower work function  $\Phi$ ), to the one with the lower Fermi energy (higher  $\Phi$ ), until Fermi levels are aligned (Figure 2.5(b)). The accumulated negative charge on one electrode will attract positive charges in the other, creating an electric field within the gap, hence an extra attractive force. By applying appropriate bias voltage between sample and tip, the electric field is canceled and the situation from panel (a) is restored (Figure 2.5(c)). The voltage required to minimize electrostatic interaction is given by

$$V_b^* = \frac{1}{e}(\Phi_s - \Phi_t) \quad (2.4)$$

The concept of detecting differences in work functions via the electric field between two electrodes was introduced by Lord Kelvin [55]. Kelvin probe force microscopy (KPFM) uses the force between the sample and the oscillating probe (tip) as a signal. This is done by keeping the tip at a fixed position while sweeping the

<sup>5</sup> For this reason one usually refers to feature sizes in STM images as *apparent* height and width

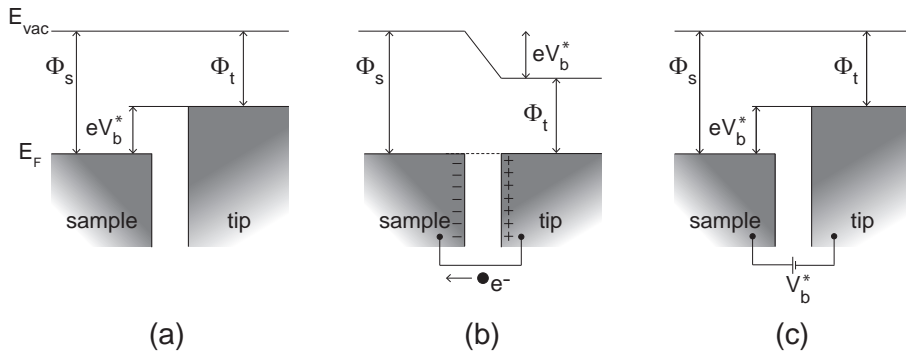


Figure 2.5: **Energy levels of two metallic surfaces facing each other.** (a) No electrical connection between sample and tip. Vacuum levels are aligned while the Fermi energies are not, due to the difference in work functions of the sample and the tip ( $\Phi_s$  and  $\Phi_t$ , respectively). (b) Sample and tip are electrically connected. Electrons flow to the electrode with higher work function until the Fermi energies align. This charge transfer causes an electric field between the sample and the tip. (c) By applying an appropriate bias voltage,  $V_b^*$ , the contact potential difference is compensated and the electrostatic interaction is minimized.

bias voltage and recording the frequency shift,  $\Delta f$ , caused by the electrostatic interaction between the sample and the tip. The  $\Delta f(V)$  spectrum is known as the Kelvin parabola. For a certain value of the bias voltage  $V_b^*$ , the electrostatic interaction between the sample and the tip will be minimized and the frequency shift will reach its extremum. The bias voltage of minimal interaction provides a qualitative measure of the difference in work functions between the sample and the tip.

## 2.5. EXPERIMENTAL SETUPS

### 2.5.1. JEOL ROOM-TEMPERATURE UHV STM

2

Initial experiments on CVD graphene were performed in a JEOL ultra-high vacuum Scanning Tunneling Microscope (UHV STM) operating at room temperature (Figure 2.6). The setup consists of three separate chambers: load-lock, preparation chamber and STM chamber. The sample and tip holders are introduced from the load-lock to the preparation chamber with a short transfer arm. The preparation chamber is equipped with a heater for sample preparation. The scan head is located in the STM chamber at a pressure of  $1 \cdot 10^{-9}$  mbar. Sample holder is mounted on a piezo tube with a  $2 \mu\text{m}$  range of motion along X and Y directions. The sample holder has two electrical contacts for the placement of current through graphene. The STM tip is a  $200 \mu\text{m}$  gold wire.

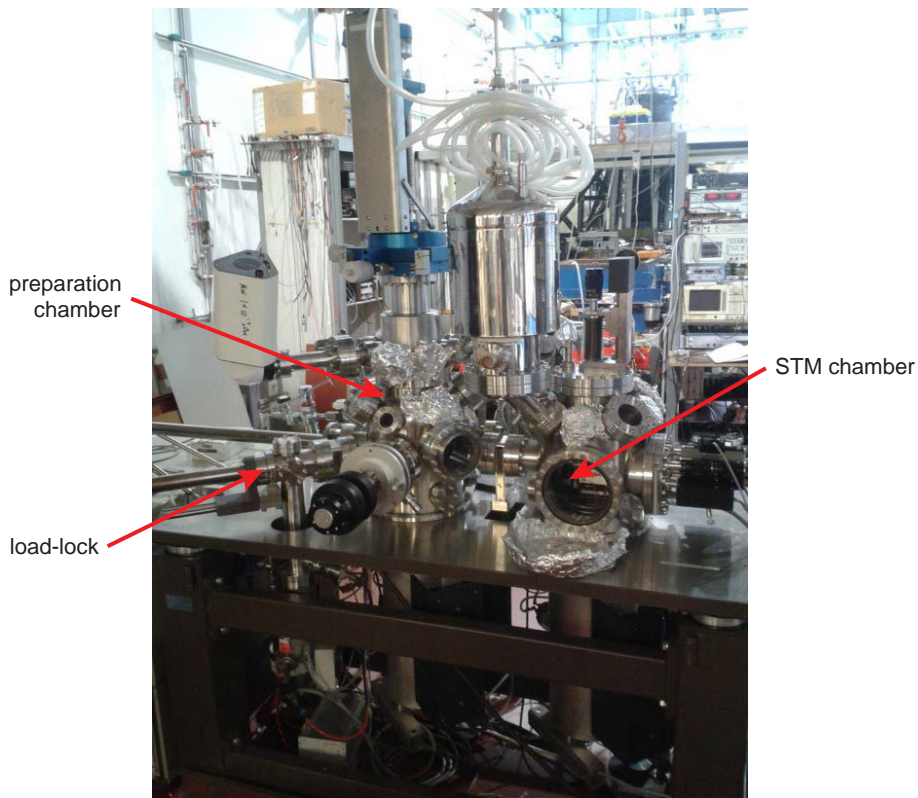


Figure 2.6: JEOL room temperature UHV STM/AFM. The setup consists of three independent chambers: load-lock, preparation chamber (with a heater) and STM chamber.

### 2.5.2. SPECS LOW-TEMPERATURE UHV STM

A part of experiments on CVD graphene were performed in a low-temperature SPECS Joule-Thomson UHV STM (Figure 2.7) in Delft, in the group of Sander Otte. The operating temperature is 10 K and the pressure is  $7 \cdot 10^{-11}$  mbar. The sample holder in this STM also has two contacts for placement of current through graphene. As a tip we used either a chemically etched tungsten wire or PtIr wire.

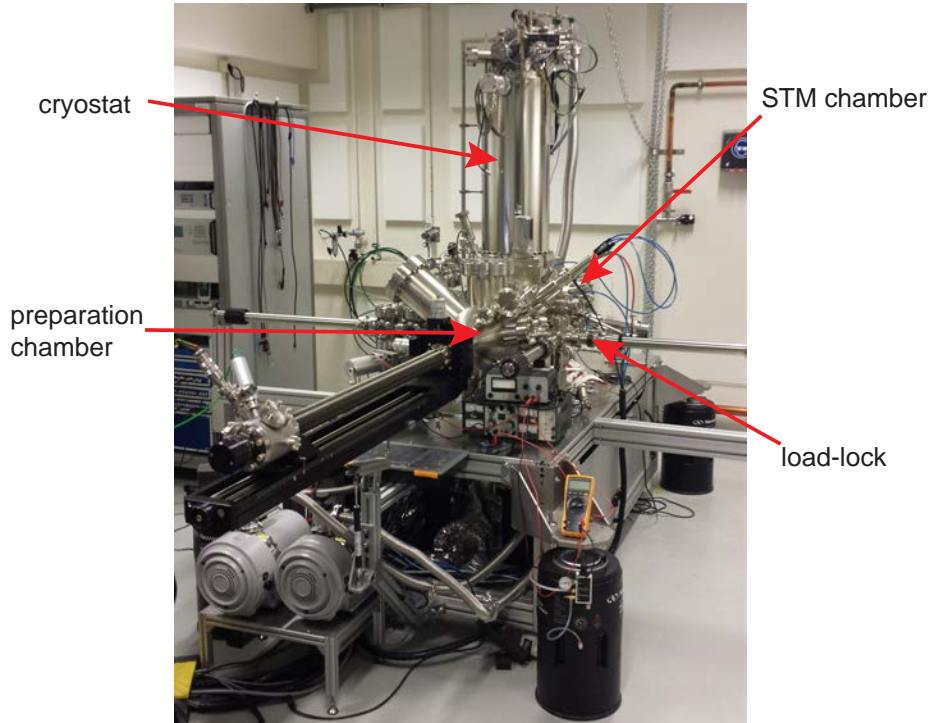


Figure 2.7: **SPECS Joule-Thomson low temperature UHV STM.** The setup consists of three independent chambers: load-lock, preparation chamber and STM chamber. The sample is inserted into the load-lock and transferred to the preparation chamber. An evaporator is situated in the preparation chamber and evaporation is done *in situ* directly onto the cooled sample.

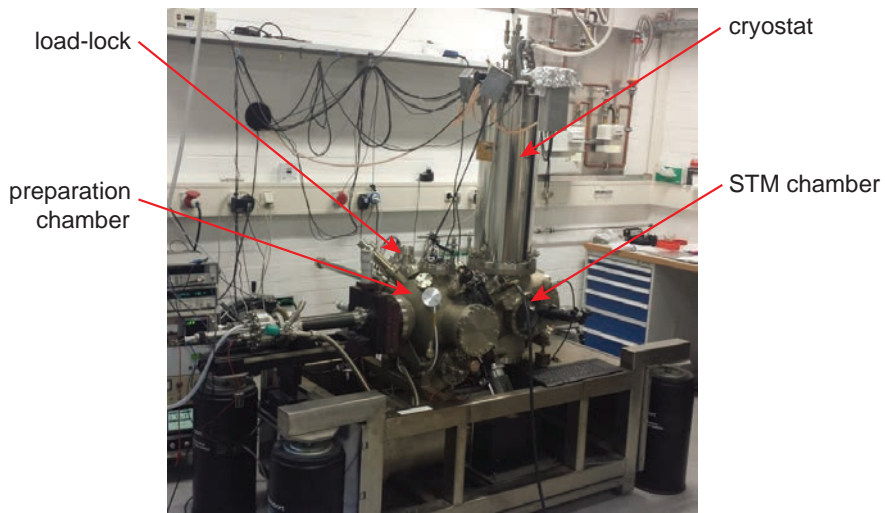
### 2.5.3. CREATEC LOW-TEMPERATURE UHV STM

The majority of the experiments in this chapter were carried out using a low-temperature UHV combined STM/AFM system, which is a modified version of a commercially available instrument from Createc Fischer & Co. GmbH® (Figure 2.8(a)) at the University of Regensburg in the group of Jascha Repp.

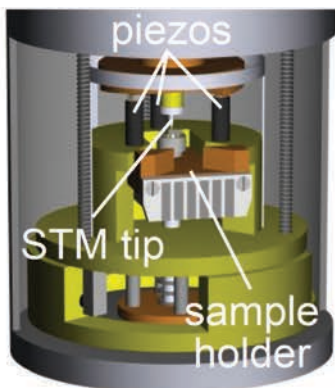
The setup consists of three separate chambers: load-lock, preparation chamber and STM chamber. The preparation chamber is equipped with a sputter gun for

sample preparation. A quartz sensor for molecular deposition and evaporators for atomic and molecular evaporation are introduced from the load-lock with a transfer arm. The scan head is located in the STM chamber under the liquid helium bath cryostat at 7-10 K at a pressure of  $P = 5 \cdot 10^{-11}$  mbar.

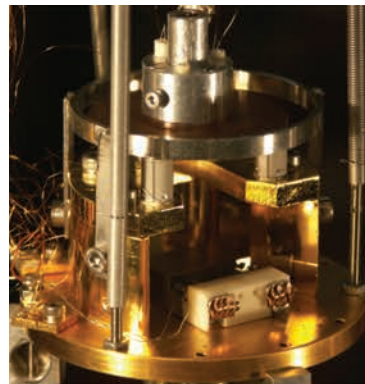
The STM scan-head is based on the Besocke beetle design [56, 57] shown in Figure



(a)



(b)



(c)

Figure 2.8: **Crearec low temperature UHV STM/AFM.** (a) The setup consists of three independent chambers: load-lock, preparation chamber and STM chamber. The sample and evaporators are inserted into the load-lock and transferred to the preparation chamber. (b) Schematics of the STM/AFM scan head based on the Besocke beetle design. (c) Photograph of (b) without the sample holder inside.

2.8(b), (c). The STM tip is attached to a disk which rests on three sapphire balls glued to three piezo tubes. By applying a saw-tooth voltage pulses to the electrodes of the piezo tubes, the disk is rotated using the principle of a slip-stick motion. Since the disk has three slightly inclined planes on the bottom side, motion of the piezos results in a vertical motion of the tip. The scan-head is suspended by three springs and equipped with an eddy current damping system.

## 2.6. FIRST EXPERIMENT: CVD GROWN GRAPHENE ON Si/SiO<sub>2</sub> IN ROOM-TEMPERATURE JEOL STM

Initial experiments were performed in the JEOL room-temperature UHV STM using CVD grown graphene on a Si/SiO<sub>2</sub> substrate purchased from Graphenea®. The SiO<sub>2</sub> thickness of 285 nm serves to separate graphene electrically from Si in order to ensure confinement of the current within the graphene sheet and the thickness is such that single-layer graphene deposited on top of it can be detected optically.

Graphene was covered with a layer of poly(methyl methacrylate) polymer (PMMA) and patterned with electron-beam lithography in order to obtain a 300×300 μm<sup>2</sup> graphene patch. In a second lithography step, electrodes were patterned and graphene was further contacted with a 5 nm thick adhesion layer of chromium and a 100 nm thick layer of gold deposited by thermal evaporation (Figure 2.9(a)). The sample was subsequently placed inside a JEOL room-temperature ultra-high vacuum scanning tunneling microscope (UHV STM) in order to image the surface of the graphene. However imaging of the sample was obstructed due to the presence of unavoidable PMMA residues on the surface of the graphene, even after thorough cleaning with acetone. The STM tip was continuously crashing while scanning over the parts covered with insulating polymer. *In situ* thermal annealing of the sample at 280°C for 6 hours reduced the noise level in the current signal, however the sample remained contaminated by the organic residue and the graphene lattice was not observed.

As a solution for cleaning the sample, we employed the current-induced cleaning procedure of graphene by Moser *et al.* [58], where they introduce a current density of 10<sup>8</sup> A/cm<sup>2</sup> into exfoliated graphene in ambient conditions, in order to remove contaminants deposited during lithography. The effects of a large electrical current passing through a graphene sheet include Joule heating, evaporation of nanoparticles due to high temperatures and possibly electromigration of material. Injection of the current of 3 mA (which translates to a current density of around 3·10<sup>6</sup> A/cm<sup>2</sup>) into the graphene via two gold contacts for the duration of 1 hour resulted in the removal of a large fraction of PMMA residue from the surface, and atomic resolution was achieved (Figure 2.9(b)). It should be noted that the sample was not perfectly clean even after all the above-mentioned cleaning procedures, which was noticeable in the STM images.

After confirming that surface of graphene can be cleaned using the current-cleaning

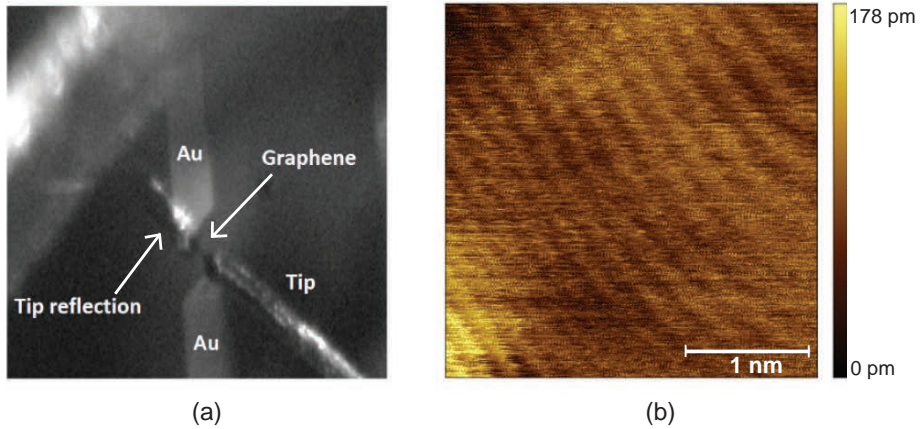


Figure 2.9: **Graphene patterned with e-beam lithography** ( $300 \times 300 \mu\text{m}^2$ ). (a) Optical microscope image of the sample and the tip positioned inside the JEOL UHV STM at room temperature. (b) Atomic resolution of graphene after current-cleaning procedure.

technique, we proceeded with experiments in the low-temperature STM. Single adatoms are mobile at the room temperature and the sample has to be cooled down in order to avoid any thermal motion before inducing electromigration.

## 2.7. SECOND EXPERIMENT: CVD GROWN GRAPHENE ON $\text{Si}/\text{SiO}_2$ IN LOW-TEMPERATURE SPECS STM

After confirming that the current-cleaning procedure was successful in removing the majority of polymer residue off the surface of the graphene, we have made an attempt to induce electromigration inside a SPECS® low-temperature UHV STM. The position of the camera on the STM chamber which gave visual access to the position of tip with respect to sample was a limiting factor in the size of the graphene, as it would be hard to approach the tip to the sample on a small graphene patch without the tip crashing onto the insulating  $\text{SiO}_2$ . We used  $5 \times 5 \text{ mm}^2$  CVD graphene on copper purchased from Graphenea®, which we transferred to a  $\text{Si}/\text{SiO}_2$  substrate (with 285 nm oxide thickness). The graphene patch was contacted with chromium and gold as described earlier, giving a resistance of 15 k $\Omega$ . After passing a current of  $I = 5.2 \text{ mA}$  in the graphene for 20 min as a cleaning procedure, the sample was cooled down to 10 K and subsequently scanned (Figure 2.10(a)). First, in this high-resolution image (note the scale) we recognize the hexagonal graphene lattice structure throughout the image, demonstrating that the surface is mostly clean. Second, the surface does not appear flat, there is a modulation of the height with a cloudy-like

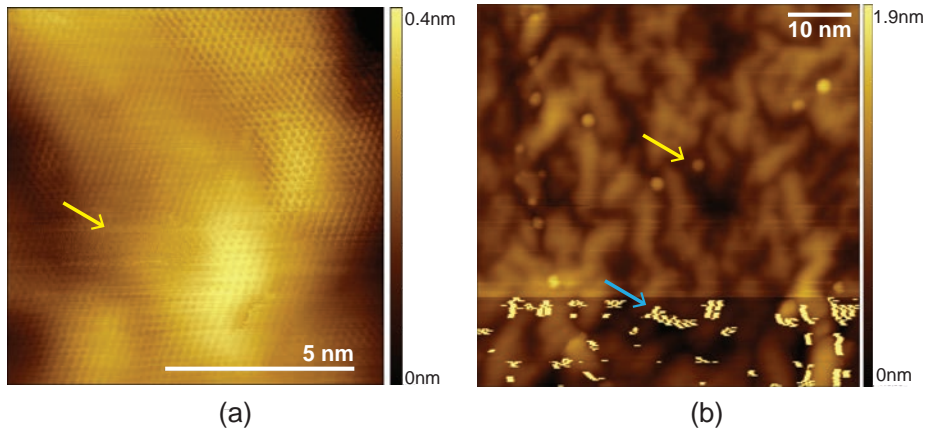


Figure 2.10: **STM images of graphene before and after evaporation of Co adatoms.** (a) Graphene on SiO<sub>2</sub> after current cleaning at high resolution (note the scale bar of 5 nm). Graphene appears to be relatively clean in the upper half of the image until the onset of horizontal stripes (indicated by yellow arrow). Scanning parameters:  $V = 1$  V,  $I = 100$  pA. (b) Graphene surface imaged over a wider area (scale bar 10 nm) after *in situ* evaporation of cobalt. Co adatoms appear as bright round shapes (the yellow arrow points at one of the Co adatoms or clusters). Small bright patches that appear in the bottom of the image (indicated by the blue arrow) are most likely dirt that comes from polymer residues and that the tip picked up. The images were obtained at 10 K. Scanning parameters:  $V = 2$  V,  $I = 30$  pA.

structure. This cloudy structure is usually attributed to the SiO<sub>2</sub> surface roughness [59], possibly in combination with random structure of charge traps in the Si/SiO<sub>2</sub> substrate. Graphene appears to be relatively clean in the upper half of the image until the point indicated by the yellow arrow, after which horizontal stripes can be observed. Their appearance suggests that the sample is not quite clean, and that the tip picks up dirt and changes as it scans along the horizontal line.

Cobalt atoms were evaporated *in situ* on cold graphene via e-beam heating. Figure 2.10(b) shows graphene after Co evaporation. Co adatoms or clusters appear as bright round shapes (the yellow arrow indicates one of the adatoms or clusters). Small bright irregular patches in the bottom of the image (indicated by the blue arrow) are attributed to dirt that the tip picked up during the scan, and they are present in the majority of the scans. In this particular experiment we did not have means to clean the tip, since the usual tip indentation into a clean patch of a Au metal surface was not an option. A current of  $I_{\max} = 9$  mA (which corresponds to around  $5 \cdot 10^5$  A/cm<sup>2</sup> current density) was applied through graphene for  $t = 17$  min. This was the maximum current that the STM wires were designed to carry. We observed no motion of Co adatoms, which indicates that the current density was not sufficient to induce electromigration. A possible reason for the lack of motion of adatoms could be that Co adheres more strongly to graphene/SiO<sub>2</sub> than the polymer does.

Considering the practical limitations of using CVD graphene, such as limitations

in achievable current density, limitations imposed by the corrugation of the SiO<sub>2</sub> substrate and limitations in cleaning of adsorbents and other defects, we concluded that graphene is not the most suitable material for our experiment. We decided to proceed with an alternative substrate: graphene nanoribbons.

## 2.8. THIRD EXPERIMENT: GRAPHENE NANORIBBONS IN LOW-TEMPERATURE CREATEC STM

In contrast to CVD graphene, the surface of graphene nanoribbons (GNRs) is free of contaminants since there is no polymer involved in the preparation procedure and the growth of GNRs takes place under UHV conditions. The growth substrate has to be a metal (usually Au, Ag or Cu), since it serves as a template and catalyst for the surface-assisted synthesis step.

A single crystal of Au(111) was cleaned by Ne<sup>+</sup> ion sputtering at the pressure of 10<sup>-5</sup> mbar, followed by thermal annealing at 550°C. The procedure for growth of GNRs on Au(111) is reproduced from the work of Cai *et al.* [61]. We used 10,10' - dibromo-9,9' -bianthryl (DBBA) molecules (Figure 2.11(a)) as precursors to produce armchair-edge graphene nanoribbons. DBBA was evaporated for 3-7 sec at a distance of around 1.5 cm from the sample. Thermal sublimation of DBBA onto the Au(111) surface kept at 100°C resulted in dehalogenation (removal of bromine atoms from DBBA molecules). In the first thermal activation step, the temperature was increased to 220°C and kept constant for 2 min, during which monomers diffused across the surface to covalently bond with other monomers by fusion of the bonds, exposed by the release of Br. This resulted in a formation of non-planar polymer chains (Figure 2.11(b)). In the second thermal activation step, the temperature was further increased to 410°C and kept constant for 3 min, inducing an intramolecular cyclodehydrogenation of the polymer chains and formation of armchair GNRs (Figure 2.11(c)).

As a tip we used a 20 μm thick PtIr wire. The tip was prepared by controlled crashes onto the clean gold surface with the feedback on and 10<sup>6</sup> amplifier gain, which resulted in atomically sharp gold-coated STM tip. Figure 2.12 shows a Kelvin parabola  $\Delta f(V)$  (discussed in subsection 2.4). The value of the bias voltage that corresponds to the minimum of  $\Delta f$  is around 500 mV. The bias voltage is applied on the sample while the tip is virtually grounded, therefore the work function of the sample is 500 meV higher than the work function of the tip.

In addition to KPFM, we used AFM to detect when the tip would become blunt and perform a new cycle of tip preparation. Determining the shape of the tip was done by comparing the oscillation frequency of the tip when it is positioned far away from the sample (out of tunneling) to the frequency of the tip in the vicinity of the sample. For a wide (blunt) tip the frequency shift is large due to a large interaction of the tip with the sample (~ 25 Hz). For a good, sharp AFM tip the frequency shift is

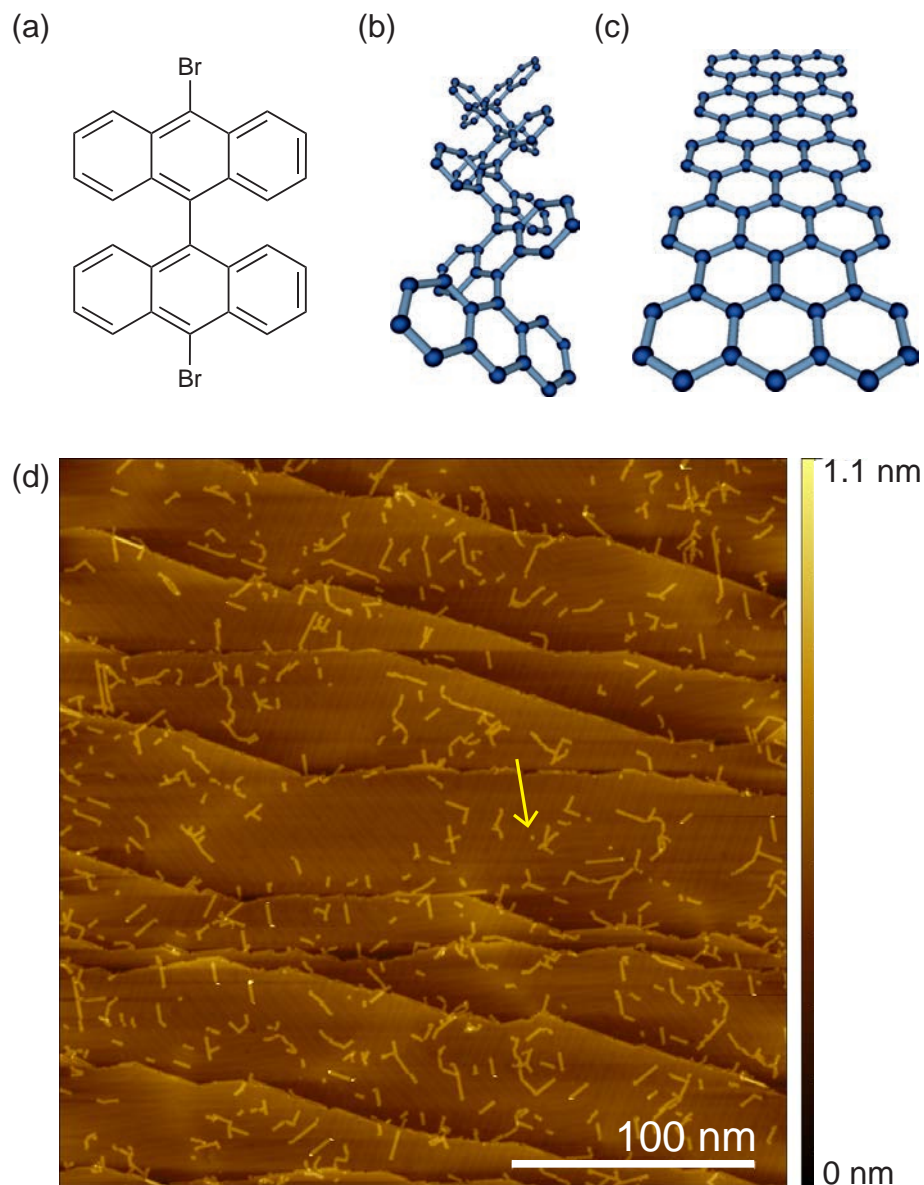


Figure 2.11: **Bottom-up fabrication of 7-armchair GNRs.** (a) Chemical structure of a 10,10'-dibromo-9,9'-bianthryl (DBBA) precursor molecule [60]. (b) C-C covalent bonding and formation of a linear polymer during the first annealing step. (c) Formation of a 7-AGNR as a result of cyclodehydrogenation during the second annealing step. (d) STM image of the sample after GNR formation on Au(111) ( $V_b = 100$  mV,  $I = 1.1$  pA). The bright worm-like structures scattered over the surface are the GNRs. Small square-like bright features are single precursor molecules (indicated by the yellow arrow).

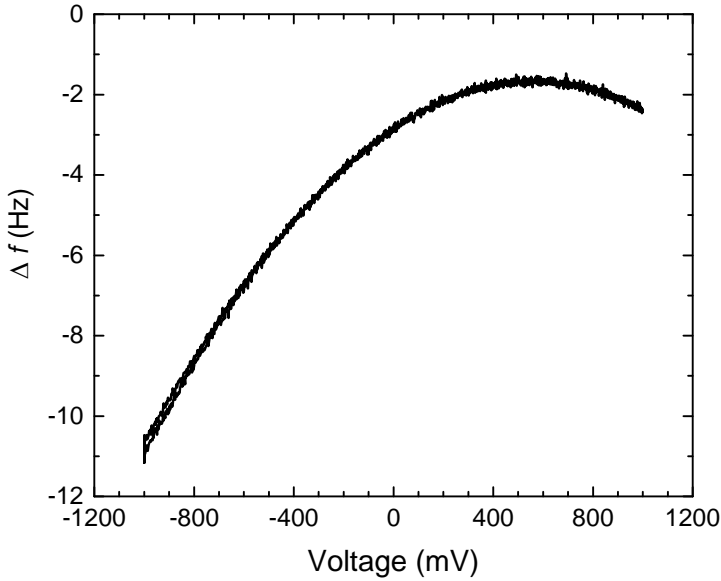


Figure 2.12: **Kelvin probe force microscopy (KPFM) measurement.** The maximum of the curve (i.e. the minimum of  $\Delta f(V)$ ) corresponds to approximately 500 mV bias voltage.

around 5 Hz.

An STM image of the sample after the formation of GNRs is shown in Figure 2.11(d). Small square-like bright features are single precursor molecules (indicated by the yellow arrow), while the elongated rectangular or worm-like structures are the GNRs. The lengths of the GNRs range from 2 to 40 nm.

As the next step we performed *in situ* evaporation of cobalt (Co) on the sample via electron beam evaporation. Co was evaporated at a distance of around 15 cm for 5 sec, while the high voltage was at 2 kV and the emission current read out was 2 mA. An STM image of the sample after Co deposition is shown in Figure 2.13(a). Co adatoms on Au(111) appear as small bright round shapes with the apparent height of 0.2 nm and a diameter of  $\sim 0.5$  nm. As a first important observation we notice that a significant fraction of Co atoms reside on top of GNRs. Co adatoms on a GNR appear much bigger, with the apparent diameter of 1.5 - 2 nm [62] (see the linear height profile in the inset in Figure 2.13(b)).

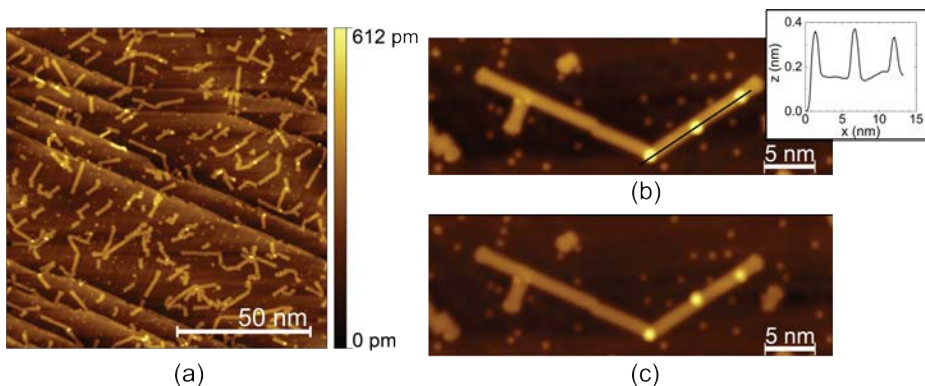


Figure 2.13: **Sample after Co evaporation.** (a) Large-area STM image of the sample after cobalt evaporation ( $V_b = 0.1$  V,  $I = 2$  pA). (b) STM image of a GNR with three Co adatoms on top ( $V_b = 0.3$  V,  $I = 1.6$  pA). Co adatoms on a GNR appear bigger than Co adatoms on a gold surface. The inset shows a line profile along one arm of a GNR indicated by the black line in the main panel. (c) STM image of the same GNR after tip manipulation. The middle Co adatom moved laterally from the right to the left on the GNR.

Co adatoms can be found in different lateral positions on the GNR (Figure 2.13(b), (c)). DFT calculations for Co adatoms on a graphene sheet indicate that the stable adsorption site for Co is the center of the GNR hexagon [63], which suggests five possible lateral positions (blue dots in Figure 2.14). We cannot distinguish all five positions within the STM resolution ( $\sim 0.2$  nm).

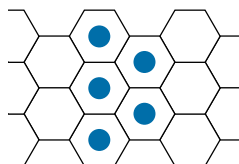


Figure 2.14: **Possible lateral adsorption sites for Co adatom on GNR (blue dots)** [63].

### 2.8.1. CURRENT-INDUCED MANIPULATION OF CO ADATOMS

The GNRs of interest are 5–20 nm long, do not cross other GNRs and have 1–7 Co adatoms on top. These criteria were chosen in order to ensure the best possible conditions for tracking of Co adatoms after injection of the current. Migration of Co adatoms on a GNR was induced by applying voltage pulses while the tip was brought into point contact with the GNR. We used voltage pulses in the range of  $-1000$  mV  $\leq V_b \leq -600$  mV and  $600$  mV  $\leq V_b \leq 1200$  mV (voltage is applied on the sample while

the STM tip is grounded).

Increase of the current with decreasing tip–sample distance ( $z$ ) in most cases had a smooth exponential trend up to  $10\ \mu\text{A}$  (the value at which the current amplifier saturates) without noticeable kinks in the slope that would indicate point contact between the tip and the GNR. In order to obtain the point-contact value, we first established a tip–Au(111) point contact on the Au surface near a GNR (which corresponds to  $R = 12.9\ \text{k}\Omega$ ), then we lifted the tip by the height of the GNR ( $\sim 0.2\ \text{nm}$ ) and positioned it above the GNR. The current read-out for this tip position showed values around  $0.3\text{--}0.6\ \mu\text{A}$  for  $100\ \text{mV}$  bias voltage (which corresponds to  $R_{\text{pc}} \approx 250\ \text{k}\Omega$ ). This value was noted as the tip–GNR point contact and was used in all manipulation experiments. The point contact was also confirmed by observing a small kink in the current slope around  $0.3\text{--}0.6\ \mu\text{A}$  in some of the  $I(t)$  curves.

During the manipulation, the initial setpoint is set to  $I = 1\text{--}2\ \text{pA}$  at  $V_{\text{b}} = 0.1\ \text{V}$ . After switching off the feedback, the amplifier gain is reduced to  $10^6$  to enable recording of higher currents. The STM tip is brought closer to the GNR until the point contact value is reached. A voltage pulse is subsequently applied with a duration of  $0.2\text{--}1\ \text{sec}$ . The tip is then retracted, the amplifier gain is set back to  $10^{11}$  and the feedback is switched on. Figure 2.15(a) shows an example of this procedure for a positive voltage

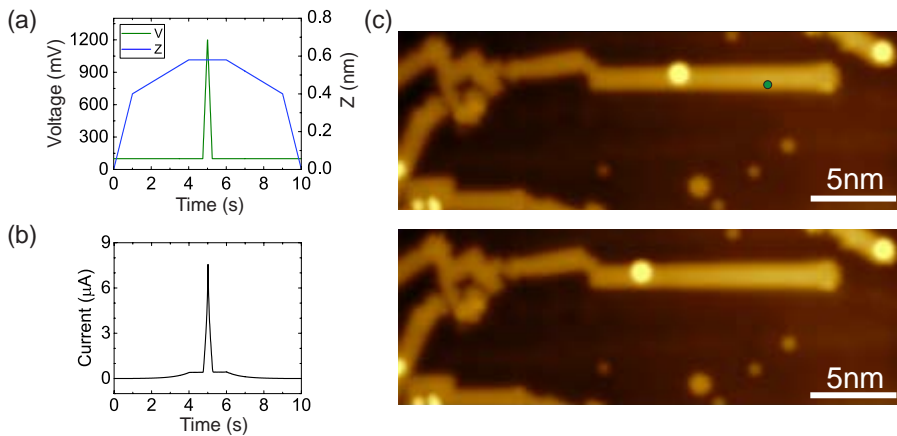


**Figure 2.15: Example of the motion of a single cobalt adatom along a GNR induced by a positive voltage pulse via the STM tip.** (a) The blue line represents the relative tip–sample distance ( $Z$ ) with respect to the feedback setpoint position.  $Z$  increases as the tip goes towards the surface, until the point-contact position with a GNR is reached. Around 1 sec after the point-contact is established, a short voltage pulse of  $V_{\text{b}} = 1200\ \text{mV}$  is applied (green line) and the tip is subsequently retracted by a procedure that is the reverse of the approach. (b) Current corresponding to the tip motion and voltage pulse from (a). At the initial bias of  $100\ \text{mV}$ , the value of the point-contact current between the tip and the GNR is around  $0.3\text{--}0.6\ \mu\text{A}$ . (c) STM images of a GNR before and after the voltage pulse of  $V_{\text{b}} = 1200\ \text{mV}$ . The green dot on the GNR marks the position of the tip at the moment of the pulse after which the Co adatom has moved away from the tip, as observed in the lower image taken after the event.

pulse of  $V_b = 1200$  mV (green line) and the corresponding Z-position of the tip with respect to the feedback setpoint position (blue line). Figure 2.15(b) shows the corresponding current. After the voltage pulse, the same sample area is scanned in order to trace any motion of Co adatoms.

STM images of the sample before and after a positive voltage pulse of  $V_b = 1200$  mV on the GNR can be seen in Figure 2.15(c). The green dot marks the position of the tip at the moment of the pulse. After the voltage pulse, we observe that the Co adatom has moved along the GNR away from the tip.

An example of a negative voltage pulse of  $V_b = -900$  mV and the corresponding current can be seen in Figure 2.16(a), (b), respectively. Figure 2.16(c) shows STM images of Co on a GNR before and after this negative voltage pulse of  $-900$  mV (with the tip at the position marked by the red dot). In this particular case, the Co adatom is observed to have moved towards the tip after the pulse. Interestingly, we find that the atoms are displaced along the GNR and do not leave the GNR towards the Au(111) surface. We will discuss this confinement of Co adatoms to GNRs more extensively in the following sections.

Two GNRs can chemically bond to form a GNR with a bend. If the produced 7-AGNRs come into close proximity to each other, they can undergo cross-dehydrogenative coupling to form more complex structures [64, 65]. The work of Dienel *et al.* [66] offers a comprehensive characterization of the atomic connectivity in the 7-AGNR junctions on Au(111). Figure 2.17(a) shows an STM image (courtesy [66])

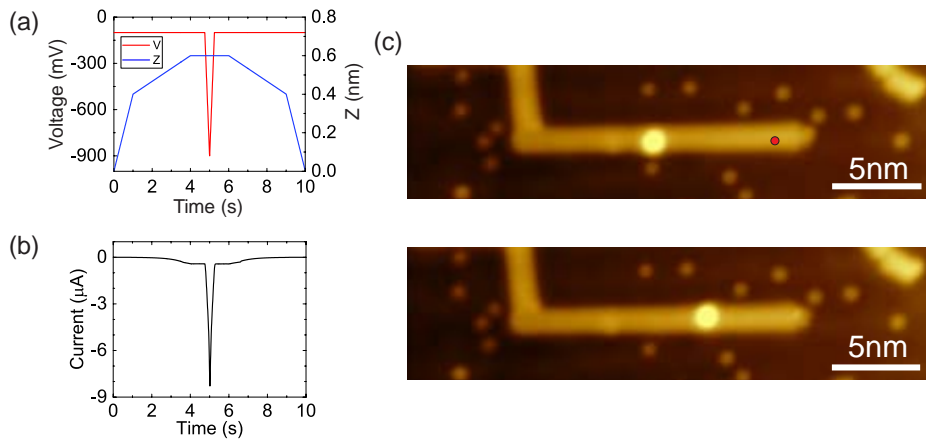


**Figure 2.16: Example of an induced motion of a single cobalt adatom on a GNR by a negative voltage pulse via the STM tip.** (a) The red line represents a negative voltage pulse of  $V_b = -900$  mV with a duration of 0.5 sec. The blue line represents the relative tip-sample distance ( $Z$ ) with respect to the feedback setpoint. (b) The current as a function of time. (c) Representative STM images of a GNR before and after a voltage pulse of  $V_b = -900$  mV. The red dot on the GNR marks the position of the tip at the moment of the pulse. The Co adatom is observed to have moved towards the tip after the pulse.

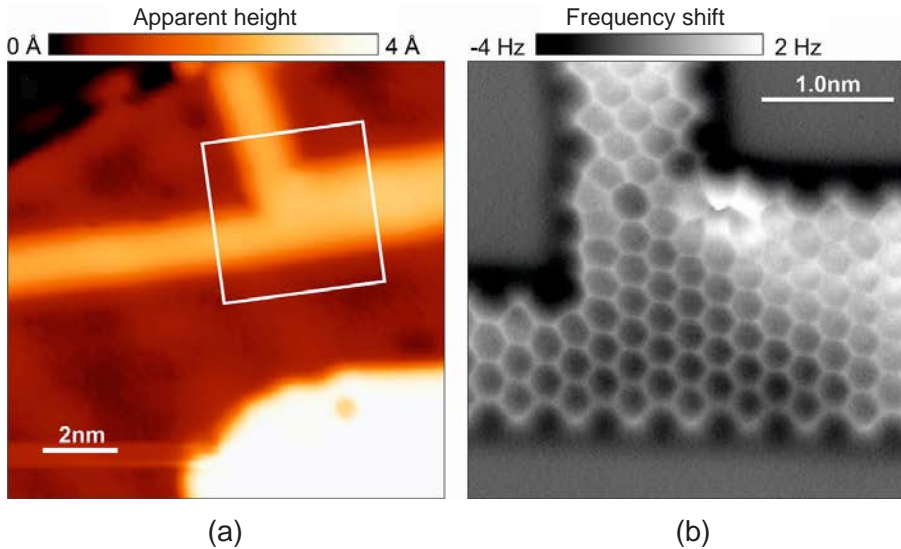


Figure 2.17: **Cross-dehydrogenative coupling of AGNRs.** (a) STM image ( $V_b = 0.2$  V,  $I = 2$  pA) of a junction between AGNRs of different widths on Au(111) (image taken with permission from [66]). (b) Constant-height non-contact AFM frequency shift image of the junction between two 7-AGNRs and one 14-AGNR shown in (b).

of a junction between two regular 7-AGNRs and a broader ribbon extending to the right. Figure 2.17(b) shows a non-contact AFM image in which one can distinguish the hexagonal rings within the two 7-AGNRs on the left and top edges of the image, and within the broad structure on the right. The broad structure is in fact a fully conjugated 14-AGNR formed by cross-dehydrogenative coupling of two 7-AGNRs along their long axis.

We find that Co adatoms can be manipulated even when the voltage pulse is applied around the bend of a GNR with such a kink. Figure 2.18 shows an example of a Co adatom manipulation on such a GNR. After a positive voltage pulse of  $V_b = 900$  mV (at the position marked by the green dot in panel (a)) on the right part of the GNR, the Co adatom is pushed away from the tip along the path of the GNR (panel (b)). Furthermore, after applying a second, negative voltage pulse of  $V_b = -1000$  mV (at the position marked by the red dot in panel (c)) the Co adatom moves along the GNR towards the tip (panel (d)). We have, however, not observed any motion of Co adatoms around the bend/corner of a GNR: once in the corner, Co adatom would not move along the GNR any longer after subsequent voltage pulses, suggesting that this position offers a local potential minimum for the Co adatom.

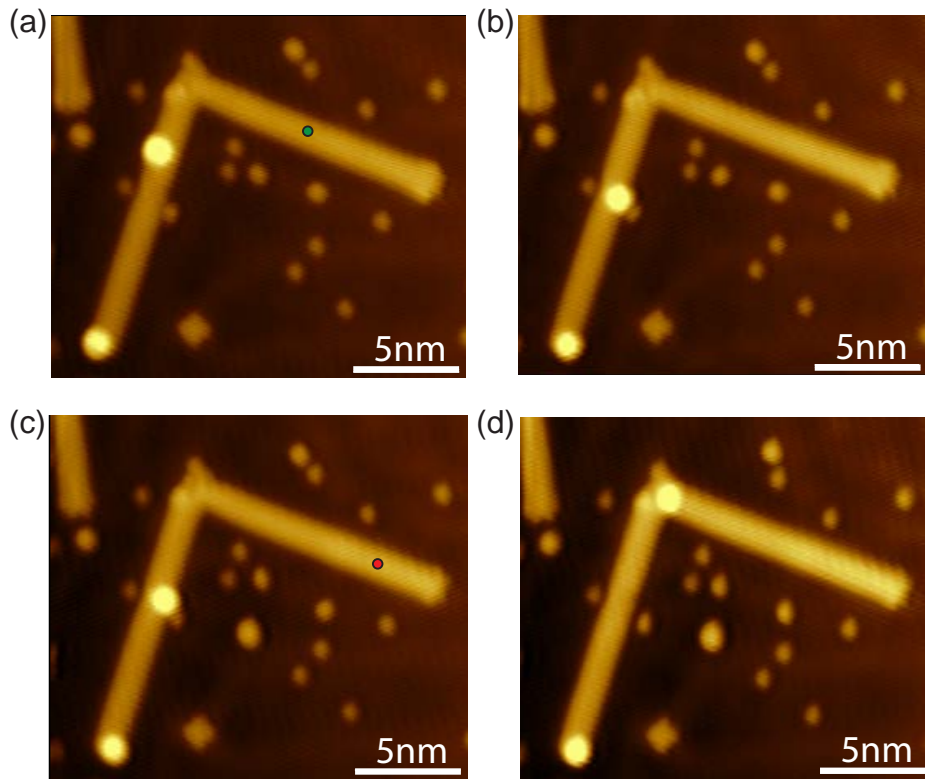


Figure 2.18: **Motion of a Co adatom on a GNR after voltage pulse around the corner of the GNR.** (a), (b) STM images before and after a positive voltage pulse of  $V_b = 900$  mV at the green dot in (a), respectively. (c), (d) STM images before and after a negative voltage pulse of  $V_b = -1000$  mV at red dot, respectively.

### 2.8.2. RESULTS

In total we performed around 900 voltage pulses on GNRs with the amplitude up to 1200 mV and  $-1000$  mV for positive and negative bias voltages, respectively. Parameters recorded with each voltage pulse are the value of the bias voltage ( $V_b$ ), the tunneling current ( $I$ ), the initial tip-adatom distance ( $X$ , ranging from 2.5 nm to 21 nm) and the resulting displacement of the Co adatoms ( $L$ ).  $X$  was measured from the tip position at the moment of the pulse to the center of the Co adatom at its initial position, while  $L$  was measured from the center of the Co adatom in its initial position to the adatom's center at its final position. If the Co adatom was not displaced,  $L$  was noted as 0 nm. Criteria for recording successful migration of adatoms were as follows:

- $|V_b| \geq |\pm 600|$  mV (voltage amplitudes lower than this value did not result in a significant fraction of moved Co adatoms)
- $|I| \geq |\pm 0.3|$   $\mu$ A (this value was recorded as the tip–GNR point contact current for  $\pm 100$  mV bias voltage)
- Co adatoms at the end points of GNR were not added to statistics as their motion was limited only to the direction towards the tip
- Co adatoms at the corner of kinked GNR were not added to statistics (we have not observed any displacement of these adatoms)
- Only observations for single Co adatoms were registered (clusters of two or more adatoms were dismissed)

Table 2.1 shows all events that occurred after voltage pulses. An event is considered as a motion of one Co adatom on the GNR on which the voltage pulse was performed, thus for one voltage pulse multiple adatoms might move, resulting in more than one event per pulse. Around half of the adatoms were displaced from their initial position

Cobalt on GNR	
Total number of events	1504
Number of Co that did not move	764 (50.8%)
Number of displaced Co (includes events below)	740 (49.2%)
- Co moved along GNR	543 (36.1%)
- Co moved left/right on GNR	55 (3.7%)
- missing Co	136 (9%)
- Co fell on Au(111)	6 (0.4%)

Table 2.1: **Statistics for migration of Co adatoms on GNRs after voltage pulses.** Total number of voltage pulses is around 900.

after the pulse. Displaced adatoms include the ones that moved along GNR, the ones that moved laterally ("left/right"), the ones that fell on gold substrate and the ones that were removed from GNR and were not traced back (so-called *missing* adatoms). Subsequent scans of the area around GNR in order to locate the missing Co adatoms showed that only in a few cases Co dropped on the gold surface (always in the vicinity of the initial Co position on the GNR).

### ESCAPE PROBABILITY

In Figure 2.19(a) we show the escape probability of Co adatoms on GNR after a voltage pulse, as a function of the initial tip-adatom distance ( $X$ ). By the escape probability we mean the probability for the Co atom to escape from the local potential well in which it is initially residing. Experimentally this is defined as the ratio of the number of displaced adatoms on a GNR and the total number of adatoms on the GNR at initial distance  $X$ :

$$\Gamma = \frac{N_{\text{displaced}}}{N_{\text{total}}}, \quad \Delta\Gamma = \sqrt{\frac{\Gamma(1-\Gamma)}{N_{\text{total}}}}. \quad (2.5)$$

The second expression in 2.5 gives a measure of the statistical accuracy of the escape probability. Each data point in Figure 2.19 corresponds to a 2 nm wide range of  $X$  values. For example, the value of  $X = 3$  nm corresponds to  $2 \text{ nm} \leq X < 4 \text{ nm}$  range of values; the value of  $X = 5$  nm corresponds to the range of values  $4 \text{ nm} \leq X < 6 \text{ nm}$ , and so forth. The number  $N_{\text{displaced}}$  includes all events for which the atoms have left its initial position, including those where the atoms have disappeared from the GNR. With the exception of the first few data points which appear to have nearly the same

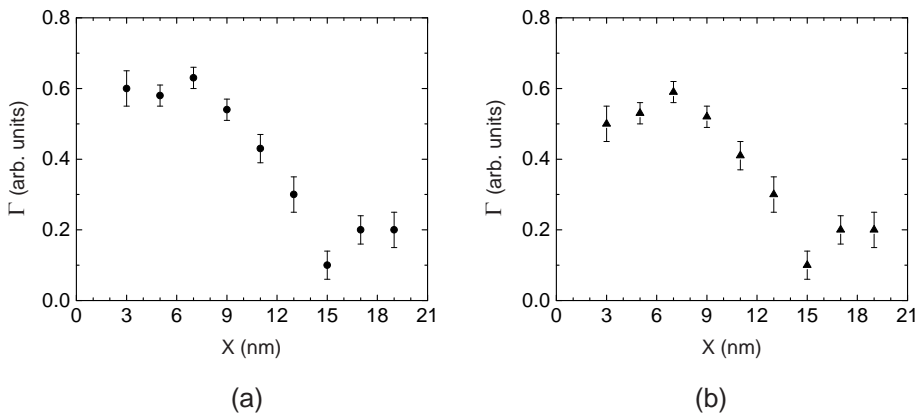


Figure 2.19: **Escape probability  $\Gamma$  as a function of initial tip-adatom distance.** (a)  $\Gamma(X)$  for all events. (b)  $\Gamma(X)$  for events excluding missing Co adatoms. Each  $X$  represents a 2 nm wide range of data points.

value, we observe a drop of the escape probability over the length scale of  $\sim 12$  nm.

Figure 2.19(b) shows the escape probability for Co adatoms, excluding the missing Co adatoms. We observe a similar trend, with the escape probability for each  $X$  slightly lower than the one in panel (a).

The first four data points ( $X \leq 10$  nm) in both graphs in Figure 2.19(a) have similar values for the escape probability, and we observe a drop with increasing  $X$  beyond 10 nm and a leveling off beyond 15 nm. If we take the escape probability to be constant for  $X \leq 10$  nm, then we can group the data together for this range of  $X$  and we can plot the escape probability ( $\beta$ ) as a function of the height of the voltage pulse for both subsets of the data, where  $\beta$  is defined analogous to  $\Gamma$  in Eq. 2.5. The difference in symbols emphasizes the fact that the two quantities refer to different selection criteria from the data sets. In  $\Gamma$  we have grouped up all voltage pulse heights together, in  $\beta$  we have lumped all  $X \leq 10$  nm together. Figure 2.20(a), (b) shows  $\beta(V)$  for all events and for events excluding missing adatoms, respectively. The data is fitted to an exponential function  $\beta = e^{-\frac{c}{\sqrt{V}}}$  where  $c$  is a fitting parameter [67]. The red and green curves are fits to negative and positive voltage data points, respectively, showing that the two data sets are fairly symmetric in voltage. We also obtained partial data for lower voltages (e.g.  $\pm 500$  mV), however we do not have enough statistics to present it.

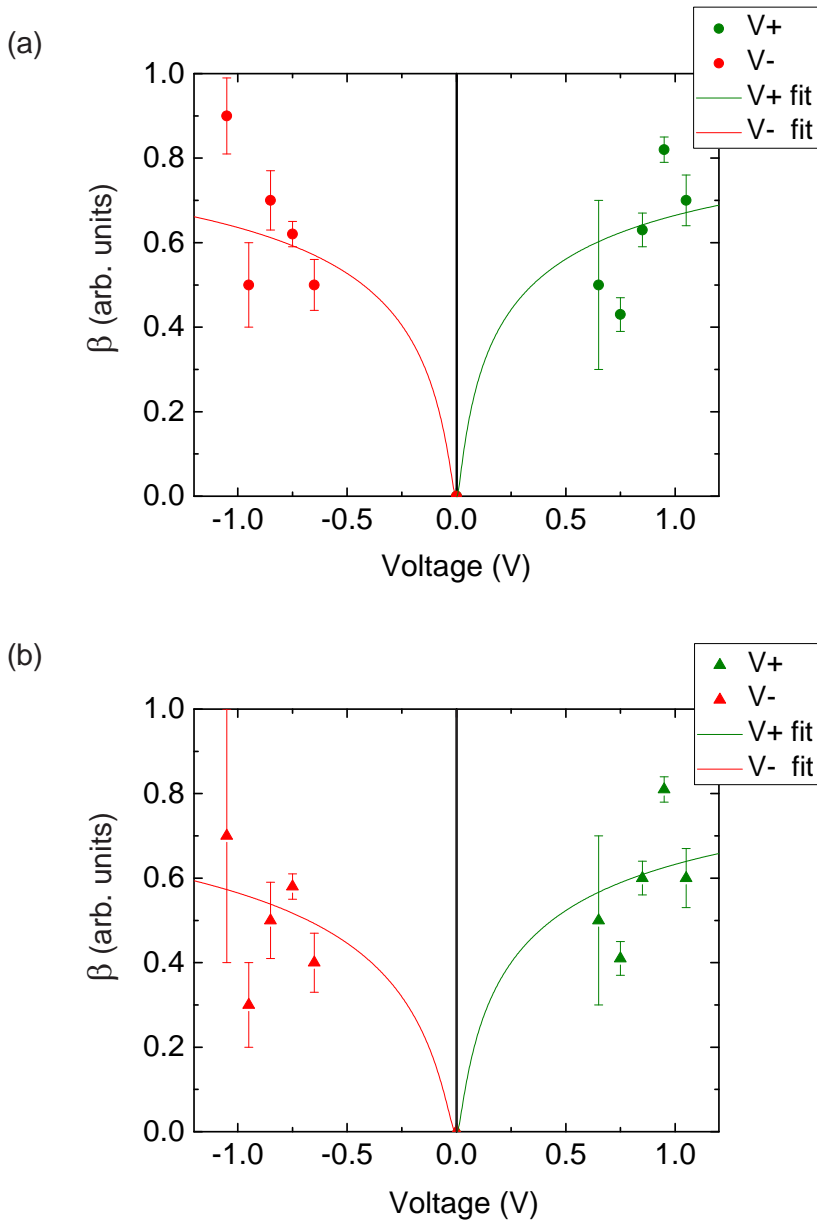


Figure 2.20: **Escape probability  $\beta$  as a function of voltage for  $X \leq 10$  nm.** (a)  $\beta(X)$  for all events. (b)  $\beta(X)$  for events excluding missing Co adatoms. Red and green lines represent exponential fits for negative and positive voltage, respectively.

## VOLTAGE - DISTANCE CHARACTERISTICS

The length of displacement of Co adatoms on the GNR ( $L$ ) for all voltage pulses  $V$  is plotted in Figure 2.21, where green and red dots indicate positive and negative voltage, respectively. Obviously, adatoms that went missing or that dropped onto the Au(111) surface are not included in this plot. Positive  $L$  values indicate motion of Co adatoms away from the tip while negative values indicate motion towards the tip. Voltage pulses that did not induce motion of adatoms ( $L = 0$ ) were not included in the graph for clarity (and they are also not included in the statistical averages). The average value of  $L$  for positive voltage pulses is  $L_+ = 0.2 \pm 0.2$  nm, whereas the average value of  $L$  for negative voltage pulses is  $L_- = 0.1^{+0.2}_{-0.1}$  nm. Both values are close to zero, indicating undetectable directional motion. In order to analyze whether  $L$  can be affected by the initial tip-adatom distance  $X$ , we also plotted the displacement  $L$  for different voltage pulses, separately for small  $X$  ( $\leq 10$  nm) and for large  $X$  ( $> 10$  nm), Figure 2.22(a), (b) respectively. The average displacement for small  $X$  is  $L_{-S} = 0.3 \pm 0.3$  nm and  $L_{+S} = 0.2 \pm 0.2$  nm. Large  $X$  gives average values of  $L_{-L} = -0.4 \pm 0.2$  nm and  $L_{+L} = 0.1^{+0.2}_{-0.1}$  nm. Again the values that we obtained are quite small, suggesting that

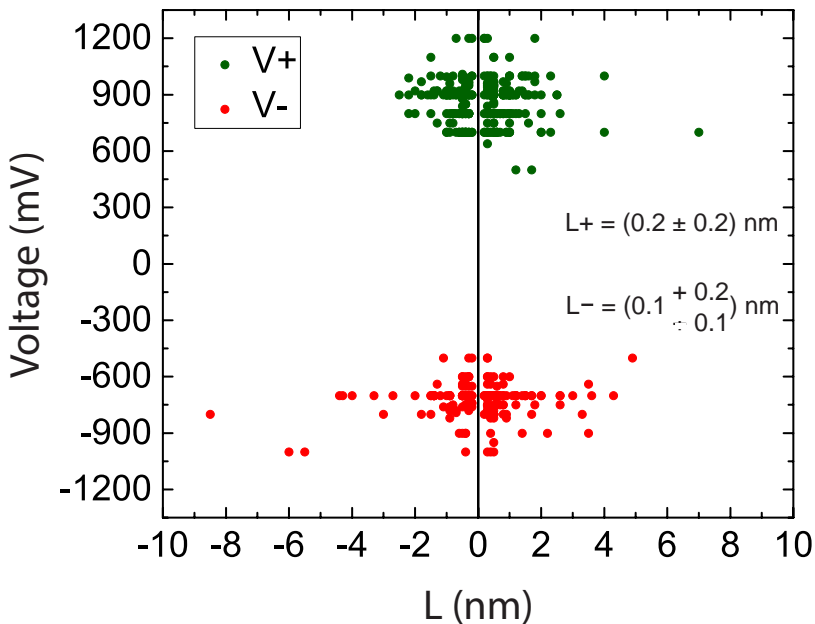


Figure 2.21: Displacement of Co adatoms ( $L$ ) after a voltage pulse  $V$ .  $L_+$  and  $L_-$  note average values of  $L$  for positive and negative voltage pulses, respectively.

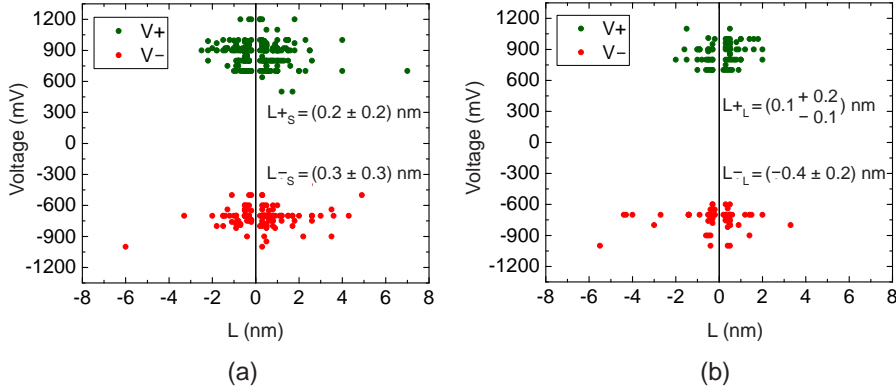


Figure 2.22: **Displacement of Co adatoms after voltage pulse V.** (a)  $L$  for  $X \leq 10$  nm. (b)  $L$  for  $X > 10$  nm.  $L_{+}$  and  $L_{-}$  note average values of  $L$  for positive and negative voltage pulses, respectively.

even if there is directional motion, the magnitude is at the border of our experimental resolution.

Figure 2.23 shows a histogram of the distance  $L$  traveled by adatoms after the voltage pulse, including the events for which no displacement was detected ( $L = 0$ ). Maximum observed values for  $L$  are  $-8.4$  nm and  $7.1$  nm. The green line is a fit of the right-hand side data (positive  $L$ ), excluding  $L = 0$ , to the 1-dimensional<sup>6</sup> random walk probability distribution  $P$  [68], with the hopping rate ( $v_p$ ) and a prefactor ( $A_p$ ) as fitting parameters. The fit is extrapolated to  $L = 0$  and mirrored to the left side.  $P$  is obtained by considering the probability for an atom to jump to the nearest-neighbor sites<sup>7</sup> along a straight line (see Appendix for more details). The red line is the equivalent fit to the negative  $L$  data set, with  $v_n$  and  $A_n$  as fitting parameters. Initial fitting with only the hopping rate as fitting parameter did not yield a good fit of both the  $L = 0$  bar and the tails of the distribution. Introducing a prefactor lowers the total probability from 1 to the value of  $A$  and ensures a good fit to all the data points except for  $L = 0$ . This will be discussed later in the chapter.

After several hundreds of pulses we observed that Co adatoms are removed from the GNR more often after negative voltage pulses compared to the positive ones of the same amplitude. Table 2.2 shows statistics for these missing Co adatoms after positive and negative voltage pulses. One can see that even for the lower average voltage amplitude ( $V_{\text{avg}}$ ) and larger average initial tip-adatom distance ( $X_{\text{avg}}$ ), the fraction of missing adatoms for negative bias voltage is more than two times larger

<sup>6</sup> Even though GNRs are 2-dimensional, in the first approximation it suffices to use this model

<sup>7</sup> A better fit of the theoretical probability distribution to the experimental data is obtained if the next-nearest-neighbor jumps are also taken into account [68, 69], however this single jumps approximation is adequate for a first approximation required in this analysis

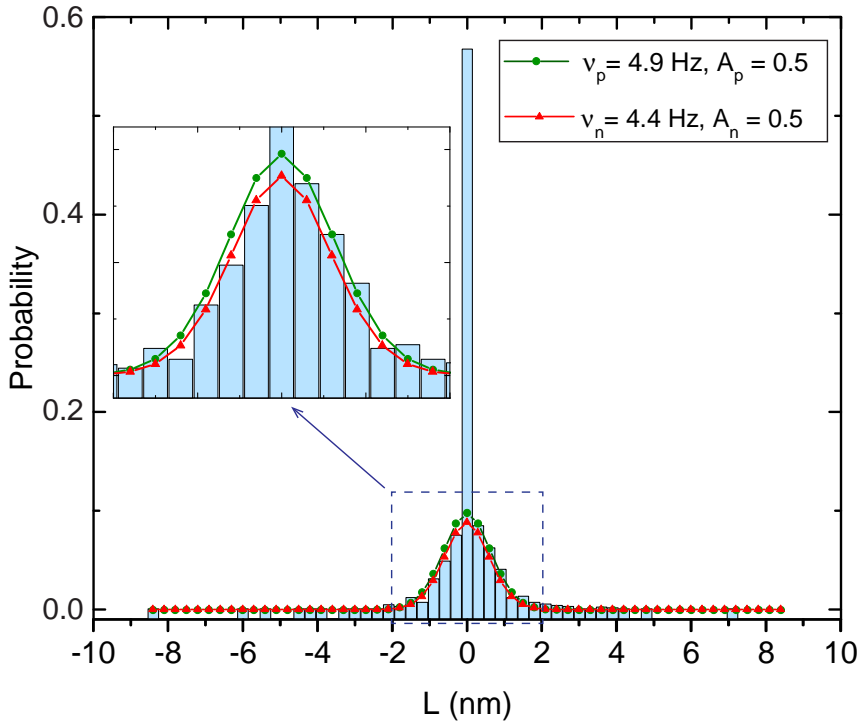


Figure 2.23: **Histogram of the distance traveled by Co adatoms along GNR after a voltage pulse ( $t \sim 0.5$  sec).** Positive (negative)  $L$  indicates motion away from (towards) the tip, while  $L = 0$  nm indicates Co adatoms that did not move. Green line is the fit of the positive  $L$  data to the 1-dimensional random walk probability distribution, excluding the data points for  $L = 0$ . Fit is extrapolated to  $L = 0$  and mirrored to the left side. Fitting parameters are the hopping rate  $v_p$ , ( $4.9 \pm 0.4$ ) Hz and a prefactor  $A_p$ , ( $0.5 \pm 0.3$ ). (see Appendix for details). Red line is the equivalent fit of the negative  $L$  values mirrored to the right side, with fitting parameters  $v_n = (4.4 \pm 0.4)$  Hz and a prefactor  $A_n$ , ( $0.5 \pm 0.3$ ). The inset shows zoom-in on the small area in a dashed box.

than for the positive one. This is one of the reasons why we limited the amplitude of negative voltage pulses to -1000 mV.

Positive voltage			Negative voltage		
Missing Co	$V_{\text{avg}}^+$	$X_{\text{avg}}^+$	Missing Co	$V_{\text{avg}}^-$	$X_{\text{avg}}^-$
9%	886 mV	7.3 nm	21%	-733 mV	8.2 nm

Table 2.2: **Statistics for missing Co adatoms for positive and negative voltage pulses.**  $V_{\text{avg}}^+$  and  $X_{\text{avg}}^+$  are the average voltage amplitude and initial tip-adatom distance for positive voltage pulses, while  $V_{\text{avg}}^-$  and  $X_{\text{avg}}^-$  correspond to negative voltage pulses.

## COBALT ADATOMS ON Au(111)

During voltage pulses on GNR we have sometimes observed motion of Co on Au(111) close to the GNR. Figure 2.24 shows an image scan before (a) and after (b) a voltage pulse of 800 mV on the GNR (green dot). It can be seen that a Co adatom on Au(111) close to GNR (yellow arrow) moves towards the GNR after the pulse.

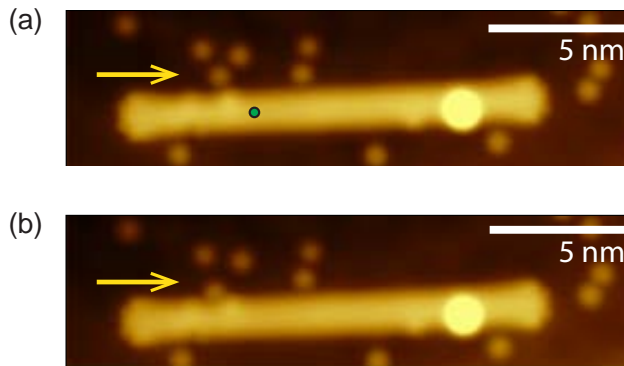


Figure 2.24: **Motion of Co on Au(111)**. STM images before (a) and after (b) a voltage pulse of  $V = 800$  mV on a GNR. The green dot indicates the place of the pulse. The yellow arrow points at the Co adatom on Au(111) that moved.

We have obtained statistics for voltage pulses on the GNR that moved Co adatoms on Au(111) within a range of 7 nm radius from the place of the pulse (first row in Table 2.3). This range was selected because it covers an area that is visible in most of the scans taken.

In order to make a quantitative comparison, we performed voltage pulses on gold to induce migration of Co adatoms on gold. We used the same procedure of lowering the tip and the same initial parameters as for Co on GNR ( $|I| \geq |\pm 0.3| \mu\text{A}$ ,  $V_b = 100$  mV) and we applied voltage pulses in the range of  $-1000 \text{ mV} \leq V_b \leq -600$  mV and  $600 \text{ mV} \leq V_b \leq 1200$  mV. Here we also take into account only Co adatoms on gold

Event	Displaced Co
Displacement of Co on Au(111) after pulse on GNR	391 / 6331 (6%)
Displacement of Co on Au(111) after pulse on Au(111)	16 / 519 (3%)
Displacement of Co on GNR after pulse on GNR	740 / 1504 (49%)

Table 2.3: **Overview of different pulsing events**. First number in the right column is the number of displaced Co adatoms and second number is the number of all Co adatoms in the area of interest. Last row corresponds to the statistics for Co on GNR from Table 2.1.

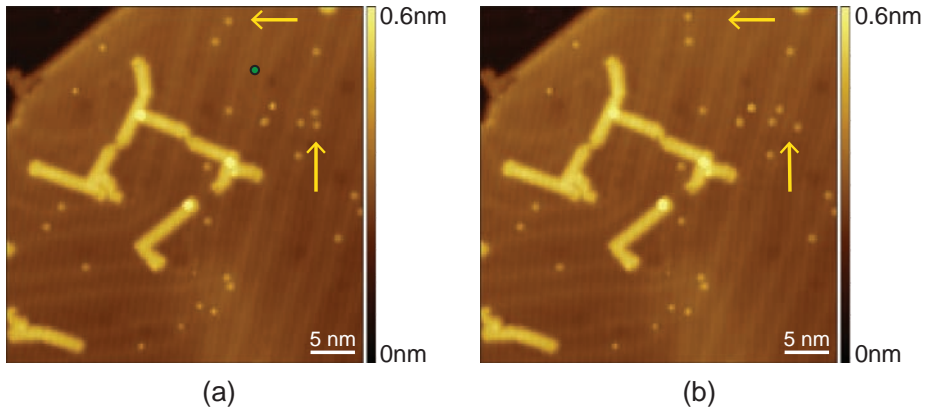


Figure 2.25: **Manipulation of Co adatoms on Au(111)**. STM images (a) before and (b) after a voltage pulse of 1200 mV (green dot). The area taken into account in the analysis is a circle of 7 nm radius from the green dot. The yellow arrows point at three Co adatoms that moved, and also serve as a reference marking the same position in both images.

that were within the 7 nm radius from the place of the pulse. Figure 2.25 shows STM images before (a) and after (b) a voltage pulse of 1200 mV applied at the position of the green dot. We can observe motion of several adatoms around the place of the pulse (two yellow arrows point at three Co adatoms that moved after the pulse). Obtained statistics for these events is shown in the second row of Table 2.3. Compared to migration of Co on GNR, the statistics shows that current-induced migration of Co adatoms on GNR (third row of Table 2.3) is much more effective than moving Co on Au(111). It also shows that motion of Co on Au(111) is nearly equally (in)effective for pulsing on GNR and Au(111).

We also observed that sometimes Co on Au(111) far away from the place of the pulse, but in the vicinity of the GNR, moves after voltage pulses on the GNR. Figure 2.26(a), (b) shows an example of such motion (the green dot marks the position of the tip during the pulse of 700 mV). We did not do an extensive quantitative analysis of these events (as mentioned before, they are not added to the statistics because the distance is larger than 7 nm).

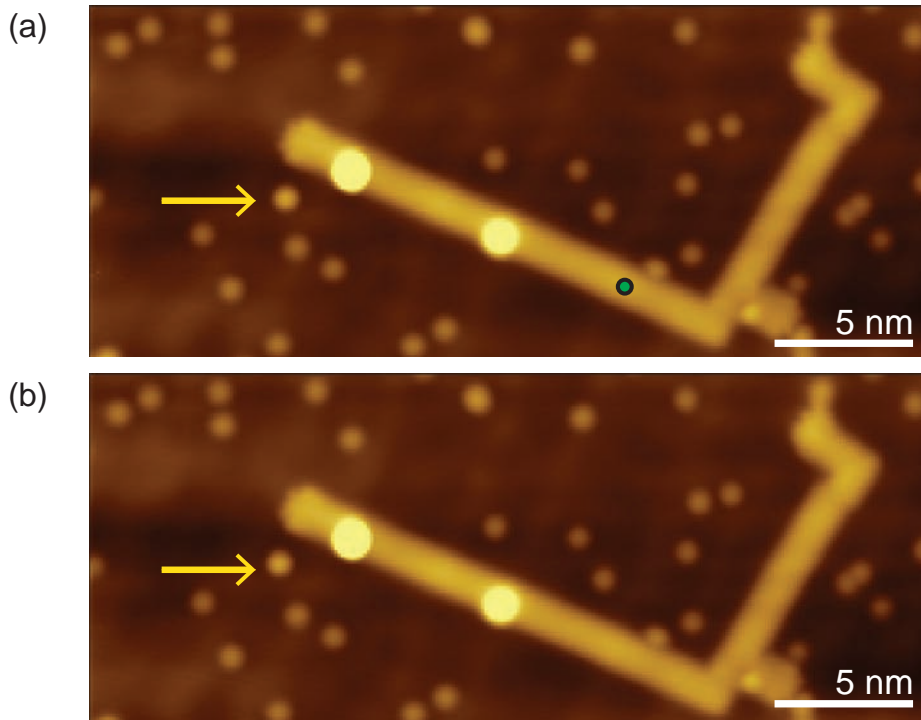


Figure 2.26: **Motion of Co on Au(111) in the vicinity of the GNR.** STM image before (a) and after (b) a voltage pulse of 700 mV (green spot). The yellow arrow points at Co adatom that moved, and also serves as a reference marking the same position in both images.

### 2.8.3. TEMPERATURE-DEPENDENT DIFFUSION MEASUREMENTS

In order to obtain more information on the relative excitation energies of Co adatoms on GNR and on Au(111), we performed a series of temperature-dependent diffusion measurements. Temperatures higher than 10 K were achieved by slowly heating the entire STM scan head, which is thermally weakly coupled to the helium bath. As temperature sensor we used a DT-470 diode sensor (Lake Shore Cryotronics) attached to the scan head. For our diffusion study, sequences of STM images were recorded at different temperatures. The temperature was raised from 8 K in steps of  $\sim 15$  K up to 79 K. For each step we waited several hours to reach thermal equilibration before starting the acquisition of image sequences. Co adatoms on Au(111) were already diffusing at 34 K. Figure 2.27 shows two STM images obtained at 46 K, where (a) is acquired 7 min before (b). Motion of a Co adatom on Au(111) is noticeable as the adatom is moved from its initial position (indicated by the yellow arrow), while the Co adatoms on the GNR remain unaffected.

Figure 2.27(a) confirms a well-known observation that adatoms prefer to sit at the corners of the herringbone. In other words, not all positions on Au(111) are equal, some lattice sites have a deeper energy well and are preferentially occupied [70]. We also observed that there are some sites on GNR from which it is very hard to remove Co adatoms. This could be due to the interaction of Co with adsorbates or with the herringbone reconstruction on gold below. Also as mentioned before, there is at least one type of such pinning site, which is a corner of a GNR which creates a stable position for Co adatom. This means that the escape probability may depend on the

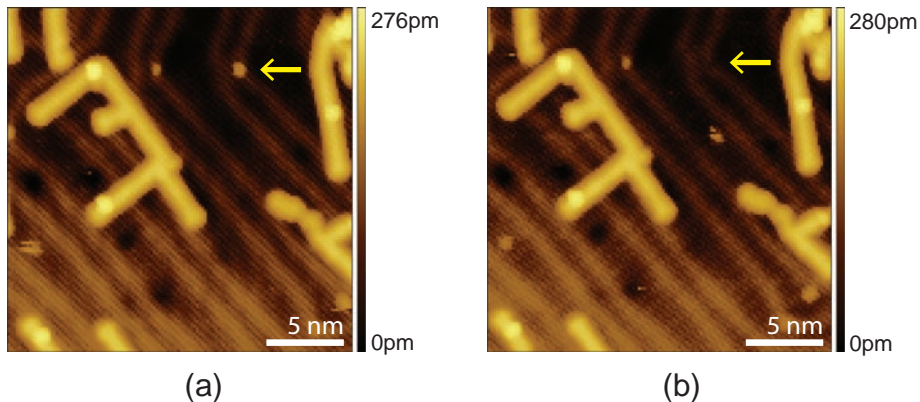


Figure 2.27: **Temperature-dependent diffusion measurement.** (a) STM image of the sample at 46 K. (b) STM image of the same area at the same temperature obtained 7 min after (a). The yellow arrow points at a Co adatom that moved, and also serves as a reference marking the same position in both images. The scan area is slightly shifted due to thermal drift.  $V_b = 0.1$  V,  $I = 1$  pA

initial positions of Co adatoms.

When 79 K was reached, the time required for the temperature to stabilize became very long, and we did not increase the temperature any further. Even at 79 K motion of Co on GNR was not observed, while most of the single Co on Au(111) could not be seen any longer (they either grouped up into clusters or possibly jumped towards the tip during scanning). Figure 2.28 shows an exemplary case of displacements of Co on Au(111) at 34 K, where  $L = 0$  corresponds to Co adatoms that did not move. Each  $L$  corresponds to a 0.3 nm wide set of values (e.g.  $L = 0.6$  nm takes all values from 0.45 to 0.75 nm). Yellow bars show the experimental probability distribution, while brown bars show the fit of a 2-D random walk on a triangular grid to the experimental data, with the hopping rate  $\nu$  as a fitting parameter (see Appendix for details). The fit gives the value of  $\nu = 0.025$  Hz.

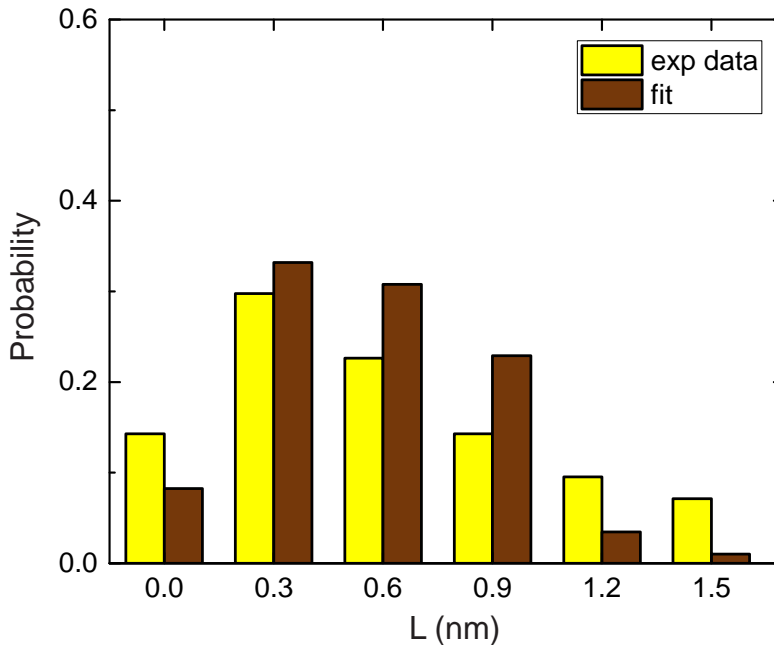


Figure 2.28: Comparison of the 2-D random walk (brown) and experimentally observed (yellow) probability distribution for displacement of Co ( $L$ ) on a triangular lattice of Au(111) at  $T = 34$  K. The values  $L = 0$  nm indicate Co adatoms that did not move. The calculated distribution corresponds to a hopping rate of  $\nu = 0.025$  Hz.

## 2.9. DISCUSSION

There are two mechanisms involved in the motion of adatoms after voltage pulses: Joule heating which results in a stochastic motion, and current-induced forces which, with the help of Joule heating needed to excite an atom out of its equilibrium position, would give preferred direction of motion. Figure 2.29 shows a schematic diagram of the path that the current (carrying a part of the heat) presumably takes after a voltage pulse from the STM tip. Thicker red arrows indicate higher current density. A large part of the current goes straight from the place of the pulse to bulk of gold. The remaining part of the current most likely spreads evenly along the GNR and seeps into the bulk of gold. When hot electrons are injected with the STM tip, there is a certain distance over which they will travel before thermalizing and the area within this radius will become equally hot. This area is represented with a red semicircle, with a center at the tip position on GNR and a radius of the mean free path (MFP) of the injected hot electrons and induced phonons in the GNR. In order to estimate the contribution of each mechanism (heat and current-induced forces), we need to look for evidence of directional motion of Co adatoms due to the part of the current flowing along the GNR.

We now turn to our experimental results. The first thing that we notice is that Co adatoms stay on GNRs after pulsing with the STM tip (only 0.4% of events showed adatoms to have dropped on gold). This suggests the presence of a potential barrier at the edges of GNRs which is much higher than the barrier for leaving the initial site. GNRs, therefore, provide a path for one-dimensional diffusion of Co adatoms.

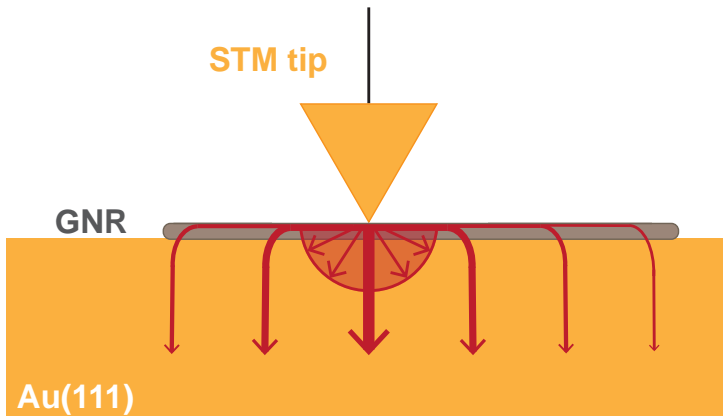


Figure 2.29: **Schematic diagram of the current flow.** The red arrows indicate split current paths from the STM tip during a voltage pulse. The red semicircle represents a hot spot around the place of the pulse. Thicker red arrows indicate higher current density.

From Figure 2.19(a) and (b) (which shows  $\Gamma(X)$  for all events and events excluding missing Co, respectively) we see that the first four data points (for  $X \leq 10$  nm) have similar values. When we consider the atoms as sitting in potential wells of depth  $E_D$ , the probability of escaping from this well should be determined by the local effective temperature. The constant level of  $\Gamma$  for the first few data points therefore points at a nearly constant temperature in this region. This suggests that the radius of the hot spot around the place of the pulse is  $\sim 10$  nm (which is presumably equivalent to the MFP of the injected electrons and induced phonons). Although still inside the accuracy margin, one may recognize a slight trend of the first three data points in Figure 2.19(b), which seems counter-intuitive: the escape probability for the larger  $X$  is higher than the one for the smaller  $X$ . This is actually consistent with the assumption that Co adatoms closest to the tip (i.e. smallest  $X$ ) are more likely to jump to the tip after a voltage pulse and disappear from the statistics. Since this graph does not show missing Co adatoms, this trend is to be expected. For  $X > 10$  nm,  $\Gamma$  decays by a factor of  $\sim 3$  over the distance of around 12 nm. This indicates the presence of a thermal gradient along the GNR with a hot spot around the place of the pulse and colder spots towards the ends of the GNR. It also implies that GNRs are in a close contact with gold surface: if they were isolated, the temperature of GNRs would be constant along their entire lengths, and in turn  $\Gamma$  would also be constant.

The fits to the escape probability  $\beta$  for positive and negative voltages in Figure 2.20 (green and red curves, respectively) show that the escape probabilities are symmetric for positive and negative bias voltage. In addition, average values for  $L$  obtained from the  $V(L)$  distribution (Figure 2.21) are the same, within experimental accuracy, for both voltage polarities, which indicates an overall lack of directionality of Co motion. The same conclusion can be drawn from the distribution for small  $X$  (Figure 2.22(a)) and the equal values obtained for  $L_{+S}$  and  $L_{-S}$ . The distribution for large  $X$  (Figure 2.22(b)) shows a slight directionality of Co motion towards the tip for  $V^-$ , however it is quite small ( $L_{-L} = -0.4 \pm 0.2$  nm). The symmetric distribution of diffusion in both directions is further confirmed by the red and green fits in Figure 2.23, which shows that the distributions left and right of  $L = 0$  are symmetric, to within experimental accuracy. In order to estimate whether preferred directionality of Co motion is expected for the range of voltages we used in the experiments, we need information on the GNR conductance and density of states which will tell us whether we are probing the electronic states of GNR or the surface states of the underlying gold.

### 2.9.1. GNR CONDUCTANCE

Grill *et al.* [60] calculated the conductance of a 7-AGNR, lifted off the surface of gold with the STM tip (Figure 2.30). Quite different slopes are obtained for high and low bias voltages. For low bias voltage of  $-0.5$  V (below the HOMO level) the conductance drops nearly exponentially with the effective GNR length spanning the junc-

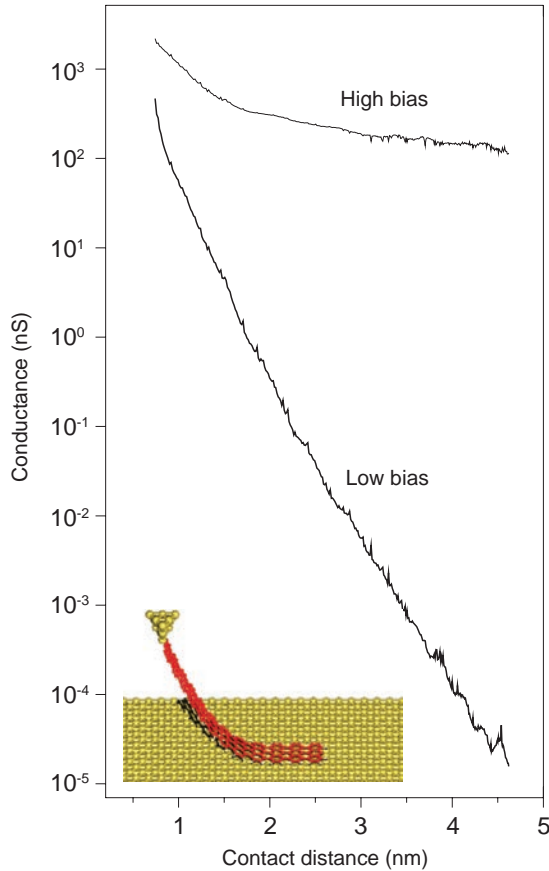


Figure 2.30: **Calculated conductance of a 5 nm AGNR in an STM pulling configuration as a function of effective molecular length in the junction.** Low bias =  $-0.5$  V (in the gap); high bias =  $-1.2$  V (matching HOMO level)). The high bias curve first decays (up to a contact distance of 1.5 nm) and then remains almost constant at larger contact distances. Image taken with permission from [60].

tion. Such a low conductance at small bias voltages is explained by the lack of overlap of two Tamm states<sup>8</sup> located at the opposite GNR termini, so they do not contribute to the conductance. For high (absolute) bias voltage of  $-1.2$  V (probing the HOMO level) the curve first decays (up to a contact distance of 1.5 nm), because the Tamm state contribution is captured at this stage, and then it stays almost constant at larger contact distances.

Fasel *et al.* [71] compared  $dI/dV$  spectra of an armchair GNR with  $N = 7$  (7-AGNR) on an insulating gold silicide monolayer (AuSIL) to the one on Au(111). The differential conductance  $dI/dV$  signal is obtained by positioning the tip of a scanning

<sup>8</sup> Tamm states are present close to the Fermi level at around 30 meV [60]

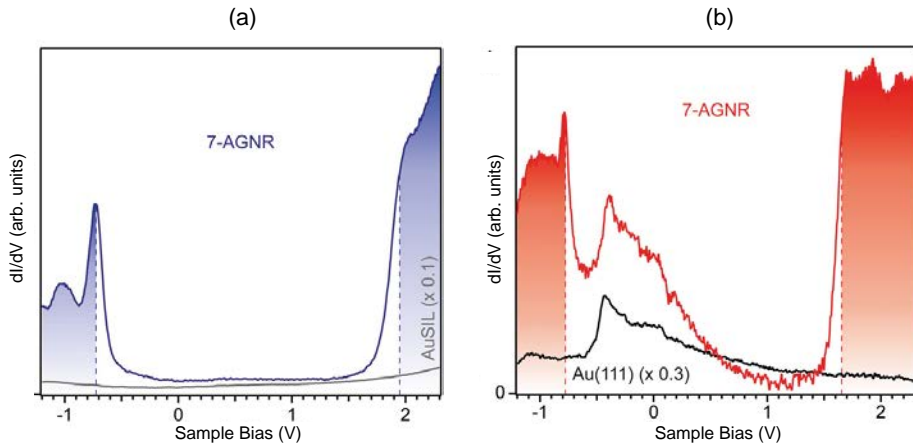


Figure 2.31: **Comparison of differential conductance spectra of 7-AGNR on an insulator and a metal** [71]. (a)  $dI/dV$  spectrum of a 7-AGNR on an insulating gold silicide (AuSIL). (b)  $dI/dV$  spectrum of a 7-AGNR on Au(111) substrate. The GNR spectrum is dominated by the Au(111) surface state. Image reproduced from [71] with permission.

tunneling microscope (STM) above the middle of the GNR and setting the tunneling gap to the desired value. The feedback loop is opened to allow the current to vary and the bias voltage is ramped from  $-1.5$  V to  $2.3$  V. The  $dI/dV$  signal is directly proportional to the local density of states (LDOS) of the sample at the position of the tip. Depending on the sign of applied bias, the occupied or the unoccupied states are probed. The  $dI/dV$  signal is recorded directly using an external lock-in amplifier. A small sinusoidal voltage modulation is added to the bias voltage, causing a sinusoidal response in the tunneling current. The amplitude of the modulated current is sensitive to the slope of the  $I$ - $V$  curve (hence, a  $dI/dV$  signal). The  $dI/dV$  signal is convoluted with the DOS of the tip, which is not constant. The results will vary from tip to tip, and the tip may even change in between STS measurements.

Due to suppression of Au(111) surface state by the silicide top layer,  $dI/dV$  spectra of 7-AGNR on AuSIL exhibit a featureless band gap region<sup>9</sup> (Figure 2.31(a)). Well-defined peaks at  $-0.7$  eV and  $2$  eV correspond to the valence band maximum and conduction band minimum, respectively. 7-AGNRs on Au(111) are dominated by the metal's surface state, which slowly decays into the vacuum in comparison to some GNR states that are found only in the vicinity of the ribbon [65]. As a result, the rapidly decaying GNR states might be obscured by substrate contribution in an STS measurement [72]. The most prominent contribution stems from Au(111) surface states with an onset at around  $-0.4$  V, as can be seen on Figure 2.31(b). For 7-AGNR on Au(111) the valence band maximum is at  $-0.8$  eV and the conduction band minimum is at  $1.6$  eV, resulting in a band gap of  $2.4$  eV.

<sup>9</sup> Even though it is referred to as gap,  $dI/dV$  is nonzero between HOMO and LUMO levels

From this we infer that for the range of positive bias voltages used in experiments ((0.6 - 1.2) V) the GNR behaves as a semiconductor (low conductance regime), whereas for negative bias voltages (-0.6 - 1) V electrons are injected into the HOMO level of the GNR and the behavior is expected to be metallic (we are in a high conductance regime, probing the HOMO level). We can now estimate the distribution of the current after a voltage pulse: for  $V+$  the current will mostly flow directly to the bulk of gold and we should not expect to see directional motion, whereas for  $V-$  the current will partially flow along the GNR and we could expect to see directionality towards the tip due to a current-induced wind force.

Even though we do observe a slight asymmetry in distribution for  $V-$  for large  $X$ , it is not statistically significant and we cannot identify current-induced forces from our measurements. We, therefore, conclude that migration of Co adatoms on GNR occurs mainly due to heating of the GNR. The GNR will be heated by the current, and this heat is carried away to the bulk of the Au substrate through the electrons and through lattice vibrations. Anticipating that there is an electronic and phononic barrier for this heat transport, the GNR will act as a line source of heat. We have observed motion of Co on Au(111) in the vicinity of the GNR far away from the voltage pulse on the GNR (Figure 2.26), which confirms efficient thermal transport along GNR. The reason why we do not observe significant directional motion of Co is likely due to the insufficient current density injected into the GNR.

It is worth mentioning that Lee *et al.* [73] in their recent paper demonstrate another source of asymmetry by which the electronic transmission characteristics of atomic-scale junctions are related to their heat dissipation properties. They show that depending on whether the molecule in the junction has electron- or hole-dominated electrical transport, the heat dissipation in the sample will be smaller (larger) for  $V-$  than  $V+$ . However, the difference in temperature increase for the two bias polarities is quite small (the order of a few mK) and would not be detectable in our system.

### 2.9.2. HOPPING RATE AND DIFFUSION BARRIER

The extrapolated fits of the one-dimensional random walk probability to positive and negative  $L$  data sets separately (Figure 2.23, green and red line, respectively) give values for the hopping rates of  $\nu_p = (4.9 \pm 0.4)$  Hz and  $\nu_n = (4.4 \pm 0.4)$  Hz. The values of the hopping rates are the same within the error, which further confirms that the motion is almost equally probable in both directions and that there is no detectable directional motion.

Around 50% of the voltage pulses did not result in the displacement of Co adatoms ( $L = 0$ ). There are several possible reasons for this. The first one is the stochastic (probabilistic) nature of hopping which implies that some of the adatoms will not always escape from the potential well after sufficient amount of energy is injected. Another reason is that during a voltage pulse Co adatom could hop away and back

to its initial position. The third possible reason is a deeper potential well of certain spots in which Co resides, which mean that our underlying assumption of a uniform potential well depth is invalid. As mentioned in the subsection 2.8.3, Co adatoms have preferred lattice sites on Au(111) (such as the corners of the herringbone). It is possible that similar preferred spots exist on GNR as well. One such example is the bend of the GNR from which it was not possible to move Co. The fit of the experimental data to a 1-D random walk function (Figure 2.23) gives us the information on these special sites. Since we found that we were forced to introduce the fitting prefactors in a 1-D random walk function ( $A_p = 0.5 \pm 0.3$ ,  $A_n = 0.5 \pm 0.3$ ) in order to have a good fit of the values for  $L \neq 0$ , the total integrated probability is then 50% (instead of 100%). The fact that the experimental value for  $L = 0$  is much higher than the fit value is a clear sign that there are exceptional sites on GNR with deeper energy wells from which adatoms are harder to move.

We can now obtain an estimate for a lower limit of the diffusion barrier for Co on GNR. The hopping rate  $\nu$  is given by

$$\nu = \nu_0 e^{-E_D/k_b T} \quad (2.6)$$

where  $\nu_0$  is the attempt frequency (typically an atomic vibration frequency of the order of  $10^{12}$  Hz),  $E_D$  is the diffusion barrier,  $k_b$  is Boltzmann constant and  $T$  is temperature. In the thermal diffusion experiment, at  $T = 79$  K we observe no motion of Co on GNR, which means that at this temperature the number of hops is less than one per image-to-image time interval of  $t = 180$  sec. If we take the number of hops to be  $\sim 0.5$ , we obtain the minimum of the diffusion barrier  $E_D \geq 0.2$  eV for Co adatoms on GNR<sup>10</sup>. Using this value of the lower limit of diffusion barrier, and the value for the hopping rate for Co on GNR obtained from the fitting ( $\nu_p$  or  $\nu_n$ ), we estimate the lower limit for temperature of GNR during the voltage pulse to be  $T_{\min} = 90$  K.

### 2.9.3. VERTICAL CO DISPLACEMENT

The statistics from Table 2.1 shows that in 9% of the cases Co adatoms were removed from the GNR ("missing" adatoms). We attribute these events to vertical displacement of Co adatoms towards the tip, rather than lateral motion along the GNR. The reason for this is that the largest potential drop is between the tip and the sample, so the electric field lines are oriented mostly perpendicular to the surface of GNR.

Vertical motion includes two mechanisms: excitation of vertical vibrations of the adatom and forces that attract the adatom towards the tip (direct force or Van der Waals forces). Since we have similar heating effect for  $V+$  and  $V-$  (Figure 2.20), this means that the electric field plays a key role in removing Co adatoms from the GNR.

The statistics from Table 2.2 shows that for missing Co adatoms there is asymmetry between  $V+$  and  $V-$ . One possibility for the asymmetry could be the higher

<sup>10</sup> By comparison, theoretical value for Co on pristine monolayer graphene obtained by DFT calculations is 0.76 - 1.32 eV, depending on the adsorption site [74]

work function of the sample with respect to the tip (discussed in section 2.4). Since the work function of the sample is 500 meV higher than the one of the tip, there is an additional attractive force between the sample and the tip due to the equilibration of the chemical potentials. This means that the effective field is smaller for positive bias (where the applied field helps to reduce the Kelvin potential) than for negative bias where it adds to it. As a consequence, adatoms would move easier towards the tip for  $V^-$ .

#### 2.9.4. ATOM AS A LOCAL THERMOMETER?

It is well known that diffusion of matter in a thermal gradient is directed away from hot spots and towards cold spots. Would it be possible to use single atom diffusion to detect temperature variations on the atomic scale? Theoretical work of Meair *et al.* [75] suggests that this could be a possibility: occupation of a hot spot by a single adatom should always lead to further adatom diffusion towards colder spots. This asymmetry in diffusion would in principle permit detecting temperature variations on the atomic scale, which could arise in structures such as the one in our experiment.

We concluded from Figure 2.19 that the hot spot on the GNR has a radius of  $\sim 10$  nm and the temperature drops with further increase of  $X$ . Based on diffusion in a thermal gradient, we would expect a directional component for  $X > 10$  nm. If the theory is applicable to our experiment, Co adatom in this range of  $X$  should always move towards the cold spots after the pulse, i.e. away from the tip. The statistics shows, however, that this is not the case, as  $L_{\text{avg}}$  for this data set has a value of  $0.1^{+0.2}_{-0.1}$  nm. If we want to observe the effect of thermal diffusion in a thermal gradient, a Co adatom has to make many hops. The first hop at a certain spot is still a random forward-backward motion even in a thermal gradient. It is only after many hops that one can effectively see a directionality in motion. The reason that we do not observe this directionality is that we have a global temperature gradient of a short duration (coming from a short voltage pulse) rather than a steady state in which the adatom has time to move away from hot spots. This suggests that the displacements of Co adatoms that we observe are mostly due to single hops or a few shorter hops within the short time of the voltage pulse.

#### 2.9.5. CO ON Au(111)

The statistics from Table 2.3 indicates that the induced migration of Co on GNR (row 3) is much more efficient than migration of Co on Au(111) (rows 1, 2), despite the fact that we find that the potential wells for Co on GNR are deeper than for Co on Au(111). In addition, comparison between rows 1 and 2 indicates that migration of Co on Au(111) was equally difficult whether the pulsing was done on GNR or Au.

The most likely explanation for the difficulty of moving Co on Au(111) lies in the

current and heat distribution (Figure 2.32). When we apply a voltage pulse on gold (top-left black dot), the electric and thermal transport are limited to the vicinity of the place of the pulse (indicated by round yellow shade) due to the ballistic electron transport through the bulk of gold, without affecting much nearby Co adatoms (local distribution). Also the heat is carried away mostly by the electrons, which is a process that is fast compared to the relaxation of the GNR where the most efficient heat transport is along the GNR (indicated by the color gradient along the GNR, where red color represents a hot spot of  $\sim 10$  nm radius). Rows 1 and 2 of the Table 2.3 suggest that the effect of pulsing on the GNR is very similar to pulsing on Au(111) when it comes to moving Co on Au(111). This implies that pulses on Au and on the GNR both lead to a local hot spot within a similar range over the Au surface (yellow shades; the dashed circle is for size comparison). Seeing how Co on Au(111) starts diffusing at around 34 K while Co on GNR does not move even at 79 K, we conclude that diffusion barrier for Co on Au(111) is much smaller than the one for Co on GNR. We also draw the conclusion that pulsing on the GNR heats the GNR to a much higher temperature than the Au surface, and that pulsing directly on gold leads to a similar modest local temperature rise of the Au surface as induced by pulsing on a GNR.

The diffusion barrier for Co on Au(111) is given by

$$E_d = -k_b T \ln\left(\frac{\nu}{\nu_0}\right) \quad (2.7)$$

where  $k_b$  is Boltzmann constant and  $\nu_0 \sim 1$  THz =  $10^{12}$  Hz. Using the average hopping rate  $\nu = 0.025$  Hz obtained from the fit of a two-dimensional random walk probability to experimental data at  $T = 34$  K, we obtained diffusion barrier for Co on gold  $E_{D_g} = 0.092$  eV. By comparison, the diffusion barrier for Co adatoms on Cu(111) is 0.01 - 0.4 meV, depending on the adsorption site [76].

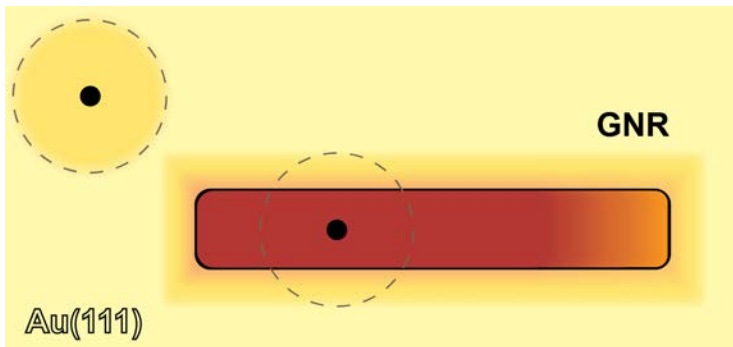


Figure 2.32: **Diagram of a heat distribution.** Black dots indicate place of the pulse on gold and GNR. Colors indicate different temperatures: yellow disc is temperature spread on gold and it is around the same size as the spread around GNR (dashed circle is for size comparison). Red color on GNR indicates the hot spot, with temperature gradually dropping with distance.

## 2.10. CONCLUSION & OUTLOOK

In summary, we have shown that it is possible to study one-dimensional migration of single Co adatoms on 7-AGNR on Au(111) by applying voltage pulses from an STM tip while in point-contact with GNRs. This experiment is the first step towards a detection of current-induced forces on a scale of single atoms. Interestingly, GNRs provide a lateral confinement due to the potential barrier at the edges, limiting the diffusion to be effectively one-dimensional, which makes the study of atomic diffusion a lot simpler. Although we inject electrons at negative bias polarity into the HOMO level of the GNR, analysis of escape probability and voltage-distance characteristics show no detectable directionality of Co migration which would come from current-induced forces. Slight directionality towards the tip for negative bias voltage is not significant enough to draw a definitive conclusion about detection of the wind force. The reason for this is most likely an insufficient current density along the length of the GNR. We infer that the observed motion of Co adatoms is mainly stochastic, under the influence of thermal excitations.

The statistics shows that it is much easier to move Co on GNRs than Co on Au(111). We attribute this to different current and heat distributions in the two substrates: voltage pulses on a GNR cause the entire GNR to become hot with a wide area of maximum temperature around the pulse, while on Au the heat is localized at the place of the pulse and quickly dissipated to the bulk. We have additionally performed temperature-dependent diffusion measurements in order to gain information on the relative energy barriers for Co adatoms on GNR and Au. Our findings suggest that there is a smaller relative barrier for Co on Au compared to the one on GNR, and that pulsing on GNR heats up the GNR to a much higher temperature than the Au surface, even when compared to pulsing directly on Au.

The experiment could be further improved by depositing GNR on a thin insulating layer (such as NaCl or hexagonal boron nitride), ideally with one end connected electrically to the substrate. This would confine the current within the whole GNR and also enable the GNR to stay hot for longer periods of time after the voltage pulse. Recent experiments have already demonstrated that it is possible to transfer a GNR from the metallic growth substrate onto insulating islands of NaCl, using the STM tip [77]. Going back to the initial experiments where we used CVD grown graphene, a possible improvement would be to decrease the width of the graphene patch to 30  $\mu\text{m}$ , which would yield a 10 times higher current density for the same value of  $I_{\text{max}}$ . Using such a small sample would require a method of tip guiding [78] to avoid crashing the tip onto the insulating  $\text{SiO}_2$  substrate. Regarding polymer contamination of graphene, an improvement would be to use a recently developed technique of graphene transfer in water, without using polymer [79], which would remove one polymer-deposition step. It should also be noted that  $\text{SiO}_2$  has corrugated surface and Co adatoms sitting in the dips might be harder to move, thus switching to a more

flat insulating substrate (such as quartz) would help overcome this problem.

## REFERENCES

- [1] M. Gerardin. *Compt. Rend. Acad. Sci. Paris*, 53:727, 1861.
- [2] W. B. Fiks. On the mechanism of the mobility of ions in metals. *Sov. Phys. Solid State*, 1:14–28, 1959.
- [3] H. B. Huntington. Electromigration in metals, in: *Diffusion in Solids - Recent Developments*, A. S. Nowick and J. J. Burton (Eds.). *Academic Press, New York*, 51:303, 1975.
- [4] C. Bosvieux and J. Friedel. *J. Phys. Chem. Solids*, 23, 1962.
- [5] R. S. Sorbello. Theory of electromigration, in: *Solid State Physics*, H. Ehrenreich and F. Spaepen (Eds.). 51, 1997.
- [6] A. Christou. Electromigration and Electronic Device Degradation. 1994.
- [7] R. E. Hummel. Electromigration and related failure mechanisms in integrated circuit interconnects. *International Materials Reviews*, 39:97–112, 2013.
- [8] A. J. Learn. Effect of structure and processing on electromigration-induced failure in anodized aluminum. *Journal of Applied Physics*, 44:1251 – 1258, 1973.
- [9] J. Cho and C. V. Thompson. Grain size dependence of electromigration-induced failures in narrow interconnects. *Appl. Phys. Lett.*, 54:2577 – 2579, 1989.
- [10] M. J. Attardo and R. Rosenberg. Electromigration Damage in Aluminum Film Conductors. *Journal of Applied Physics*, 41:2381 – 2386, 1970.
- [11] I. A. Blech and E. S. Meieran. Direct transmission electron microscope observation of electrotransport in aluminum thin films. *Appl. Phys. Lett.*, 11:263, 1967.
- [12] J. C. Blair, P. B. Gbate, and C. T. Haywood. Electromigration-induced failures in aluminum film conductors. *Appl. Phys. Lett.*, 17:281, 1970.
- [13] E. Arzt, O. Kraft, J. E. Sanchez, S. Bader, and W. D. Nix. Electromigration resistance and mechanical strength. *Mat. Res. Soc. Symp. Proc*, 239:677–682, 1992.
- [14] I. A. Blech. Electromigration in thin aluminum films on titanium nitride. *J. Appl. Phys.*, 47:1203–1208, 1976.
- [15] P. S. Ho and T. Kwok. Electromigration in metals. *Rep. Prog. Phys.*, 52:301–348, 1989.
- [16] C. Y. Liu, C. Chen, and K. N. Tu. Electromigration in Sn-Pb solder strips as a function of alloy composition. *Journal of Applied Physics*, 88:5703 – 5709, 2000.
- [17] S. Lin, Y. Liu, S. Chiu, Y. T. Liu, and H. Lee. Visualizing the Electron Scattering Force in Nanostructures. *Scientific Reports*, 7:3082, 2017.

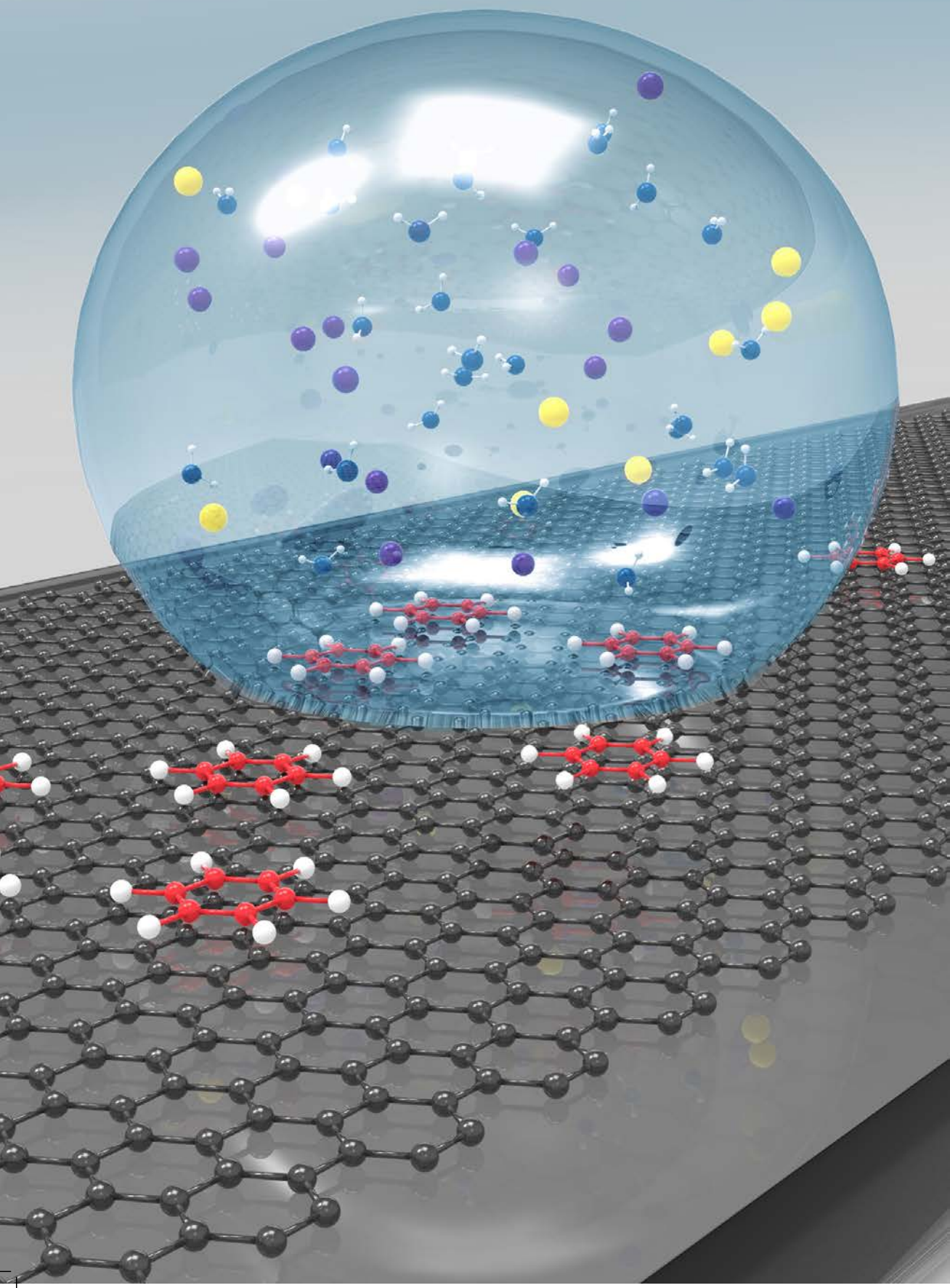
- [18] J. D. Verhoeven. Electrotransport as a means of purifying metals. *JOM*, 18:26–31, 1966.
- [19] B. C. Regan, S. Aloni, R. O. Ritchie, U. Dahmen, and A. Zettl. Carbon nanotubes as nanoscale mass conveyors. *Nature*, 428:924–927, 2004.
- [20] A. Barreiro, R. Rurali, E. R. Hernandez, and A. Bachtold. Structured Graphene Devices for Mass Transport. *Small*, 7:775 – 780, 2011.
- [21] H. Park, A. Lim, and P. Alivisatos. Fabrication of metallic electrodes with nanometer separation by electromigration . *Applied Physics Letters*, 75, 1999.
- [22] W. Liang, M. Shores, M. Bockrath, J. Long, and H. Park. Kondo resonance in a single-molecule transistor. *Nature*, 417:725–729, 2002.
- [23] H. Heersche, G. Lientschnig, K. O’Neill, H. van der Zant, and H. W. Zandbergen. In situ imaging of electromigration-induced nanogap formation by transmission electron microscopy. *Applied Physics Letters*, 91, 2007.
- [24] D. R. Strachan, D. E. Smith, D. E. Smith, T.-H. Park, Michael J. Therien, D. A. Bonnell, and A. T. Johnson. Controlled fabrication of nanogaps in ambient environment for molecular electronics. *Appl. Phys. Lett.*, 86:043109, 2005.
- [25] M. Rudneva, B. Gao, F. Prins, Q. Xu, H. S. J. van der Zant, and H. W. Zandbergen. In situ transmission electron microscopy imaging of electromigration in platinum nanowires. *Microscopy and Microanalysis*, 19:43–48, 2013.
- [26] F. Prins, T. Hayashi, B. J. A. de Vos van Steenwijk, B. Gao, E. A. Osorio, K. Muraki, and H. S. J. van der Zant. Room-temperature stability of pt nanogaps formed by self-breaking. *Appl. Phys. Lett.*, 94:123108, 2009.
- [27] J. J. Metois, J. C. Heyraud, and A. Pimpinelli. Steady-state motion of silicon islands driven by a DC current. *Surface Science*, 420:250–258, 1998.
- [28] C. Tao, W. G. Cullen, and E. D. Williams. Visualizing the Electron Scattering Force in Nanostructures. *Science*, 328:736 – 740, 2010.
- [29] O. Bondarchuk, W. G. Cullen, M. Degawa, and E. D. Williams. Biased Surface Fluctuations due to Current Stress. *Phys. Rev. Lett.*, 99:206801, 2007.
- [30] K. F. Braun, W. H. Soe, C. F. J. Flipse, and K. H. Rieder. Electromigration of single metal atoms observed by scanning tunneling microscopy. *APL*, 90:023118, 2007.
- [31] Y. Girard, T. Yamamoto, and K. Watanabe. Quantum-Chemical Interpretation of Current-Induced Forces on Adatoms on Carbon Nanotubes. *J. Phys. Chem. C*, 111:12478—12482, 2007.

- [32] D. Solenov and K. A. Velizhanin. Adsorbate Transport on Graphene by Electromigration. *Phys. Rev. Lett.*, 109:095504, 2012.
- [33] D. Dundas, E. J. McEniry, and T. N. Todorov. Current-driven atomic waterwheels. *Nature Nanotech.*, 4:99–102, 2009.
- [34] T. N. Todorov and D. Dundas. Nonconservative generalized current-induced forces. *Phys. Rev. B*, 81:075416, 2010.
- [35] N. Bode, S. V. Kusminskiy, R. Egger, and F. von Oppen. Scattering Theory of Current-Induced Forces in Mesoscopic Systems. *Phys. Rev. Lett.*, 107:036804, 2011.
- [36] J. Lü, T. Gunst, P. Hedegård, and M. Brandbyge. Current-induced dynamics in carbon atomic contacts. *Beilstein J. Nanotechnol.*, 2:814–823, 2011.
- [37] T. N. Todorov, D. Dundas, A. T. Paxton, and A. P. Horsfield. Nonconservative current-induced forces: A physical interpretation. *Beilstein J. Nanotechnol.*, 2:727–733, 2011.
- [38] J. Lü, M. Brandbyge, P. Hedegård, T. N. Todorov, and D. Dundas. Current-induced atomic dynamics, instabilities, and Raman signals: Quasiclassical Langevin equation approach. *Phys. Rev. B*, 85:245444–1, 2012.
- [39] J. Lü, M. Brandbyge, and P. Hedegård. Blowing the Fuse: Berry’s Phase and Runaway Vibrations in Molecular Conductors. *Nano Lett.*, 10:1657–1663, 2010.
- [40] C. Schirm, M. Matt, F. Pauly, J. C. Cuevas, P. Nielaba, and E. Scheer. A current-driven single-atom memory. *Nature Nanotech.*, 8:645–648, 2013.
- [41] C. Sabater, C. Untiedt, and J. M. van Ruitenbeek. Evidence for non-conservative current-induced forces in the breaking of au and pt atomic chains. *Beilstein J. Nanotechnol.*, 6:2338–2344, 2015.
- [42] K. S. Novoselov, A. K. Geim, S. V. Morozov, D. Jiang, Y. Zhang, S. V. Dubonos, I. V. Grigorieva, and A. A. Firsov. Electric Field Effect in Atomically Thin Carbon Films. *Science*, 306:666–669, 2004.
- [43] A. K. Geim and K. S. Novoselov. The rise of graphene. *Nature Materials*, 6:183–191, 2007.
- [44] C. Lee, X. Wei, J. W. Kysar, and J. Hone. Measurement of the Elastic Properties and Intrinsic Strength of Monolayer Graphene. *Science*, 321:385–388, 2008.
- [45] Y. W. Son, M. L. Cohen, and S. G. Louie. Half-metallic graphene nanoribbons. *Nature*, 444:347–349, 2006.

- [46] M. Fujita, K. Wakabayashi, K. Nakada, and K. Kusakabe. Peculiar Localized State at Zigzag Graphite Edge. *J. Phys. Soc. Jpn.*, 65:1920–1923, 1996.
- [47] K. Nakada, M. Fujita, G. Dresselhaus, and M. S. Dresselhaus. Edge state in graphene ribbons: Nanometer size effect and edge shape dependence. *Phys. Rev. B*, 54:17954–17961, 1996.
- [48] L. Yang, C. Park, Y. Son, M. L. Cohen, and S. Louie. Quasiparticle Energies and Band Gaps in Graphene Nanoribbons. *Phys. Rev. Lett.*, 99:186801, 2007.
- [49] Y.-W. Son, Cohen, M. L., and S. G. Louie. Energy gaps in graphene nanoribbons. *Phys. Rev. Lett.*, 97:216803, 2006.
- [50] V. Barone, O. Hod, and G. E. Scuseria. Electronic structure and stability of semi-conducting graphene nanoribbons. *Nano Lett.*, 6:2748–2754, 2006.
- [51] A. Kimouche, M. M. Ervasti, R. Drost, S. Halonen, A. Harju, P. M. Joensuu, J. Sainio, and P. Liljeroth. Ultra-narrow metallic armchair graphene nanoribbons. *Nature Commun.*, 6:10177, 2015.
- [52] G. Binnig and H Rohrer. Scanning tunneling microscopy. *Surface Science*, 126:236–244, 1983.
- [53] G. Binnig, C. F. Quate, and Ch. Gerber. Atomic Force Microscope. *Phys. Rev. Lett.*, 56:930, 1986.
- [54] P. Grünther, U. Ch. Fischer, and Dransfeld K. Scanning near-field acoustic microscopy. *Applied Physics B*, 48:89–92, 1989.
- [55] Lord Kelvin. Contact electricity of metals. *Phil. Mag.*, 18:26–31, 1898.
- [56] K. Besocke. An easily operable scanning tunneling microscope. *Surface Science*, 181:145–153, 1987.
- [57] J. Frohn, J. F. Wolf, K. Besocke, and M. Teske. Coarse tip distance adjustment and positioner for a scanning tunneling microscope. *Review of Scientific Instruments*, 60, 1989.
- [58] J. Moser, A. Barreiro, and A Bachtold. Current-induced cleaning of graphene. *Applied Physics Letters*, 91:163513, 2007.
- [59] M. R. Amirzada, A. Tatzel, V. Viereck, and H. Hillmer. Surface roughness analysis of SiO<sub>2</sub> for PECVD, PVD and IBD on different substrates. *Applied Nanoscience*, 6:215–222, 2015.
- [60] M. Koch, F. Ample, C. Joachim, and L. Grill. Voltage-dependent conductance of a single graphene nanoribbon. *Nature Nanotechnology*, 7:713–717, 2012.

- [61] J. Cai, P. Ruffieux, R. Jaafar, M. Bieri, T. Braun, S. Blankenburg, M. Muoth, A. P. Seitsonen, M. Saleh, X. Feng, K. Müllen, and R. Fasel. Atomically precise bottom-up fabrication of graphene nanoribbons. *Nature*, 466:470–473, 2010.
- [62] V. W. Brar, R. Decker, H. M. Solowan, Y. Wang, L. Maserati, K. T. Chan, H. Lee, C. O. Girit, A. Zettl, S. G. Louie, M. L. Cohen, and M. F. Crommie. Gate-controlled ionization and screening of cobalt adatoms on a graphene surface. *Nature Physics*, 7:43–47, 2010.
- [63] A. Ishii, M. Yamamoto, H. Asano, and K. Fujiwara. DFT calculation for adatom adsorption on graphene sheet as a prototype of carbon nanotube functionalization. *Journal of Physics: Conference Series*, 100:052087, 2008.
- [64] A. Basagni, F. Sedona, C. A. Pignedoli, M. Cattelan, L. Nicolas, M. Casarin, and M. Sambri. Molecules-oligomers-nanowires-graphene nanoribbons: A bottom-up stepwise on-surface covalent synthesis preserving long-range order. *J. Am. Chem. Soc.*, 137:1802–1808, 2015.
- [65] H. Huang, D. Wei, J. Sun, S. L. Wong, Y. P. Feng, A. H. C. Neto, and A. T. S. Wee. Spatially Resolved Electronic Structures of Atomically Precise Armchair Graphene Nanoribbons. *Scientific Reports*, 2:983, 2012.
- [66] T. Dienel, S. Kawai, H. Söde, X. Feng, K. Müllen, P. Ruffieux, R. Fasel, and O. Gröning. Resolving Atomic Connectivity in Graphene Nanostructure Junctions. *Nano Letters*, 15:5185–5190, 2015.
- [67] T. N. Todorov. Local heating in ballistic atomic-scale contacts. *Philosophical Magazine B*, 77:965–973, 1998.
- [68] J. D. Wrigley, M. E. Twigg, and G. Ehrlich. Lattice walks by long jumps. *J. Chem. Phys.*, 93:2885, 1990.
- [69] T. R. Linderoth, S. Horch, E. Lægsgaard, I. Stensgaard, and F. Besenbacher. Surface Diffusion of Pt on Pt(110): Arrhenius Behavior of Long Jumps. *Phys. Rev. Lett.*, 78:4978 – 4981, 1997.
- [70] J. Repp, W. Steurerand, I. Scivetti, M. Persson, L. Gross, and G. Meyer. Charge-state-dependent diffusion of individual gold adatoms on ionic thin nacl films. *Phys. Rev. Lett.*, 117:146102, 2016.
- [71] O. Deniz, C. Sanchez-Sanchez, T. Dumsloff, X. Feng, A. Narita, K. Müllen, N. Kharche, V. Meunier, R. Fasel, and P. Ruffieux. Revealing the Electronic Structure of Silicon Intercalated Armchair Graphene Nanoribbons by Scanning Tunneling Spectroscopy. *Nano Lett.*, 17:2197–2203, 2017.

- [72] H. Söde, L. Talirz, O. Gröning, C. A. Pignedoli, R. Berger, X. Feng, K. Müllen, R. Fasel, and P. Ruffieux. Electronic Band Dispersion of Graphene Nanoribbons via Fourier-Transformed Scanning Tunneling Spectroscopy. *Phys. Rev. B: Condens. Matter Mater. Phys.*, 4:45429, 2015.
- [73] W. Lee, K. Kim, W. Jeong, L. A. Zotti, F. Pauly, J. C. Cuevas, and P. Reddy. Heat dissipation in atomic-scale junctions. *Nature*, 498:209—212, 2013.
- [74] Y. Tang, H. Zhang, Z. Shen, M. Zhao, Y. Li, and X. Dai. The electronic and diffusion properties of metal adatoms on graphene sheets: a first-principles study. *RSC Advances*, 7:33208, 2017.
- [75] J. Meair, J. P. Bergfield, C. A. Stafford, and Ph. Jacquod. Local temperature of out-of-equilibrium quantum electron systems. *PRB*, 90:035407, 2014.
- [76] R. Huang, Y. Sun, C. Du, T. Gao, Y. Wu, and V. Stepanyuk. Stm-mediated atom motion: a Co atom and mixed CoCu<sub>n</sub> chains on a Cu(111) surface. *Eur. Phys. J. B*, 86:429, 2013.
- [77] S. Wang, L. Talirz, C. A. Pignedoli, X. Feng, K. Muellen, R. Fasel, and P. Ruffieux. Giant edge state splitting at atomically precise zigzag edges. *Nature Communications*, 7, 2015.
- [78] J. M. de Voogd, M. A. van Spronsen, F. E. Kalf, B. Bryant, O. Ostojić, A. M. J. den Haan, I. M. N. Groot, T. H. Oosterkamp, A. F. Otte, and M. J. Rost. Fast and reliable pre-approach for scanning probe microscopes based on tip-sample capacitance. *Ultramicroscopy*, 181:61–69, 2017.
- [79] L. A. Belyaeva, P. M. G. van Deursen, K. I. Barbetsea, and G. F. Schneider. Hydrophilicity of Graphene in Water through Transparency to Polar and Dispersive Interactions. *Advanced Materials*, 30:1703274, 2018.



# 3

## INDUCING VOLTAGE BY MOVING A DROPLET OF LIQUID ALONG GRAPHENE

*Immersed graphene cannot generate a voltage signal from a flowing ionic liquid [1, 2]. However, voltage can be induced by moving a droplet of liquid along a strip of graphene [3]. Here we demonstrate this effect with aqueous solutions of NaCl, benzenesulfonic acid (HBSA) and sodium benzenesulfonate (NaBSA). The results suggest that in the case of NaCl, ions are confined to the droplet, whereas for NaBSA and HBSA droplets,  $\text{BSA}^-$  and  $\text{H}_3\text{O}^+$  ions have such strong adhesion to the substrate that they leave the droplet and adsorb to graphene/PET interface, forming a charged layer. This is revealed by the voltage signal observed when moving a drop of deionized water along this charged graphene surface. We argue that the reason for this effect lies in the polarizability of the water, which has a large contribution to the voltage signal.*

*We further apply a voltage across the graphene sheet in an attempt to demonstrate the reverse effect and induce motion of the NaCl droplet under the influence of electromigration forces. Components of electromigration force, direct and wind forces, are known to induce motion of material in conductors and semimetals. We do not observe motion of the droplet even when the sticking force of the droplet to the substrate is minimized by introducing a tilt of the stage. We propose that this can be explained in terms of a neutral layer, composed of positive and negative charges in the droplet, which will experience no net direct force. The wind force is much smaller than our detection limit.*

---

To be published as: "Inducing voltage by moving a droplet of liquid along graphene", S. Vrbica<sup>1</sup>, T. Vlot<sup>1</sup> and J. van Ruitenbeek<sup>1</sup>

<sup>1</sup>Huygens-Kamerlingh Onnes Laboratorium, Universiteit Leiden, The Netherlands.

### 3.1. INTRODUCTION

Electrokinetic phenomena include phenomena involving fluid motion adjacent to a charged surface. Electrokinetics has been developed in close connection with the theories of the electrical double layer and of electrostatic surface forces [4]. In 1853 German physicist Hermann von Helmholtz realized that a charged conductor immersed in electrolyte solutions attracts counterions to its surface [5] due to electrochemical interaction. The two layers of opposite charges at the interface between a conductor and electrolyte form a so-called *electric double layer* (EDL). This early model introduces a linear potential drop with the distance from the surface of the conductor and does not take into account thermal motion or ion diffusion, among other effects. In 1910 this Helmholtz model was improved by Gouy and Chapman, who introduced a diffuse model of the double layer in which potential drops exponentially with the distance from the surface of the conductor. This model cannot be successfully applied to highly charged double layers, so in 1924 Otto Stern combined the Helmholtz model with the Gouy-Chapman model. Figure 3.1 schematically illustrates Stern's model of the EDL in which some ions adhere to the conductor (as suggested by Helmholtz) forming the so-called Stern layer, while other charges form a diffuse (or Gouy-Chapman) layer. According to this model, beyond the Stern plane, interactions in electrolytes decay exponentially with distance, with the Debye screening length ( $\lambda_D$ ) setting the characteristic length scale.

Flow sensors and devices that collect electricity from flowing water are important for the harvesting of electric power and the characterization of electrochemical properties. These devices rely on the principle of streaming potential, an electrokinetic phenomenon in which an electric potential is generated by driving an electrolyte through narrow pores under a pressure gradient [7, 8]. In 2001 Kral *et al.* theoretically proposed that carbon nanotubes (CNTs) in flowing liquids could generate an electric current [9], and since then several research groups have demonstrated induced voltage in CNTs, when being immersed in flowing water or polar liquids [10–12]. However, there are disparities in the experimental data, and different theories for the observed effects have been proposed, none of them yet able to provide a satisfactory explanation for all the observed phenomena. More interestingly, Dhiman *et al.* reported that a graphene sheet mounted on Si/SiO<sub>2</sub> submerged in a flowing HCl solution can generate voltages [2]. Their molecular dynamics simulations indicate that the flow-induced voltage in graphene is primarily caused by a net drift velocity of Cl<sup>-</sup> ions adsorbing/desorbing or hopping on graphene surface.

Unfortunately, their findings were challenged by Yin *et al.* [1] who argued that the signal actually comes from the exposed metal electrodes in the solution. Water flow over the graphene-electrode system induces the voltage, while the graphene mainly behaves as a load connected between the electrodes. Once the electrodes were isolated from interacting with the solution, no measurable voltage could be induced

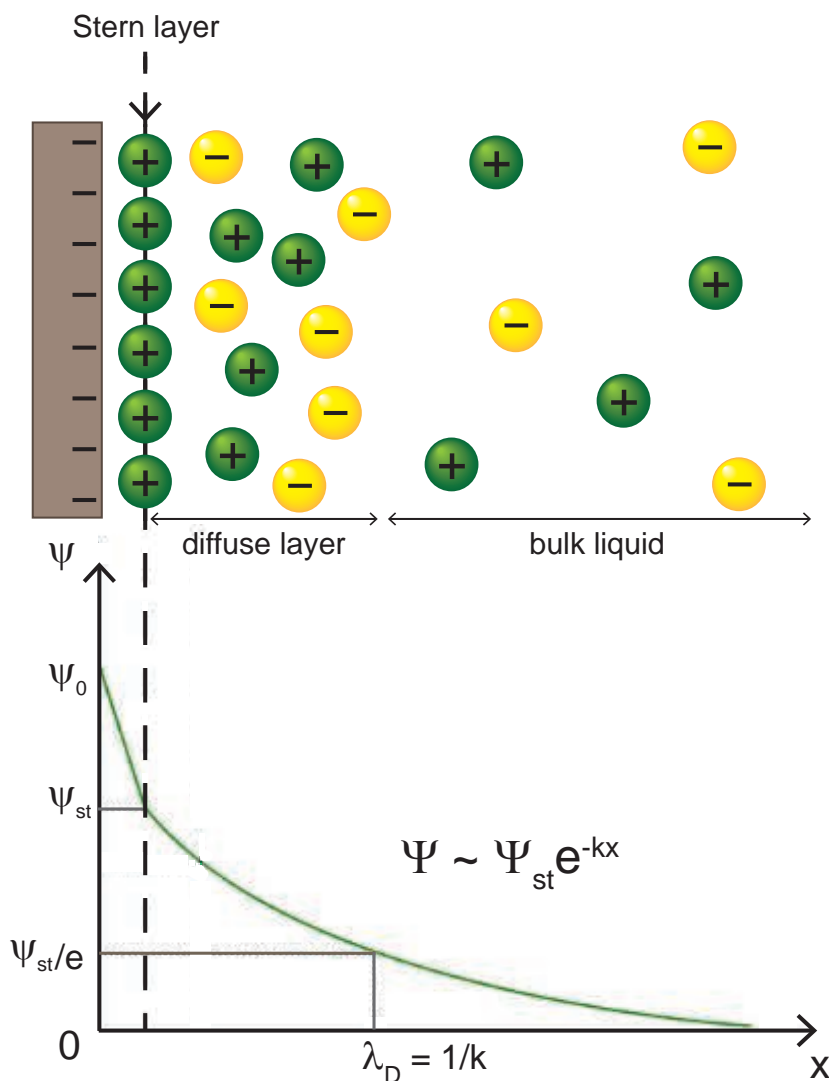


Figure 3.1: **Schematic illustration of electrical double layer (EDL) at the solid-electrolyte interface according to Stern's model** [6]. The negatively charged conductor attracts positive charges from the electrolyte, which form a dense layer at its surface (so-called Stern layer). Counterions are attracted to the Stern layer via the Coulomb force, forming a so-called diffuse (Gouy-Chapman) layer which screens the net surface charge over a characteristic Debye length,  $\lambda_D$ . The potential  $\Psi$  across the Stern layer drops linearly and across the diffuse layer it drops exponentially.

by the flow over mono-, bi- and trilayered graphene samples in the same solution. Their first principles calculations (DFT) reveal that the hydronium  $\text{H}_3\text{O}^+$  cation in the water adsorbs onto graphene and forms strong covalent bonds, while  $\text{Cl}^-$  an-

ion is repelled from graphene because of its negative adsorption energy. This is in contrast to molecular dynamics simulations of Dhiman *et al.* which indicate that the  $\text{H}_3\text{O}^+$  cation has a weak interaction with the graphene while the  $\text{Cl}^-$  anion can adsorb to graphene. The result that immersed graphene cannot generate a voltage from a flowing liquid was subsequently confirmed by the work of Newaz *et al.* [13] in which graphene transistors were used to detect the streaming potential, and no fluid-flow-induced electrical current was induced in the graphene.

Yin *et al.* [1] also show that a CNT film immersed in the flowing HCl water generates a voltage (although the electrodes are covered), with a signal sign unchanged when reversing the flow direction. The authors argue that the reason behind this is that the CNT film contains a lot of metal catalyst particles during the growth process [14, 15], which can interact with solution to produce measurable voltages. Generating electricity in graphene and CNTs in flowing liquids without a pressure gradient remains a challenge.

Nevertheless, there is a way to induce a voltage in a graphene sheet: with the help of a novel electrokinetic phenomenon, called the *drawing potential* [3].

### 3.1.1. DRAWING POTENTIAL AND FORMATION OF A PSEUDOCAPACITOR

In their more recent work, Yin *et al.* [3] show that a voltage of the order of a few millivolts can be induced by moving a droplet of ionic solution along a graphene strip on poly-ethylene terephthalate (PET) substrate. They refer to this effect as the drawing potential. They propose that the drawing potential is generated when a pseudocapacitor, formed at the interface of the droplet and graphene, is driven along the graphene strip, charging and discharging at the boundary of the droplet. Their density functional theory (DFT) calculations show that for graphene in contact with a NaCl aqueous solution,  $\text{Na}^+$  ions are adsorbed on the graphene with an adsorption energy of over 2 eV, while  $\text{Cl}^-$  ions move away from the graphene due to their negative adsorption energy [1]. DFT calculations also show that the adsorbed  $\text{Na}^+$  ions draw electrons towards the upper surface of the graphene (Figure 3.2(a)). The positive  $\text{Na}^+$  layer and negative electron layer thus form a pseudocapacitor. As the distance between these two layers is only  $\sim 0.4$  nm, the formed pseudocapacitance is very large.

Based on DFT calculations, Shi *et al.* [16] and Tsai *et al.* [17] also argue that cations ( $\text{Na}^+$ ) from an electrolytic solution would preferentially adsorb on graphene. However, Yang *et al.* [18] in their recent paper show that the surface dipole layer of the underlying substrate is actually the one responsible for adsorption of ions at the graphene surface, which leads to electricity generation in graphene. Graphene itself does not attract ions, but only appears as a weak screening layer for the dipole field and serves as a passive conductive path for the generated current. Comparison between substrates materials PET and poly-methyl methacrylate (PMMA) shows that positive voltage spikes (corresponding to positive ions attracted to the water/graphene

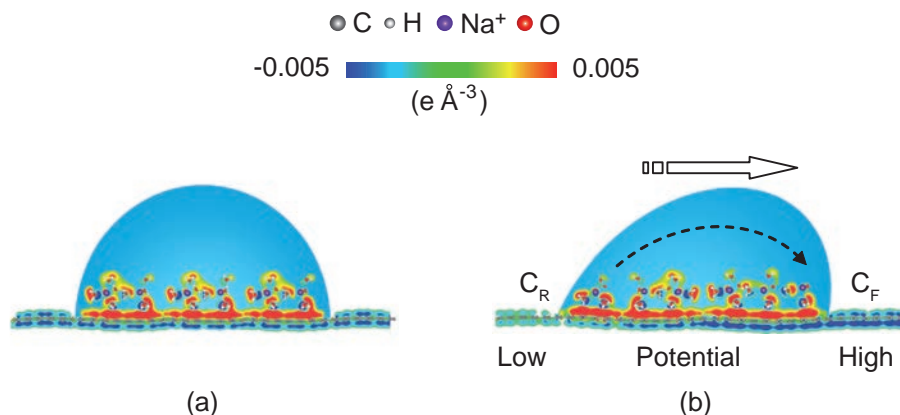


Figure 3.2: **Mechanism for the drawing potential.** (a) Schematic illustration of the pseudocapacitance formed by a static droplet on graphene. (b) Schematic illustration of the potential difference induced by a moving droplet. Color indicates DFT results for the distribution of differential charge near monolayer graphene caused by adsorbing hydrated sodium cations. Image reproduced from Yin *et al.* [3] with permission.

interface), generated when moving drops of NaCl aqueous solution over the surface are observed on graphene/PET. However, on graphene/PMMA they are not detected, which suggests that the PET substrate attracts  $\text{Na}^+$  ions much more strongly than PMMA. Yang *et al.* explain the origin of  $\text{Na}^+$  ion adsorption at the interface with the presence of a dipole on the substrate. The surface of a polymer can often be polar with a certain molecular group polar-oriented at the surface. If the group has a strong dipole, the polymer should possess a strong surface dipole layer that can attract ions. The question is: how can a surface dipole layer attract  $\text{Na}^+$  from solution to have it adsorbed on graphene/PET? The continuum theory of electrostatics states that an infinite continuum of surface dipole layer has no field outside the layer. In reality, however, surface dipoles associated with molecular groups reside at discrete positions on the surface. While such local dipoles are of very short range, they create a local potential well on top of each dipole that can trap ions [19].

Going back to the formation of the pseudocapacitor, Yin *et al.* [3] argue that for a static NaCl droplet on graphene the charge redistributes uniformly over the interface of the droplet with the graphene, and there is no potential difference between its left and right sides (Figure 3.2(a)). When the droplet is drawn along the graphene, ions are adsorbed at the front end, advancing the pseudocapacitor forward and drawing electrons in the graphene. At the same time, ions are desorbed at the rear end of the droplet, discharging the pseudocapacitor and releasing the electrons to the graphene. This process gives rise to an increase/decrease in electron density behind/ahead of the moving droplet (Figure 3.2(b)) compared to the static state, resulting in a higher potential at the front than at the rear. The authors also show that the

drawing potential depends on the ion species, as expected from the electric double-layer theory. The signal of aqueous solutions of HCl is stronger than that for NaCl solutions, for the same droplet size, concentration and velocity. In addition, the sign of the induced voltage is reversed compared to that for NaCl. The authors argue that due to a high affinity of  $\text{H}_3\text{O}^+$  ions to the graphene, the latter ions are strongly adsorbed on the graphene, such that they leave the droplet when it moves over the surface. The adsorbed layer of  $\text{H}_3\text{O}^+$  ions behaves like a positively charged sheet, attracting the  $\text{Cl}^-$  ions to the lower surface of the solution. The  $\text{Cl}^-$  ions now play the role of dynamic charges in the droplet that attract mobile positive charges (equivalent to repelling negative charges) inside the graphene sheet. This causes the sign of the induced voltage for HCl to be reversed, compared to the NaCl droplet for motion in the same direction. The authors also report on the reduced droplet contact angle on graphene that has been wetted by a HCl solution, even after rinsing with deionized water for 30 min. This supports the idea of the strong adsorption of the  $\text{H}_3\text{O}^+$  on graphene. In addition to the ionic composition, several other factors determine the magnitude and sign of the voltage created: the velocity of the droplet, the direction of motion, the length of the droplet, its volume, the number of droplets and the concentration of the ions in the solution. All these factors lead to simple linear relationships that are in agreement with the simple pseudocapacitor picture presented above. The authors also claim that no detectable drawing potential for deionized water is found, as nearly no ions are present to form the pseudocapacitor.

### 3.1.2. SODIUM BENZENESULFONATE (NaBSA) AND BENZENESULFONIC ACID (HBSA)

In order to further test the explanation offered by Yin *et al.* [3] and expand on their work, we choose to study two new aqueous solutions: benzenesulfonic acid (HBSA) and (b) sodium benzenesulfonate (NaBSA).

Figure 3.3 shows molecular structures of HBSA and NaBSA. As mentioned in the previous section, according to DFT calculations of Yin *et al.* and several other groups, ions in the droplet are attracted to graphene. However, Yang *et al.* [18] demonstrated

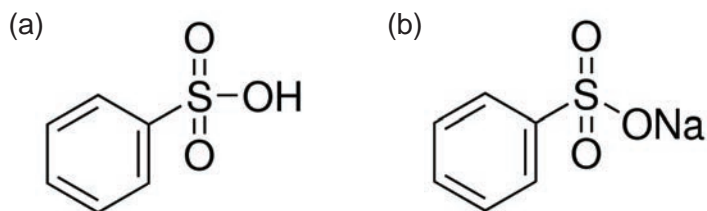


Figure 3.3: **Chemical structures of two molecules studied in this chapter.** (a) Benzenesulfonic acid (HBSA). (b) Sodium benzenesulfonate (NaBSA). BSA denotes the mutual part of the two molecules.

that ions from the droplet adhere to graphene due to strong interaction with dipoles on the underlying PET substrate. We therefore expect the ionic parts of NaBSA and HBSA ( $\text{Na}^+$  and  $\text{H}^+$ , respectively) to strongly adhere to PET substrate. The phenyl group that is part of NaBSA and HBSA is non-polar and it would not have this interaction with the PET substrate. However, it should have a  $\pi - \pi$  stacking interaction with the graphene. We suggest that these two effects will combine to give a very strong interaction with the graphene/PET interface.

In this chapter we report on the voltage signal induced by drawing a droplet of NaCl along graphene on a PET substrate and confirm that the amplitude of the voltage depends on the length, volume, concentration, velocity of the droplet and direction of its motion, in agreement with the work reported in [3]. We further utilize NaBSA and HBSA aqueous solutions to induce voltage signals in graphene and show that adhesion of  $\text{BSA}^-$  ions to graphene/PET interface is so strong that the ions leave the droplet and form a firmly adsorbed negatively charged layer on the graphene surface. We demonstrate that even deionized water can give a signal if moved along this charged graphene sheet and suggest that this is due to the high polarizability of the water. In the second part of the chapter we focus on the reverse effect of the induced voltage: we attempt to set the droplet into motion by applying a voltage across the graphene sheet.

## 3.2. EXPERIMENTAL DETAILS

For the controlled sliding of a droplet over the surface of graphene we have built a transfer stage (Figure 3.4). The graphene, grown by chemical vapor deposition and transferred onto a polyethylene terephthalate (PET) wafer, is purchased from Graphenea®. The wafer is cut into strips of  $\sim 0.7$  cm width and 7–9 cm length. The strip is fixed to the stage with a glue and graphene is contacted electrically by a drop of silver paint embedding a copper wire. The resistance of the graphene strip is between 7 and 14 k $\Omega$  (or a sheet resistance of around 0.7–1.1 k $\Omega/\square$ ). The schematics of the experimental set-up is shown in Figure 3.5. The volume of a droplet is measured with a pipette with an accuracy of  $\pm 0.5 \mu\text{l}$ . The droplet is placed on the graphene strip and subsequently pressed from the top by a  $5 \times 5 \text{ mm}^2$  Si/SiO<sub>2</sub> wafer, which is positioned at a height of 1.2–1.7 mm. The distance between the graphene and the wafer can be adjusted with the help of a micrometer screw. The smallest droplet we used at the highest wafer-graphene distance still touches the edges of the PET strip. When the volume of the droplet is increased or when the wafer is pressed further down, the edges of the PET substrate will confine the droplet on the strip due to the surface tension.

The wafer is attached to a variable-speed stepper motor (commercially available Pandrive® PN1141) and is moved along the graphene strip at a constant height and

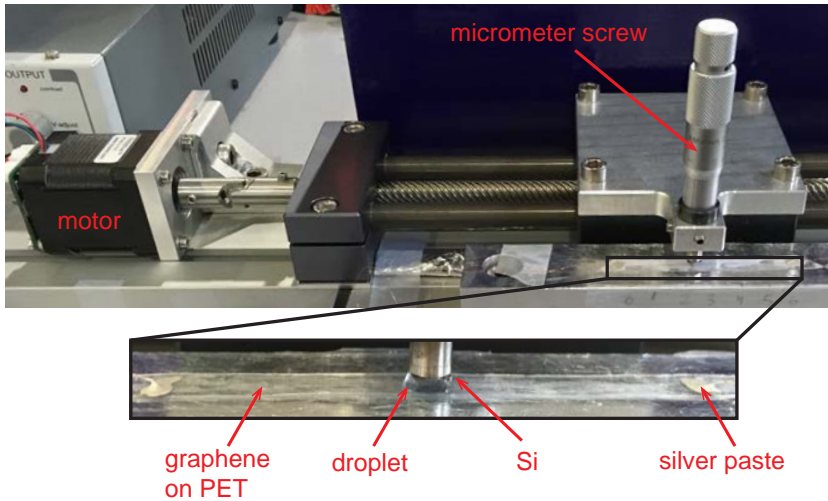


Figure 3.4: **Transfer stage with a sample holder.** The distance between the graphene strip on PET and the wafer can be adjusted with the help of a micrometer screw. The platform with the micrometer screw moves along the sample stage driven by a stepper motor, controlled via the software.

constant speed. The velocity and direction of movement on the wafer are controlled with the software. As the wafer moves, it drags the droplet due to surface tension. The

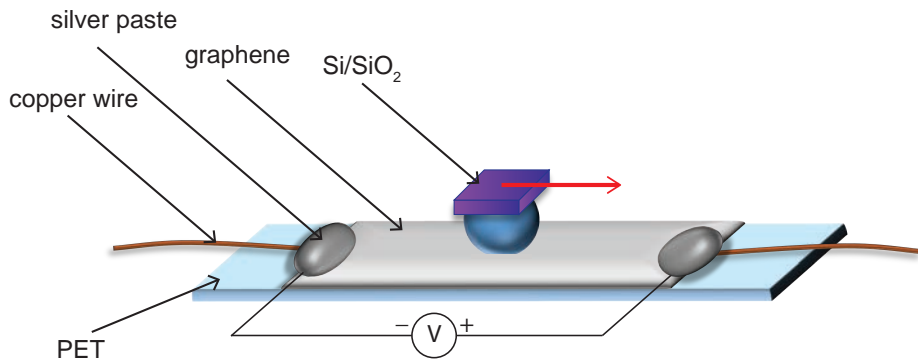


Figure 3.5: **Schematics of the experimental setup.** A droplet on a graphene strip on PET is pressed with a Si/SiO<sub>2</sub> wafer attached to a stepper motor. The droplet sticks to the wafer and follows its motion due to surface tension. Motion of the droplet (indicated with the red arrow) induces a voltage drop across the graphene strip.

induced voltage signal across the graphene is recorded by a Keithley® multimeter, which has its positive terminal connected to the right end of the graphene strip. The error of the Keithley multimeter is  $\pm 0.01$  mV. Velocities directed towards the right end are indicated as positive. Velocities are calibrated with a timer and estimated accuracy from repeated calibrations is around  $\pm 0.5$  cm/s. A fresh graphene strip is placed on the stage before the start of each experiment when changing to a different concentration or a different type of ions.

### 3.3. RESULTS

#### 3.3.1. SODIUM CHLORIDE (NaCl)

Initial experiments were performed with aqueous solutions of NaCl. Figure 3.6 shows voltage signals induced across the graphene strip for a droplet of NaCl solution. The volume of the droplet is  $43 \mu\text{L}$ , the concentration is  $0.01$  M and the graphene-wafer distance is  $h = 1.2$  mm, unless indicated otherwise. This volume and distance are such that the droplet extends a little outside the size of the Si/SiO wafer, but stays within the sides of the graphene sheet, which is a few millimeters wider than the wafer. Error bars are calculated as standard deviation:

$$s = \sqrt{\frac{\sum_{i=1}^N (V_i - \bar{V})^2}{N - 1}} \quad (3.1)$$

where  $N$  is the number of measured values  $V_i$  and  $\bar{V}$  is the mean value of a data point.

Figure 3.6(a) shows a linear increase of the induced voltage with increasing velocity of the droplet. Positive velocity indicates motion from left to right and negative velocity indicates motion in the opposite direction. When the droplet moves from right to left, we observe the same magnitude of the induced voltage but with reversed sign. When we move two droplets on a graphene strip in opposite directions, we observe no voltage response as the voltages generated by each individual droplet offset each other, which is to be expected.

The induced voltage as a function of velocity for different volumes of the droplet of NaCl solution is shown in Figure 3.6(b). Blue points represent measured data for a droplet of  $43 \mu\text{L}$  volume and red points are data for a droplet of  $65 \mu\text{L}$  volume. We observe higher induced voltage for the droplet of a larger volume, for the same velocity. As can be seen, the induced voltage is not a linear function of the volume of the droplet: when the volume of the droplet is increased by a factor of 1.5, the induced voltage is increased by a smaller factor ( $\sim 1.3$ ). The reason is that the length of the droplet, which is the factor that determines the amplitude of the induced voltage [3], does not increase linearly with the volume of the droplet.

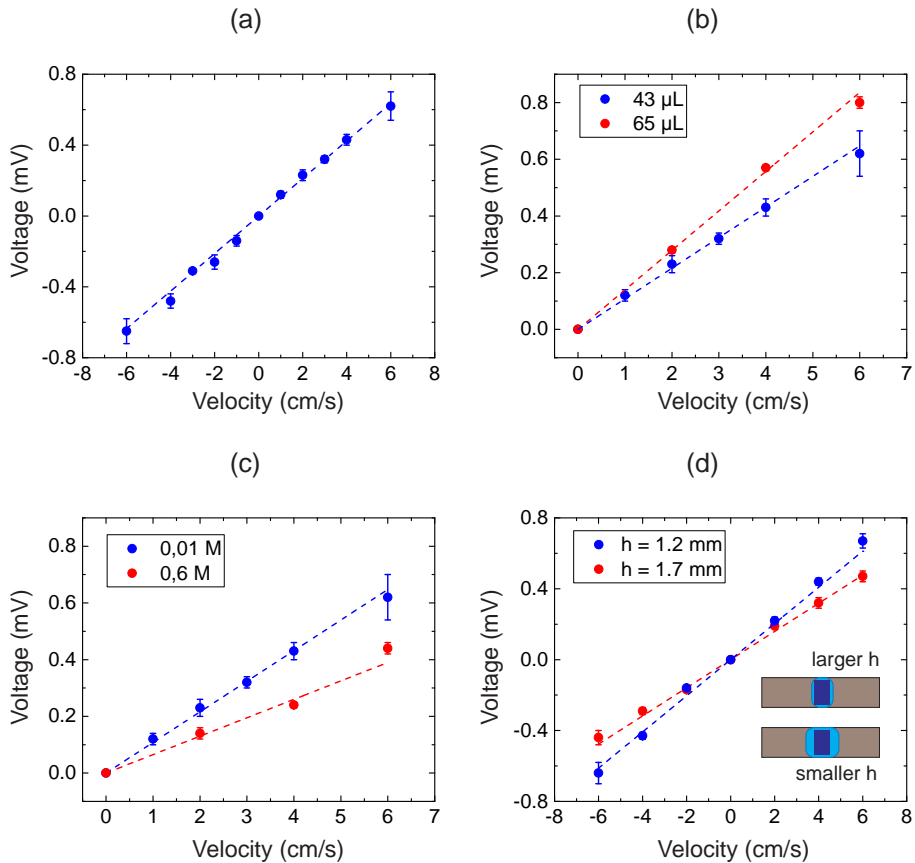


Figure 3.6: **Voltage induced across a graphene layer by moving a droplet of NaCl solution along the graphene surface.** Volume and concentration of the solution are 43  $\mu\text{L}$  and 0.01 M, unless indicated otherwise. (a) Typical voltage signal produced by moving a droplet along a graphene strip in one direction (positive values) and in the opposite direction (negative values). The dashed line is a linear fit to the measured data. (b) Voltage signal for droplets of two different volumes: 43  $\mu\text{L}$  (blue data points) and 65  $\mu\text{L}$  (red data points). The dashed lines are linear fits to the measured data. (c) Voltage response to the motion of droplets with different concentrations of NaCl solution: 0.01 M (blue data points) and 0.6 M (red data points). (d) The induced voltage signal for two different graphene-wafer distances:  $h = 1.2$  mm (blue data points) and  $h = 1.7$  mm (red data points). Inset (top view): schematics of the wafer (dark blue square) pressing on the droplet (light blue) which lies on graphene surface (grey rectangle) for two different graphene-wafer distances.

Figure 3.6(c) shows the induced voltage signal as a function of velocity for 0.01 M (blue data points) and 0.6 M (red data points) NaCl concentrations. We observe a higher voltage signal for lower NaCl concentration. The reason, as proposed by Yin *et al.* [3], is that the effective screening of the electric field from  $\text{Na}^+$  charges, produced

by the presence of  $\text{Cl}^-$  anions in the electric double layer is enhanced with increase of electrolyte concentration, as the Debye screening length decreases with the square root of ion concentration.

Figure 3.6(d) shows the induced voltage signal for NaCl droplets as a function of velocity for two different graphene-wafer distances:  $h = 1.2$  mm (blue data points) and  $h = 1.7$  mm (red data points). The voltage signal is higher for the smaller  $h$ . The reason is the larger droplet-graphene contact area for the smaller  $h$ . Our graphene strips on PET are narrow and fully cover the PET substrate. The smallest droplet we used at the highest wafer-graphene distance touches the edges of the PET strip. When the volume of the droplet is increased or when the wafer is pressed further down, the edges of the PET substrate will confine the droplet on the strip due to the surface tension. Therefore the width of the droplet on the graphene remains the same and length of the droplet increases (inset of Figure 3.6(d)).

After the experiment with NaCl droplets, no voltage signal was recorded on the same graphene layer when moving a  $\sim 43$   $\mu\text{L}$  droplet of ultrapure double-deionized Mili-Q® water (hereafter referred to as *deionized* water) at maximum speed (6 cm/s) and at graphene-wafer distance of  $h = 1.2$  mm. The resistivity of the deionized water is  $\rho = 18.2$   $\text{M}\Omega\text{cm}$ .

Yin *et al.* [3] propose a model with linear dependence of the induced voltage on the droplet's velocity and length, as well as a non-linear dependence with volume of the droplet (related to non-linear increase of the droplet's contact length with volume):

$$V = R_d I = -R_{\square} L \psi C_0 v = Av \quad (3.2)$$

where  $R_d$  is resistance across the graphene under the droplet,  $R_{\square}$  is the square resistance of the graphene,  $L$  is the length of the droplet,  $\psi$  is the equivalent surface potential of graphene relative to the adsorbed hydrated  $\text{Na}^+$  layer,  $C_0$  is the pseudo-capacitance per unit area, and  $v$  is the droplet's velocity.

Values of the voltage signal that we obtained for 0.06 M NaCl are the same as the values reported by Yin *et al.*, while the signal for 0.01 M NaCl is around 1.3 times smaller. If we take into account that our parameters ( $R_{\text{sq}}$ ,  $W$ ,  $L$  and  $h$ ) are different from parameters in the experiment of Yin *et al.*, then according to the proposed formula for the induced voltage (equation 3.2) we should expect almost 2 times smaller voltage in our experiment. This discrepancy is possibly related to the details of the experimental arrangements.

### 3.3.2. SODIUM BENZENESULFONATE (NABSA) AND BENZENESULFONIC ACID (HBSA)

The second set of measurements was performed with an aqueous solution of sodium benzenesulfonate salt (NaBSA). Figure 3.7(a) shows a comparison between voltage

responses from NaCl (blue data points) and NaBSA (brown data points) for a concentration of 0.6 M. The induced voltage signal for NaBSA is larger than for NaCl and the sign of the induced voltage is the same for both solutions.

Surprisingly, after removing a droplet of NaBSA and flushing the graphene with deionized water, there was still a voltage signal over graphene when moving a droplet of deionized water along it. Voltage signals for a  $\sim 43 \mu\text{L}$  droplet of deionized water at maximum speed (6 cm/s) and graphene-wafer distance of  $h = 1.2 \text{ mm}$  after different cleaning times were:

- $t = 20 \text{ min}$  ,  $V = 0.27 \text{ mV}$
- $t = 30 \text{ min}$  ,  $V = 0.04 \text{ mV}$
- $t = 40 \text{ min}$  ,  $V = 0 \text{ mV}$

All voltages are of the same sign as the voltages induced with NaBSA. After flushing of the graphene with deionized water for 40 min, there was no detectable signal with deionized water any longer.

A third set of measurements is performed with HBSA droplets. Figure 3.7(b) shows induced voltage signals from NaCl (blue data points) and HBSA (red data points) droplets for a concentration of 0.01 M. Here the signs of the induced voltages are also the same for both solutions, whereas the induced voltage is higher for NaCl. Just like in the case of NaBSA, graphene was not clean after removing a droplet of HBSA and

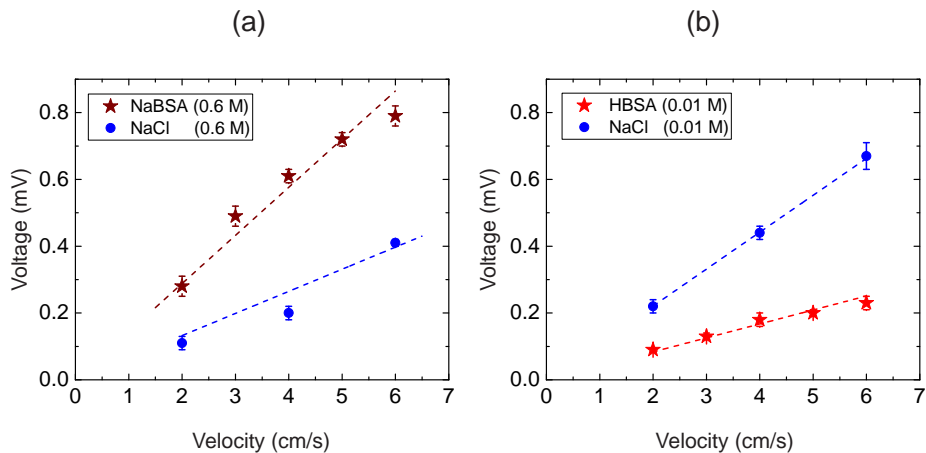


Figure 3.7: **Results for NaBSA and HBSA droplets.** (a) Voltage signal produced by drawing a droplet of 0.6 M NaCl solution (blue data points) compared to a droplet of 0.6 M NaBSA solution (brown data points). (b) Voltage induced by moving a droplet of 0.01 M NaCl solution (blue data points) compared to a droplet of 0.01 M HBSA solution (red data points). The graphene-wafer distance is  $h = 1.2 \text{ mm}$  and the volume of all the droplets is  $43 \mu\text{L}$  for both data sets.

there was a measurable voltage signal when moving a  $\sim 43 \mu\text{L}$  droplet of deionized water at the maximum speed (6 cm/s) and graphene-wafer distance of  $h = 1.2 \text{ mm}$ . After 20 min of flushing the graphene with deionized water, voltage signals were no longer detected.

## 3.4. DISCUSSION

### 3.4.1. NABSA

As noted above, after the experiment with NaCl droplets on graphene we observed no voltage signal across the graphene when moving a droplet of deionized water. This implies that  $\text{Na}^+$  and  $\text{Cl}^-$  ions do not adsorb to the graphene and leave the droplet.

Remarkably, in the case of NaBSA we do measure a strong voltage signal with a deionized water droplet after NaBSA droplets are removed from graphene (this will be discussed in detail in subsection 3.4.3). Since we know that  $\text{Na}^+$  ions do not leave the droplet, we conclude it is the  $\text{BSA}^-$  anions that remain adsorbed to the graphene and stay on it after the droplet is removed. In addition, the NaBSA droplets induce a voltage signal of the same sign as NaCl droplets, which means that positive ions are the ones dominating the pseudocapacitance in NaBSA, in other words  $\text{Na}^+$ . The  $\text{Na}^+$  ions are attracted by the  $\text{BSA}^-$  layer and in turn they attract the electrons in the graphene with which they form a pseudocapacitor. This mechanism is similar to the one of HCl solution reported by Yin *et al.*, where  $\text{H}_3\text{O}^+$  ions adsorb to the graphene and leave the droplet, while the  $\text{Cl}^-$  ions are the mobile charges, which contribute to the pseudocapacitor.

Both NaBSA and NaCl solutions have the same concentration, thus the same  $\lambda_D$ , yet they induce different voltage signals as seen in Figure 3.7(a). We suggest that this is due to different mechanisms involved in these two cases (Figure 3.8). For NaBSA droplets,  $\text{BSA}^-$  ions adsorb to the surface and  $\text{Na}^+$  are the only mobile ions (Figure 3.8(b)). On the other hand, in NaCl both  $\text{Na}^+$  and  $\text{Cl}^-$  are mobile species (Figure 3.8(a)). Even though the  $\text{Na}^+$  layer is close to the graphene and contributes more to the pseudocapacitor, there is also the influence of the layer of  $\text{Cl}^-$  above which reduces the effective charge. This would result in a smaller voltage signal compared to the case with a single type of mobile charges.

In order to induce the voltage signal, the layer of  $\text{Na}^+$  in NaBSA has to be close to the BSA layer, within the Debye screening length distance ( $\lambda_D$ ). For a monovalent salt  $\lambda_D$  is given as:

$$\lambda_D = \frac{1}{e} \sqrt{\frac{\epsilon_0 \epsilon_r k_b T}{2c}}. \quad (3.3)$$

where  $c$  is the concentration,  $\epsilon_0$  is the permittivity of free space,  $\epsilon_r$  is the dielectric

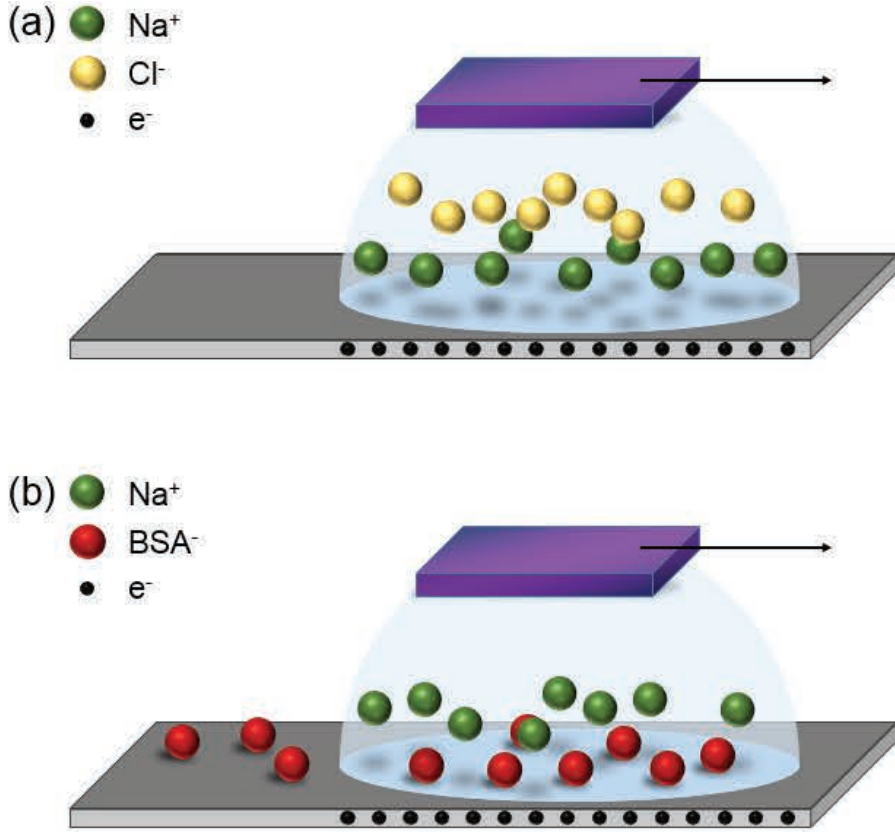


Figure 3.8: **Schematics of ionic distribution.** (a) NaCl and (b) sodium benzenesulfonate (NaBSA) droplets on graphene on PET dragged along by a Si/SiO<sub>2</sub> wafer (purple plate). In the case of NaCl both types of charges (Na<sup>+</sup> and Cl<sup>-</sup>) remain within the droplet, whereas in the case of NaBSA, BSA<sup>-</sup> ions (red) leave the droplet and remain adsorbed to graphene.

constant (10-100),  $T$  is the temperature and  $k_b$  is the Boltzmann constant. For the concentration of  $c = 0.6$  M we obtain the value of  $\lambda_D \sim 0.4$  nm. This value is small enough to induce a large signal in graphene from Na<sup>+</sup> ions sitting right above the BSA<sup>-</sup> layer.

### 3.4.2. HBSA

We concluded that the affinity of BSA<sup>-</sup> ions for graphene is larger than the affinity of Na<sup>+</sup> ions. We also know from the experiment of Yin *et al.* [3] with HCl that H<sub>3</sub>O<sup>+</sup> ions remain strongly adsorbed to graphene. The question arises as to which ions have larger affinity to graphene: H<sub>3</sub>O<sup>+</sup> or BSA<sup>-</sup>.

The data from the experiment with HBSA can give us the answer. The sign of

the induced voltage with HBSA droplet is the same as for NaCl (Figure 3.7(b)), which means that it has to be the positive  $\text{H}_3\text{O}^+$  ions that dominate the pseudocapacitor. We conclude that both species could adsorb to graphene and leave the droplet, with more  $\text{H}_3\text{O}^+$  mobile ions staying within the droplet and  $\text{BSA}^-$  having higher affinity to graphene.

Just like with the NaBSA droplets, we also record a signal with a droplet of deionized water after the graphene surface has been in contact with a droplet of HBSA. As mentioned above, the graphene cleaning time is two times longer for NaBSA than for HBSA. In the case of HBSA, we have both types of charges,  $\text{H}_3\text{O}^+$  and  $\text{BSA}^-$ , leaving the droplet (Figure 3.9(b)) and we speculate that they can be removed easier from graphene by flushing with water because they partially screen each others effects.

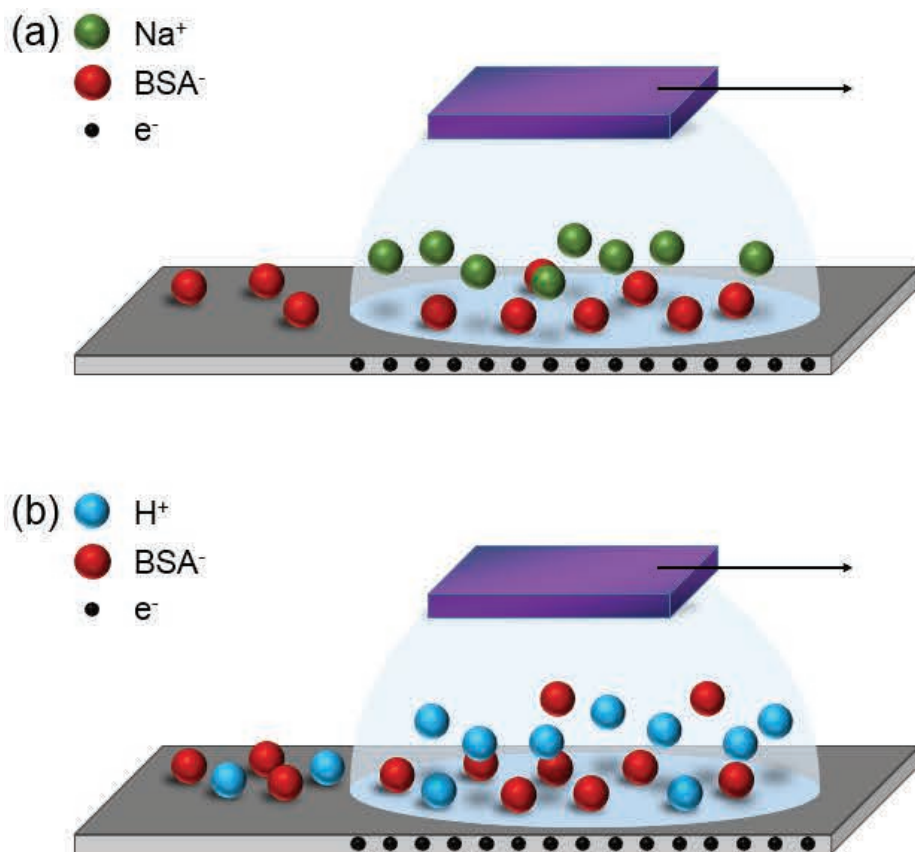


Figure 3.9: **Schematics of ionic distribution.** (a) Sodium benzenesulfonate (NaBSA) and (b) benzenesulfonic acid (HBSA) droplets on graphene on PET dragged along by a Si/SiO<sub>2</sub> wafer (purple plate). In the case of NaBSA only BSA<sup>-</sup> leaves the droplet, whereas for HBSA both types of charges (BSA<sup>-</sup> (red) and H<sub>3</sub>O<sup>+</sup> (blue)) leave the droplet and remain adsorbed to graphene.

There is effectively a smaller amount of charge that will bond to the graphene or the dipoles of the underlying PET substrate. In case of NaBSA, only  $\text{BSA}^-$  ions leave the droplet, which means the effective charge is higher than for HBSA and thus harder to remove.

This idea could also explain the larger induced signal with the NaBSA droplet compared to the HBSA droplet. In the NaBSA droplet only the  $\text{BSA}^-$  ions adhere to the surface of graphene; they attract  $\text{Na}^+$  ions, which in turn attract electrons in graphene. In the HBSA droplet both  $\text{H}_3\text{O}^+$  and  $\text{BSA}^-$  adhere to the surface ( $\text{H}_3\text{O}^+$  will remain more mobile in the droplet), which means that the effective charge of the  $\text{BSA}^-$  is lowered. This means that there will be less positive charges from the droplet attracted to graphene, and in turn less negative charges induced in the graphene.

### 3.4.3. SIGNAL WITH DEIONIZED WATER

The most extraordinary observation in our experiments is the fact a droplet of deionized water can induce a voltage drop in the graphene after previously using NaBSA or HBSA droplets. In the case of NaBSA, even after 20 min of flushing the graphene with deionized water, the voltage signal with a droplet of deionized water was still very strong, only three times smaller than the maximum signal achieved with a NaBSA droplet. In order to understand the underlying physics behind it, we consider several possible mechanisms.

#### INTRINSIC CHARGES IN DEIONIZED WATER

No matter how pure deionized water is, it will always contain a small amount of  $\text{H}^+$  and  $\text{OH}^-$  charges. Particularly, the conductivity of the deionized water at a room temperature is  $5.5 \cdot 10^{-6}$  S/m (equivalent to a resistivity of 18.2 M $\Omega$ cm). Could these charges be enough to induce a voltage signal in graphene?

As mentioned previously, there was no induced voltage with a droplet of deionized water onto freshly exposed graphene. In order to rationalize this observation, we calculate the Debye screening length of deionized water ( $\lambda_D$ ), which is equivalent to the distance between the two planes of a pseudocapacitor (layer of charges in the droplet and electrons in graphene). According to the proposed theory of Yin *et al.*, the distance between these layers has to be very small (up to several nanometers) in order to induce measurable voltage signal ( $C \propto 1/\lambda_D$ ). For large distances between the two layers, the induced voltage would be too small to be detected. We estimate  $\lambda_D$  of the deionized water to be around 0.14  $\mu\text{m}$ . This means that the pseudocapacitance, and in turn the induced voltage signal, would be around 400 times smaller. In our experiment the highest voltage measured with a NaCl droplet is around 0.6 mV, therefore the induced voltage signal from deionized water should be around 0.001 mV. The smallest voltage our Keithley is able to record is 0.02 mV. This explains why no voltage signal was detected with a droplet of deionized water on fresh graphene and confirms that the concentration of charges in the deionized water is not high enough

to induce measurable voltage signal.

#### RESIDUAL IONS ON GRAPHENE FROM IONIC LIQUIDS

We have already shown that the concentration of intrinsic charges in deionized water is too small to induce a measurable voltage signal in the graphene. However, there are residual charges on the graphene from HBSA/NaBSA liquids. If we assume full initial surface coverage with ions and if we assume that all the residual charges on the graphene under the deionized droplet will detach from the graphene into the droplet, then the estimated concentration of these charges in the droplet of deionized water is  $c = 10^{-6}$  M. Extrapolating the measured signals for known concentrations of the droplets to this small concentration the signal would be below our noise limit.

We therefore conclude that even in the unlikely case that all residual ions diffuse back to the surface of graphene, concentration of ions would not be sufficient to induce a measurable voltage signal.

#### POLARIZABILITY OF WATER

Figure 3.10(a) shows a schematics of a droplet of NaBSA solution (indicated with green color) after moving it along the graphene sheet (grey). Negative  $\text{BSA}^-$  ions (minus signs) adsorb to the surface of graphene and attract positive  $\text{Na}^+$  ions from the droplet (marked as plus signs in the droplet).  $\text{Na}^+$  ions cause release of positive charges in graphene under the area of the droplet. When the NaBSA droplet is removed (Figure 3.10(b)) negative  $\text{BSA}^-$  ions remain adsorbed to the graphene, attracting positive charges from graphene towards the surface. What will happen when a droplet of deionized water is now deposited on the graphene covered with a layer of charges?

A water molecule is made up of one oxygen and two hydrogen atoms. It is a polar molecule with partial negative charge near the oxygen atom, due to the unshared pair of electrons, and partial positive charges near the hydrogen atoms (Figure 3.10(c)). When a droplet of deionized water is deposited on graphene (Figure 3.10(d)) water molecules will rearrange so that the positive  $\text{H}^+$  ends (small blue balls) are facing the graphene and screening the  $\text{BSA}^-$  ions, which leads to releasing of positive charges from graphene in the area below the droplet (which is effectively attracting negative charges). When the droplet is set in motion, negative charges from graphene will follow the droplet, just like in the case with NaBSA. The sign with the deionized droplet will therefore be the same as for the ionic liquid, which is exactly what we measured. The total effective charge produced by the polarization on water can be calculated as

$$Q_p = \frac{\epsilon_r}{\epsilon_r + 1} Q_{ext} \quad (3.4)$$

where  $\epsilon_r = 80$  is dielectric constant of water. From here we see that the induced charge in a droplet is nearly equal to the external charge adsorbed to graphene.

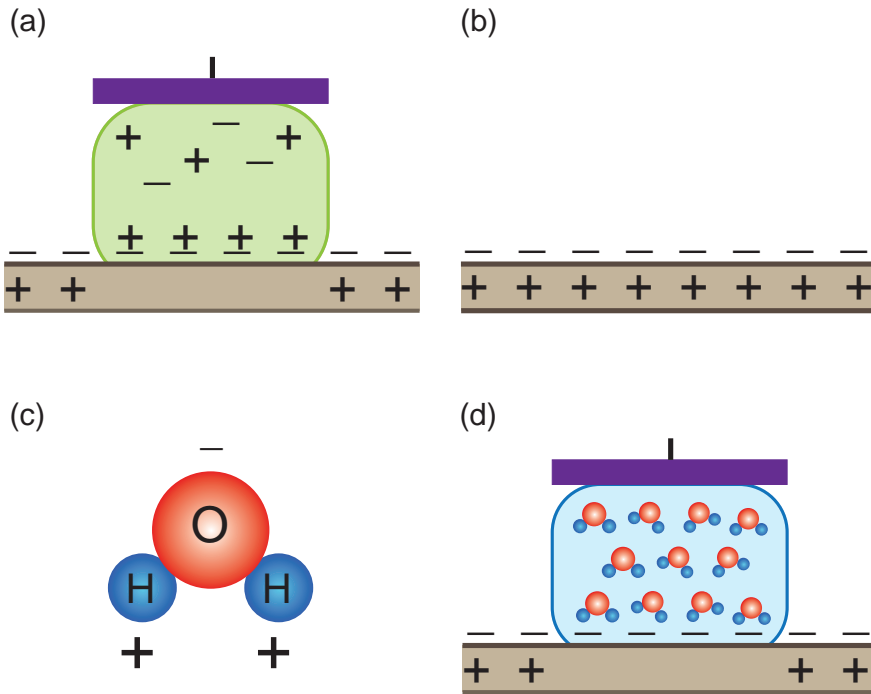


Figure 3.10: **Polarizability of water.** (a) Distribution of charges for NaBSA droplet (indicated with green color) moved along the graphene (grey rectangle) while being pressed from top with Si/SiO<sub>2</sub> wafer (purple rectangle). Minus signs on the graphene surface indicate adsorbed BSA<sup>-</sup> ions which left the droplet. Plus signs in the droplet indicate Na<sup>+</sup> ions. (b) Graphene surface after the removal of the NaBSA droplet. Graphene remains covered with a negative layer of BSA<sup>-</sup> ions, which attract positive charges from graphene towards the interface. (c) Schematics of a polar water molecule. (d) Distribution of charges when a droplet of deionized water (blue) is deposited on the charged graphene surface from panel (b). Polar molecules of water will arrange such that positive H ends (blue balls) will face the negatively charged graphene sheet, and negative O ends will face the wafer. Due to positive H charges from the water screening the BSA<sup>-</sup> ions, positive charges in the graphene will be released under the droplet area.

This is an important observation because it implies that polarizability of water has a large effect, not only in the droplet of deionized water, but also in aqueous solutions of other ionic liquids. As mentioned before, the voltage signal with deionized water is of the same order of magnitude as the signal from the ionic liquid even after 20 min of cleaning the graphene with deionized water. We conclude that the polarizability of the water is mainly responsible for the induced voltage on a charged graphene sheet and the ions in the ionic liquid droplet only partially contribute to the voltage signal. As long as there are ions that have a strong tendency to adsorb to

graphene (or an underlying substrate) there is no requirement for ions in the droplet. Water alone will induce a voltage signal!

### 3.5. ELECTROMIGRATION FORCES ON A NaCl DROPLET

As we have shown above, a voltage is induced when moving a droplet of ionic solution along a strip of graphene. Would the opposite be possible: to apply a voltage across the graphene strip and induce motion of the droplet?

In Chapter 2 we discuss the theory of the wind force and the direct force. The wind force stems from the transfer of momentum of electrons impinging on the ions, whereas the direct force is the electrostatic force which comes from the external electric field. A NaCl droplet attracts negative charges in graphene, which together with  $\text{Na}^+$  ions form a strong pseudocapacitor, therefore we expect that an induced motion of negative charges in graphene in an external electric field will be accompanied by motion of the droplet. In order to test this idea, we apply voltage across a graphene sheet and look for eventual motion of the droplet.

#### 3.5.1. EXPERIMENTAL SETUP AND RESULTS

We use the same stage and the same substrate as for the experiment of detecting voltages induced by motion of droplets of ionic solutions (see section 3.2). We first observe that droplets stick to the surface of graphene and a sticking force hampers lateral motion of the droplets. This sticking force increases the longer the droplet stays on the graphene. For this reason we first apply a voltage of  $\pm 10$  V across the graphene strip of  $8\text{ k}\Omega$  resistance and then deposit a  $43\ \mu\text{L}$  droplet of  $0.01\text{ M}$  NaCl on graphene while the current is flowing. We observe no motion of the droplet. Increasing the voltage up to  $100\text{ V}$  resulted in a large increase of graphene resistance, eventually leading to infinite resistance due to burning away the graphene.

The adhesion of the droplet to the graphene/PET substrate is so high that after the droplet was resting on graphene/PET for only  $\sim 5$  sec, we were not able to move it even when placing the sample vertically or upside down. In order to overcome strong adhesion to the graphene/PET substrate, we tilt the stage to a critical angle at which gravitational and adhesion forces are almost at the balance. For angles larger than this critical angle droplets after deposition to the substrate slide down the slope; below the critical angle they remain in place. Figure 3.11 shows a schematic of the tilted stage with graphene (grey rectangle) with a droplet (blue ball) on top. This critical angle is  $\alpha_c = 60^\circ$  for a droplet of  $43\ \mu\text{L}$  volume. If the stage is tilted by one more degree, the droplet starts sliding due to gravitational force overcoming friction.

Further, a voltage of  $10\text{ V}$  is applied across the graphene strip with  $8\text{ k}\Omega$  resistance, before a  $43\ \mu\text{L}$  droplet of  $0.01\text{ M}$  NaCl-solution is deposited on it with a pipette. A small force would lead to a shift in the critical angle, depending on the sign of the

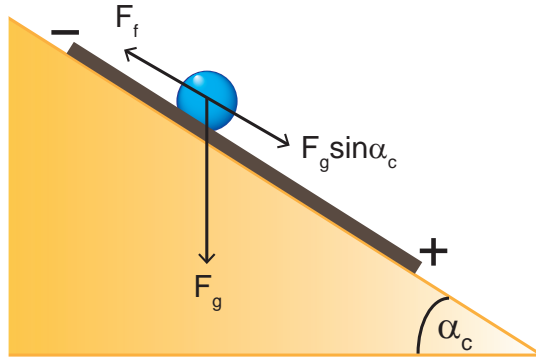


Figure 3.11: **Schematics of the experimental setup.** A  $43 \mu\text{L}$  droplet of  $0.01 \text{ M}$  NaCl solution is positioned on graphene on PET (grey rectangle) lying on a stage tilted by a critical angle of  $\alpha_c = 60^\circ$  at which friction force  $F_f$  and horizontal component of the gravitational force  $F_g \sin \alpha_c$  are in balance. A voltage of  $10 \text{ V}$  is applied across the graphene strip before the droplet is deposited.

applied voltage. However, we were unable to resolve any change in critical tilt angle within our accuracy of about  $1^\circ$ .

### 3.5.2. DISCUSSION

When the tilt angle is increased from the critical angle by  $1^\circ$  the droplet starts to slide due to gravity. The amplitude of the effective gravitational force component that sets the droplet in motion for a small increase of the angle  $\Delta\alpha$  is given by

$$\begin{aligned}
 F_{\text{eff}} &= F_g \sin(\alpha_c + \Delta\alpha) - F_f \\
 &= F_g \sin(\alpha_c + \Delta\alpha) - F_g \sin \alpha_c \\
 &\approx \rho V g \Delta\alpha \cos \alpha_c
 \end{aligned} \tag{3.5}$$

where we expanded the function  $\sin(\alpha_c + \Delta\alpha)$  into the first two terms of Taylor series around the point  $\alpha_c$ . For a droplet of  $43 \mu\text{L}$  volume, critical angle of  $\alpha_c = 60^\circ$  and  $\Delta\alpha = 1^\circ$  (equivalent to  $0.017$  radians) we obtain the effective force of  $F_{\text{eff}} = 3.6 \cdot 10^{-6} \text{ N}$ .

We now consider the direct force resulting from the electric field acting on the induced charges in graphene when a voltage is applied across graphene strip. Total electron charge,  $Q$ , is calculated as

$$Q = \psi C_0 W L \tag{3.6}$$

where  $\psi$  is the equivalent surface potential of graphene relative to the adsorbed hydrated  $\text{Na}^+$  layer,  $C_0$  is pseudocapacitance per unit area, and  $L$  and  $W$  are the length and the width of the droplet, respectively. A current across the graphene section under the droplet is derived from the rate of transferred electrons as

$$I = -\frac{dQ}{dt} = -\psi C_0 W v \quad (3.7)$$

where  $v$  is the velocity of the droplet. From here the induced voltage across the graphene under the droplet is given as

$$V = R_d I = -R_{\square} L \psi C_0 v = A v \quad (3.8)$$

where  $R_d$  is resistance across the graphene under the droplet and  $R_{\square}$  is the square resistance of the graphene. Coefficient  $A$  can be taken from the experimental data for any set of measured voltage  $V$  as a function of the droplet velocity  $v$  and it has the value of around  $1.1 \cdot 10^{-2}$  Vs/m. The electric field is given as

$$E = \frac{V}{L} = \frac{I R_d}{L} = \frac{I R_{\square}}{W} \quad (B.8)$$

From here we obtain a value for  $F_d$  for the applied voltage of 10 V across graphene strip:

$$F_d = QE = IA = 1.4 \cdot 10^{-5} \text{ N}. \quad (B.9)$$

This means that the direct force acting on the charges in the graphene is larger than our resolution for changes in the effective gravitational force, yet we do not observe any motion of the droplet. In considering the direct force we only took into account one layer of charges in the droplet. If we also consider the charges of the opposite sign in the droplet which will experience nearly the same electric field, the two charge layers should nearly cancel. With this assumption, the droplet will not move along the graphene as the electric field will not move a neutral body.

Interestingly, even though we cannot observe the effects of the wind force, we can estimate its magnitude by measuring the power injected into the system. Here we assume that the wind force is the same as the component  $F_e$  of the force during mechanical dragging of the droplet that is converted into electrical energy, and that this force is conservative. The power that this force exerts is  $P = v F_e$ , and this is converted in electrical power  $P = VI = I^2 R$ . We measure the current that graphene generates by adding a resistor  $R_t$  of a known resistance, Figure 3.12 ( $R_t = 12.96 \text{ k}\Omega$ ). The resistance of the graphene strip is  $R_g = 4.96 \text{ k}\Omega$ . The measured voltage signal across the resistor  $R_t$ , when drawing a droplet with a speed of 6 cm/s is  $V_t = 0.15 \text{ mV}$ . Plugging in the numbers gives an estimate for the drag force  $F_e$ , which we take as a measure of the wind force, of  $F_w = 40 \text{ pN}$ . This is well below our current measurement limit of about  $4 \mu\text{N}$ .

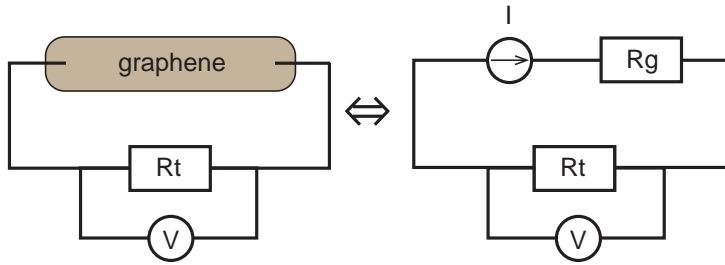


Figure 3.12: **Schematics of the circuit for measuring current induced by drawing a droplet along graphene.**  $R_g = 4.96 \text{ k}\Omega$ ,  $R_t = 12.96 \text{ k}\Omega$ .

### 3.6. CONCLUSION AND OUTLOOK

We measured the voltage response for a droplet of NaCl aqueous solution and demonstrated the influence of volume, concentration, length, velocity and direction of motion on the magnitude and sign of the induced voltage. We studied the induced voltage signal for solutions of NaBSA and HBSA droplets and proposed that there is a strong adhesion of BSA<sup>-</sup> ions to graphene. This leads to the remarkable discovery of a voltage induced by dragging a droplet of deionized water along a negatively charged graphene sheet, resulting from the wetting by NaBSA or HBSA solutions. The observed effect is explained by the polarizability of water, which has a large influence on the magnitude of the induced voltage, so much that the presence of ions in the liquid is not required. The effects could be further tested by using other liquids, such as HCl. Positive hydronium ions from HCl droplet bond strongly to graphene/PET, which would also give a suitable environment for possible voltage induction with deionized water, this time on a positively charged sheet. Further investigation are also needed to use graphene on PMMA or other substrates, in order to investigate different ion-substrate adsorption properties and consequential differences in induced voltage signals.

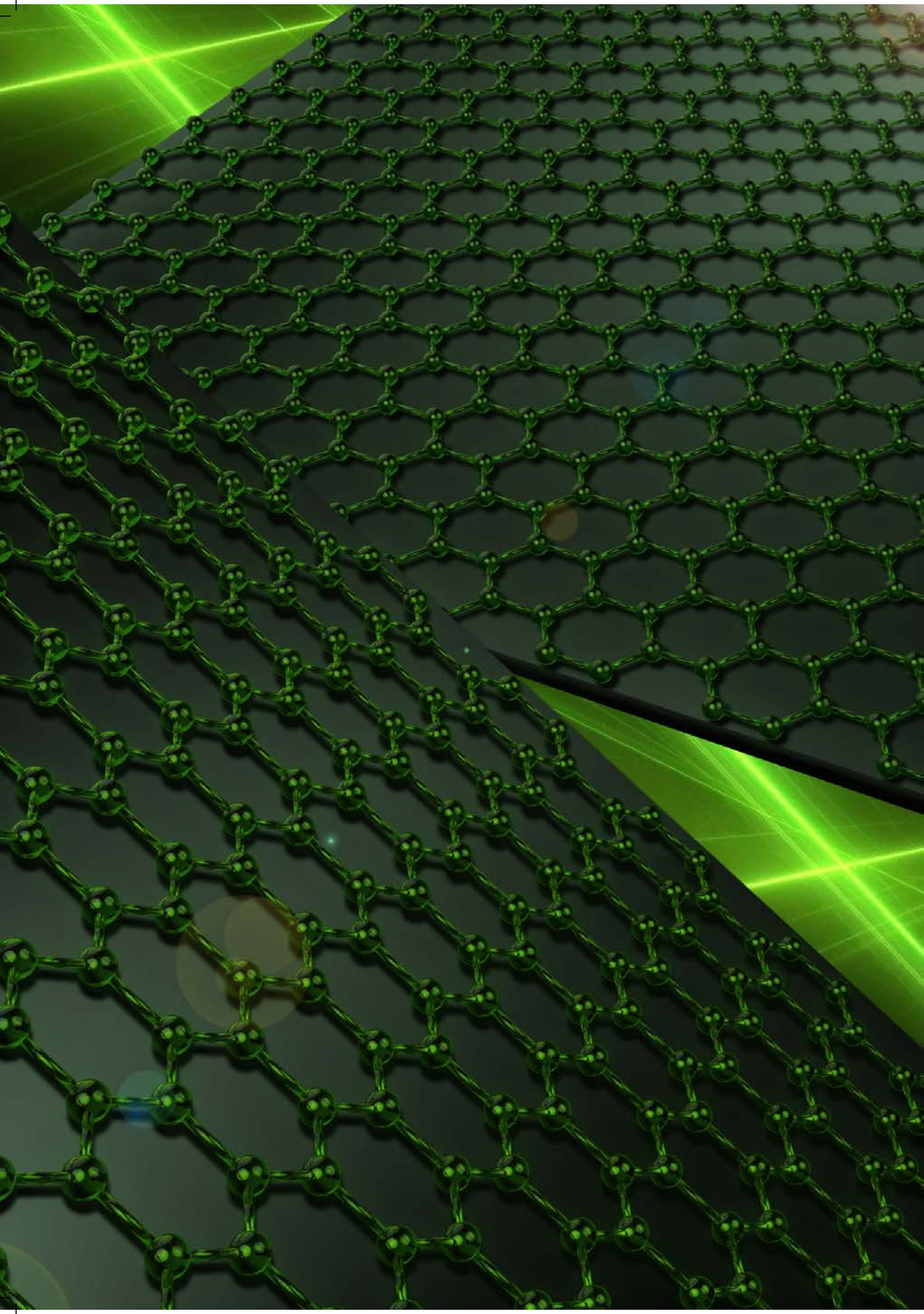
We further attempted to reverse the effect by applying a voltage across the graphene strip in order to try and induce motion of the NaCl droplet. No motion was observed even when the adhesion force of the droplet to the substrate was minimized by introducing a tilt of the stage. We believe that the counterions in the droplet (together with electrons from the graphene) neutralize nearly all the charges attracted to graphene/PET, therefore the direct force will have no effect on it. The estimated contribution of the wind force is far too small to be observed.

**REFERENCES**

- [1] J. Yin, Z. Zhang, X. Li, J. Zhou, and W. Guo. Harvesting Energy from water flow over graphene? *Nano Lett.*, 12:1736–1741, 2012.
- [2] P. Dhiman, F. Yavari, X. Mi, H. Gullapalli, Y. Shi, P. M. Ajayan, and N. Koratkar. Harvesting Energy from Water Flow over Graphene. *Nano Lett.*, 11:3123–3127, 2011.
- [3] J. Yin, X. Li, J. Yu, Z. Zhang, J. Zhou, and W. Guo. Generating electricity by moving a droplet of ionic liquid along graphene. *Nature Nanotech.*, 9:378–383, 2014.
- [4] A.V. Delgado, F. Gonzalez-Caballero, R.J. Hunter, L.K. Koopal, and J. Lyklema. Measurement and interpretation of electrokinetic phenomena. *Journal of Colloid and Interface Science*, 309:194–224, 2007.
- [5] H. Helmholtz. Ueber einige Gesetze der Vertheilung elektrischer Ströme in körperlichen Leitern mit Anwendung auf die thierisch-elektrischen Versuche. *Annalen der Physik und Chemie*, 165:211–233, 1853.
- [6] O. Stern. *Z. Electrochem*, 30:508, 1924.
- [7] D. Li. *Electrokinetics in microfluidics*. Elsevier Academic Press, 2004.
- [8] H.-C. Chang and L. Y. Yeo. *Water-assisted highly efficient synthesis of impurity-free single-walled carbon nanotubes*. Cambridge University Press, 2009.
- [9] P. Kral and M. Shapiro. Nanotube Electron Drag in Flowing Liquids. *Physical Review Letters*, 86:131–134, 2000.
- [10] S. Ghosh, A. K. Sood, and N. Kumar. Carbon nanotube flow sensors. *Science*, 299:1042–1044, 2003.
- [11] Zhao Y. Individual water-filled single-walled carbon nanotubes as hydroelectric power converters. *Adv. Mater.*, 20:1772–1776, 2008.
- [12] J. Liu, L. Dai, and J. W. Baur. Multiwalled carbon nanotubes for flow-induced voltage generation. *J. Appl. Phys.*, 101:064312, 2007.
- [13] A. K. M. Newaz, D. A. Markov, D. Prasai, and K. I. Bolotin. Graphene Transistor as a probe for streaming potential. *Nano Lett.*, 12:2931–2935, 2012.
- [14] K. Hata, D. N. Futaba, K. Mizuno, T. Namai, M. Yumura, and S. Iijima. Electrokinetically-driven microfluidics and nanofluidics. *Science*, 306:1362–1364, 2004.
- [15] K. Liu, Sun. Y. H., L. Chen, C. Feng, X. F. Feng, K. L. Jiang, Y. G. Zhao, and S. S. Fan. Controlled growth of super-aligned carbon nanotube arrays for spinning continuous unidirectional sheets with tunable physical properties. *Nano Lett.*, 8:700–705, 2008.

- [16] G. Shi, J. Liu, C. Wang, B. Song, Y. Tu, J. Hu, and H. Fang. Ion Enrichment on the Hydrophobic Carbon-based Surface in Aqueous Salt Solutions due to Cation- $\pi$  Interactions. *Scientific Reports*, 3:3436, 2013.
- [17] S. J. Tsai and R. J. Yang. Bimodal behaviour of charge carriers in graphene induced by electric double layer. *Scientific Reports*, 6:30731, 2016.
- [18] S. Yang, Y. Su, Y. Xu, Q. Wu, Y. Zhang, M. B. Raschke, M. Ren, J. Wang Y. Chen, W. Guo, Y. R. Shen, and C. Tian. Mechanism of Electric Power Generation from Ionic Droplet Motion on Polymer Supported Graphene. *J. Am. Chem. Soc.*, 42:13746–13752, 2018.
- [19] D. A. Cherepanov, B. A. Feniouk, W. Junge, and A. Y. Mulkidjanian. Low dielectric permittivity of water at the membrane interface: effect on the energy coupling mechanism in biological membranes. *Biophys. J.*, 85:1307–1316, 2003.





# 4

## DYNAMIC TUNNELING JUNCTION AT THE ATOMIC INTERSECTION OF TWO TWISTED GRAPHENE EDGES

*The investigation of the transport properties of single molecules by flowing tunneling currents across extremely narrow gaps is relevant for challenges as diverse as the development of molecular electronics and sequencing of DNA. The achievement of well-defined electrode architectures remains a technical challenge, especially due to the necessity of high precision fabrication processes and the chemical instability of most bulk metals. Here, we illustrate a continuously adjustable tunneling junction between the edges of two twisted graphene sheets. The unique property of the graphene electrodes is the fact that the sheets are rigidly supported all the way to the atomic edge. By analyzing the tunneling current characteristics, we also demonstrate that the spacing across the gap junction can be controllably adjusted. Finally, we demonstrate the transition from the tunneling regime to contact and the formation of an atomic sized junction between the two edges of graphene.*

---

Parts of this chapter have been published as: A. Bellunato\*, S. Vrbica\*, C. Sabater, E. de Vos, R. Fermin, K. Kanneworff, F. Galli, J. M. van Ruitenbeek, G. Schneider, "Dynamic tunneling junction at the atomic intersection of two twisted graphene edges", *Nano Letters* **18** (4), 2505–2510 (2018). Patent applications: GB1610183.4, GB1610187.5

\*These authors contributed equally to this study

## 4.1. INTRODUCTION

The great potential that graphene offers as an electrode material for addressing individual molecules has been widely recognized. This is of particular importance in the study of electron transport across individual molecules [1–3], in the development of molecular electronics [4, 5], and for direct electron current readout in the quest of sequencing biopolymers [6, 7]. In a typical essay in any of these fields of research, a voltage is applied across a nanoscale gap between two metallic electrodes where the measured current contains information on the nature of the molecule bridging this gap. In absence of molecules in the gap the current that flows is a pure tunneling current, resulting from the finite overlap of the exponentially decaying electron wave functions on either side of the gap. Currently, nearly all experiments have been performed using some form of break junction devices with metallic electrodes, mostly gold [8]. Metallic electrodes pose serious limitations, associated with poor characterization and poor reproducibility of the molecule-electrode bonding configurations. The size and shapes of the metal electrodes are generally unknown, the shape and surface coverage are subject to rapid chemical and geometrical modifications, and the radius of curvature of the electrodes is much larger than the size of the molecules under study, notably in the case of the widely used gold electrodes at room temperature [9]. The large size and the poorly known shape of the electrodes limits accurate comparison with computational modeling [10]. Moreover, (gold) metal electrodes offer a wide variety of choice for the position of the molecules between the electrodes and for the bonding configurations, which lead to more unknowns in the analysis of the observations [11]. The size of the electrodes is of particular interest in the field of biopolymer sequencing, where the extent of the electrodes in the direction along the length of the biopolymer should ideally be close to the size of the individual building blocks forming the biopolymer.

For many of those concerns the use of graphene edge electrodes offers a promising approach (Figure 4.1). Graphene is a good conductor of electricity and has a thickness of just a single carbon atom. Further benefits of the use of graphene include the stability of the covalently bonded lattice, the fact that image charges are nearly absent which greatly simplifies the comparison with computational models and the fact that the edges offer a limited range of bonding configurations which can be further exploited by edge-specific chemical decorations. Graphene electrodes can be contacted via  $\pi$ -stacking [3, 12] or through covalent bonds [13–15], introducing selective docking sites for molecular trapping and characterization [16, 17].

Several approaches towards exploiting graphene electrodes for addressing individual molecules have already been reported, where the challenge is the required small size of the gap between the electrodes. By exploiting the surface tension of an evaporating solvent, a freely suspended sheet of graphene can be torn into forming a tunneling junction on a Si/SiO<sub>2</sub> substrate [18]. Alternatively, feedback-controlled

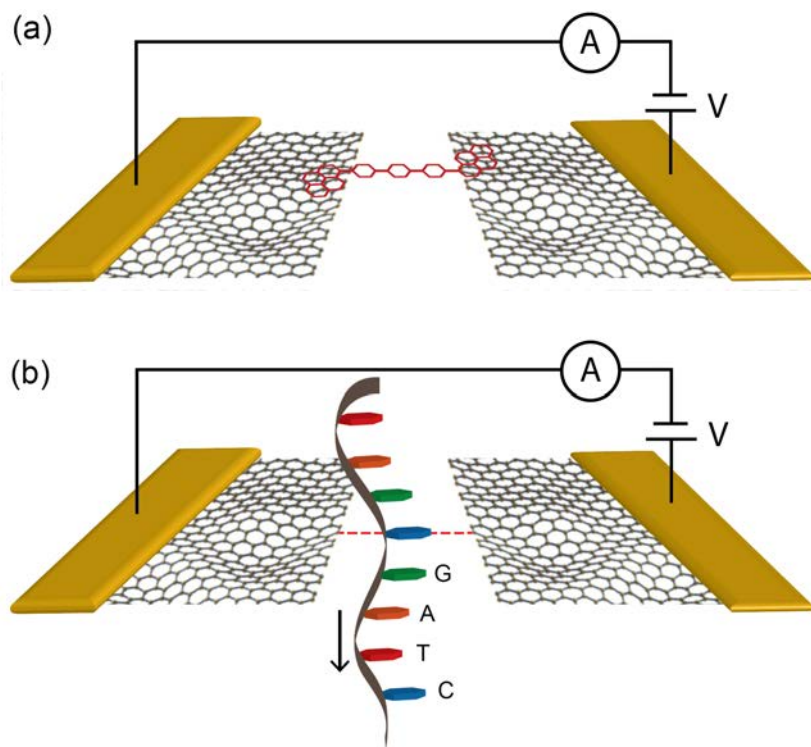


Figure 4.1: **Possible applications for the use of graphene nanoelectrodes.** (a) Investigation of single molecules for molecular electronics research. (b) DNA sequencing. Colored blocks are different nucleotides (A, T, C and G) of a single DNA strand. Red dashed line indicates tunneling current flowing through one of the nucleotides.

electroburning can be used for fabricating graphene nanogaps [1–4, 19], or high-resolution electron-beam patterning in combination with oxygen plasma etching [20]. These methods have in common that the size of the gap cannot be precisely and freely designed, and the resulting junctions are static: once created, the size of the nanogap cannot be adjusted. A drawback in the context of applications for sequencing is the fact that both the electrodes are sculpted on a common substrate that covers the gap between the electrodes, physically preventing the flow of molecules across the gap.

In this chapter we describe the fabrication and characterization of two graphene edge electrodes supported to the atomic edge, where electrons tunnel between the two carbon atoms facing each other. Using piezoelectric actuators of a modified scanning tunneling device, the two graphene edges are positioned relative to each other with sub-atomic precision, leaving a gap between the two facing carbon atoms that can be used for the translocation of molecules.

## 4.2. EXPERIMENTAL TECHNIQUES

### 4.2.1. ATOMIC FORCE MICROSCOPY (AFM)

Atomic force microscopy (AFM) was invented by Binnig, Quate and Gerber in 1986 [21]. AFM is a type of a scanning probe microscope that can achieve atomic resolution. The imaging signal is given by the force between the scanning probe (cantilever) and the sample surface. AFM is therefore not limited to conductive samples and probes, and it can be used to image both the  $\text{SiO}_2$  and the graphene surface at the same time.

All AFM measurements in this chapter were conducted in ambient conditions using a Bruker Multimode AFM® in tapping mode (TM AFM). In this mode the cantilever is driven to oscillate up-down at its resonance frequency (in the "down" position the tip is in direct contact with the sample). The amplitude and the frequency of the oscillation change as the surface height changes due to the interactions between the tip and the surface. Light from a laser is reflected off the cantilever and falls on a photodiode, which detects the deflection of the cantilever, as shown in Figure 4.2. The feedback loop compares the actual deflection frequency and amplitude with the

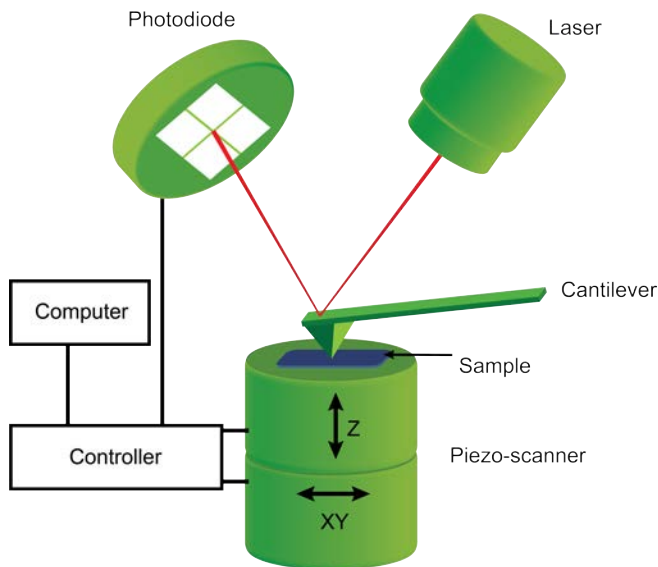


Figure 4.2: **Working principle of an AFM.** A cantilever is mechanically excited to oscillate at its resonance frequency. In tapping mode, light from the laser is reflected off the back side of the cantilever and reaches a photodiode, which detects the oscillations of the cantilever, influenced by the tip-sample forces. A feedback loop controls the piezo element holding the sample in order to restore the deflection to a user-defined setpoint. The feedback signal is used to obtain a topography image of the sample.

set-point, and in order to minimize the difference between these values it adjusts the tip height  $Z$  by adjusting the high voltage on the piezo element on which the sample resides. As the cantilever follows the profile of the surface, the feedback signal is used to obtain a height image.

Phase-imaging AFM records the phase-shift signal of the oscillation of the cantilever. These images often contain more information than the height images if the surface of the sample is not composed of one material. Two different materials might have the same height locally, but different interaction with the cantilever, thus giving a better contrast in the image.

The part of the graphene that we were interested in is at the very edge of the substrate. This required an AFM tip to be positioned close to the edge of the wafer in order to image over the edge and beyond the wafer support. Special care was taken in choosing the appropriate scanning parameters. Feedback was set to a low value in order to prevent fast descent of the cantilever once beyond the edge, and subsequent crashing. The line-scan direction was initially chosen to be parallel to the edge of the wafer, however in most cases this caused the tip to crash as soon as it reached the edge. The scan direction was soon after changed to be perpendicular to the edge. This way the cantilever was beyond the edge for only a few tens of nanometers during each line scan, and together with slow feedback parameters this approach yielded successful scanning.

#### 4.2.2. SCANNING ELECTRON MICROSCOPY (SEM)

A scanning electron microscope (SEM) is a type of electron microscope that produces images of a sample by scanning the surface with a focused beam of electrons. The electrons interact with atoms in the sample, producing various signals that contain information about the sample's surface topography and composition. The electron beam is scanned in a raster scan pattern, and the beam's position is combined with the detected signal to produce an image. All measurements were conducted in vacuum of  $10^{-5}$  mbar in a FEI Nova NanoSEM 200® which can achieve a resolution of around 20 nm.

The SEM mode used for the work reported in this chapter uses detection of the secondary electrons emitted by atoms excited by the electron beam. The number of secondary electrons that can be detected depends, among other things, on the specimen topography. By scanning the sample and collecting the secondary electrons that are emitted using a special detector, an image displaying the topography of the surface is created. Obtaining the highest resolution SEM images of the edge was hampered by the charging of the  $\text{SiO}_2$  which resulted in a high level of brightness at the edge area.

### 4.2.3. RAMAN SPECTROSCOPY

Raman spectroscopy is a technique that provides information on molecular vibrations that can be used for sample characterization. Typically, a sample is illuminated with a laser beam and electromagnetic radiation from the illuminated spot is collected with a lens and sent through a monochromator. Elastically scattered radiation at the wavelength corresponding to the laser line (Rayleigh scattering) is filtered out by either a notch filter, edge pass filter, or a band pass filter. The rest of the collected light, which is shifted in energy due to interactions with the vibrational energy levels of the molecules in the sample is dispersed onto a detector. Peaks in the Raman spectrum provide information on a structural fingerprint, quality of the material and presence of lattice defects.

The Raman spectroscopy was performed with a 532 nm laser source using a Witec Raman Alpha 3000®.

### 4.2.4. ELECTRICAL MEASUREMENTS

Electrical measurements are done in the modified homemade scanning tunneling microscope (STM) in ambient conditions (Figure 4.3). A bias voltage is applied between two conducting samples while piezo actuator moves one of the samples towards the other in small steps. When the samples are a few nanometers away, a tunneling current is detected, and current-voltage and current-distance characteristics can be obtained. Details of the setup and its operation are described in section 4.5.

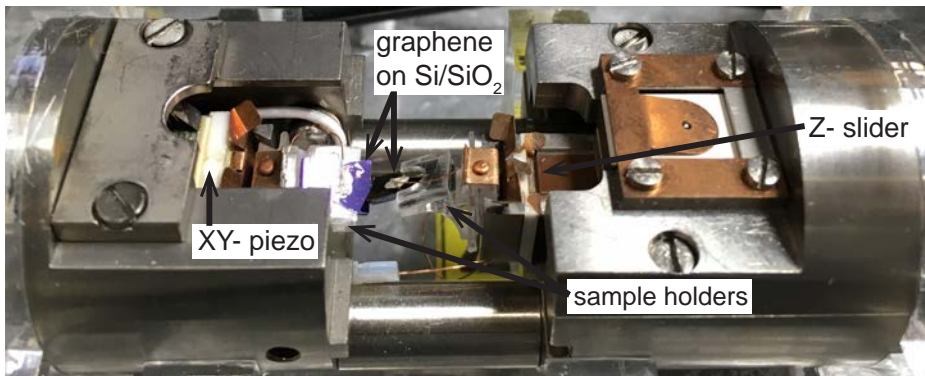


Figure 4.3: Modified homemade scanning tunneling microscope with two sample holders.

#### 4.2.5. GRAPHENE FILM DEPOSITION

The undoped Si/SiO<sub>2</sub> wafers with a polished oxide surface 285 nm thick are purchased from Sieger Wafers®. The supports are cleaned by organic solvents (acetone, isopropanol, ethanol), further cleaned in a piranha solution (1 : 3 = hydrogen peroxide : sulphuric acid) and afterwards exposed to O<sub>2</sub> plasma at 0.3 mbar and 60 W for several minutes. The piranha solution and the plasma aim to clean the surface from any organic residuals and increase the hydrophilicity of the surface, in order to facilitate the deposition of the graphene.

The graphene obtained by chemical vapor deposition (CVD) on a Cu substrate is purchased from Graphenea®. The graphene samples are spin-coated by a polymer (PMMA or PCA) and briefly back-etched in O<sub>2</sub> plasma 0.3 mbar 60 W for 10s in order to remove any carbon trace from the back-side of the copper substrate. Afterwards, the copper is etched in 0.5 M solution of ammonium persulfate, while the polymer works as a support. The film is rinsed three times in ultrapure water to remove residuals of ammonium persulfate from the surface of graphene and transferred over the wafers. After the transfer on the SiO<sub>2</sub> supports, the samples are dried on a hot plate and stored in vacuum.

### 4.3. FIRST APPROACH: BREAKING OF POLYMER-COVERED GRAPHENE

The uniform extension of the graphene film up to the extremity of its support is a prerequisite for the assembly of the tunneling junction. If the distance between the electrodes is larger than a few nanometers, no tunneling current will be detected. This requires full graphene coverage of the wafer all the way to its edge.

As a first method of obtaining graphene edge electrodes on Si/SiO<sub>2</sub> wafers, the so-called *broken-graphene* approach was used. The first of the two broken-graphene methods that we employed is schematically shown in Figure 4.4. The Si/SiO<sub>2</sub> wafer is weakened by making a notch with a diamond knife on the oxide side. Graphene is transferred on top of the wafer via the polymer-mediated method described in section 4.2.5, using polymethyl methacrylate (PMMA). The wafer is subsequently broken by exerting a three-point force (red arrows), initiating a crack along a low-index crystal plane of the wafer. The PMMA support layer was left on the graphene during the breaking process in order to protect it from potential damage. The polymer was later removed by putting the wafers overnight in acetone and subsequent flushing with acetone, isopropanol, ethanol and drying with nitrogen gas. The process resulted in two halves of the wafer with graphene on top.

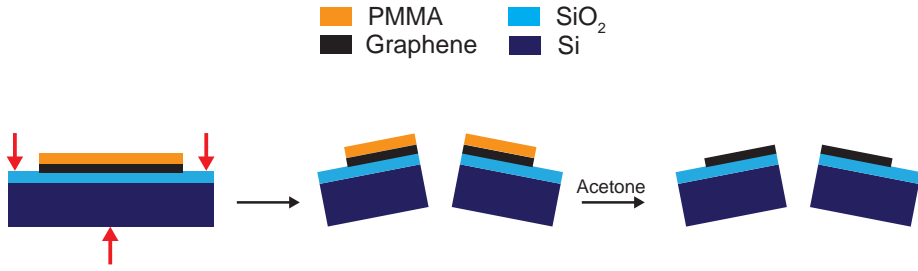


Figure 4.4: **Schematic representation of the broken-graphene technique for graphene on Si/SiO<sub>2</sub> with protective PMMA layer on top.** Force is exerted on the wafer that carries the graphene covered with polymer and two halves of the wafer are obtained. The polymer is removed by subsequent cleaning with acetone.

4

### 4.3.1. RESULTS AND DISCUSSION

Figure 4.5(a), (b) shows the phase and height AFM images of the edge of the wafer, respectively. The difference between the two materials can clearly be seen from the phase image, confirming that a large part of graphene in the vicinity of the edge (darker area on the top left in Figure 4.5(b)) is missing. The bright yellow spots are attributed to polymer residues. The inset in Figure 4.5(b) shows a step-height of around 2 nm between the graphene and the SiO<sub>2</sub> (line 1). The expected thickness

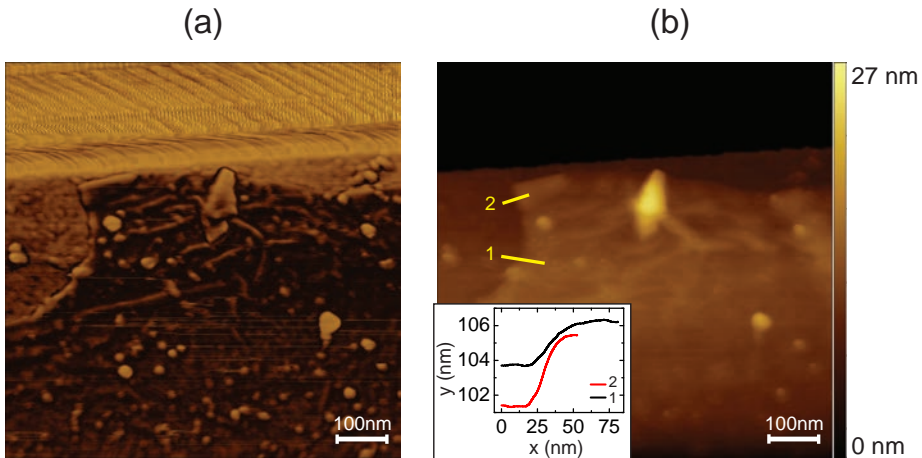


Figure 4.5: **AFM images of a broken graphene (first method).** (a) Phase and (b) height image of graphene in the vicinity of the wafer edge (black area on top in (b)). The inset shows height profiles corresponding to lines 1 and 2. Line 1 goes over the SiO<sub>2</sub> - graphene step and shows a height of around 2 nm. Line 2 goes over the folded graphene patch and shows a step-height of around 4 nm.

of the graphene sheet is around 0.35 nm. In the literature, however, AFM measurements report a wide range of values for single layer graphene thickness (between 0.4 and 1.7 nm) [22]. This discrepancy has been attributed to tip-surface interactions, image feedback settings, imaging force and surface chemistry, as well as the graphene-substrate adsorbate layer [22]. For the CVD grown graphene transferred from copper onto Si/SiO<sub>2</sub> wafer, the value of around 1.8 nm is reported [23] which is in agreement with the value that we obtained. Line 2 shows a profile along what appears to be folded graphene near the edge of the wafer, further confirmed by the step-height of around 4 nm. Out of all the samples obtained with this technique we did not observe graphene reaching the edge. We found that the closest distance between the graphene and the wafer edge in this type of samples is around 18 nm.

The most likely explanation for the missing graphene patches in the vicinity of the edge is the strain induced in the graphene during breaking which causes it to stretch. After putting the samples in acetone, graphene at the edge presumably gets removed along with the polymer residue or it folds back on itself.

#### 4.4. SECOND APPROACH: BREAKING OF BARE GRAPHENE

The second broken-graphene method that we employed uses the same approach as the first one, with one difference: the polymer layer is removed from graphene before breaking of the wafer (Figure 4.6).

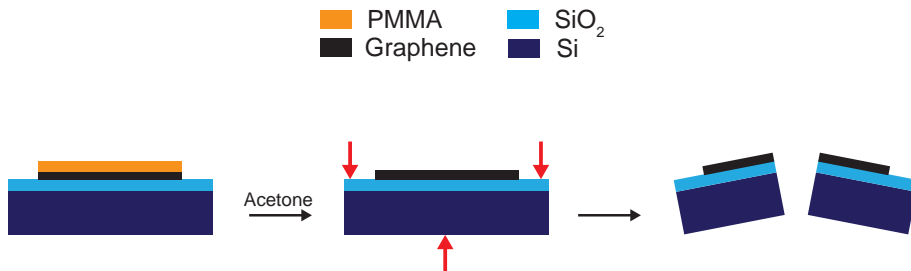


Figure 4.6: **Schematic representation of the broken-graphene technique for bare graphene on Si/SiO<sub>2</sub>.** The polymer is removed by cleaning with acetone before the wafer is broken. Force is exerted on the wafer that has bare graphene and two halves of the wafer are obtained.

##### 4.4.1. RESULTS AND DISCUSSION

The AFM scans were purposely aimed at an area where both SiO<sub>2</sub> and graphene are visible. This was done in order to distinguish between the graphene and the substrate, and determine the distance of the graphene from the sample edge. Figure 4.7

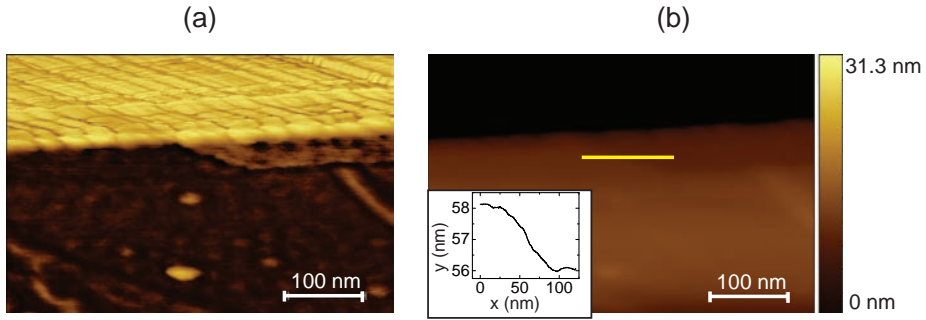


Figure 4.7: **AFM images of a broken graphene (second method)**. (a) Phase and (b) height image of a graphene edge. The inset shows a profile along the yellow line and a graphene step-edge of around 2 nm.

4

shows AFM phase and height images of the graphene at the edge of the wafer (black area on top in Figure 4.7(b)). The bright area on the right side of the edge in Figure 4.7(a) indicates a missing patch of graphene. This is confirmed by the 2 nm step-height along the yellow line in Figure 4.7(b) shown in the inset. On the left side, the graphene reaches the edge to within the resolution of the AFM.

From the results obtained with broken-graphene methods, it is clear that the more successful method is the one without polymer covering the graphene during the breaking process. However, this method also does not yield usable graphene edge electrodes. Even though graphene does reach the edge within AFM resolution, there are still parts of the wafer edge that have missing graphene patches. This suggests the possible presence of overhanging patches of graphene on the other half of the broken sample as a result of the stretching of graphene during breaking.

This is further confirmed by experiments of Victor Vollema and Carlos Sabater

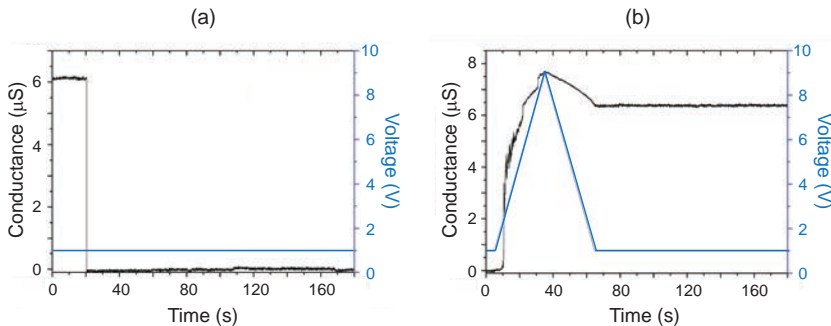


Figure 4.8: **Conductance measurements for graphene on a glass substrate** [24]. (a) Breaking of the graphene. (b) Graphene reformation as a result of a voltage ramp. High conductance over extended time period indicates stability of the contact.

[24] on a broken graphene on a glass substrate, which show the occurrence of a voltage-induced restoring effect on the broken carbon-carbon bonds. Figure 4.8(a) shows breaking of the graphene at a bias voltage of 1 V. The conductance drops and does not spontaneously change through relaxation of the substrate within the next few minutes. Figure 4.8(b) shows the conductance of a broken graphene junction during a voltage ramp to 9 V and back to 1 V, while the two halves were kept at tuning distance. The increase of the conductance indicates that the contact is re-established during the voltage ramp, and remains stable after the voltage is reduced to the initial value. This effect was observed multiple times and was independent on the polarity of the voltage: only the magnitude of the voltage was of importance. As an explanation for the restauration of contact we propose that the breaking produces overhanging flaps of graphene (the counter parts of the missing patches observed in AFM), that can be switched into contact with the other half by the electric force field. Due to the missing graphene patches at the edge of the wafers, this method was abandoned and further electrical measurements on these samples were not performed.

## 4.5. THIRD APPROACH: PLASMA ETCHING OF SUSPENDED GRAPHENE

As an alternative approach to breaking graphene, we utilized plasma etching in attempt to create fully functional graphene electrodes. We start by describing the fabrication process.

A Si/SiO<sub>2</sub> wafer is broken in half by introducing a notch on the surface at the edge of the wafer with a diamond knife. The notch initiates a crack that develops along a high-symmetry crystallographic direction of the silicon, yielding two wafers with straight edge profiles. Sharp edges are a prerequisite to have uniform edge electrodes and facilitate the approach of the tunnel junction.

The two wafer halves are further cleaned and mounted over a slit in a holder, facing each other at a distance of about a millimeter (Figure 4.9(a)). A graphene sheet supported by a layer of polycarbonate (PCA) [25] is deposited on top of the two wafer halves, bridging the gap between them. The schematics is shown in Figure 4.9(a). Figure 4.9(b) shows an optical photograph of the polymer-supported graphene, suspended between the two supports.

Subsequently, the holder with the wafers and the polymer-supported graphene are exposed from below to an isotropic H<sub>2</sub> plasma. The plasma removes the graphene suspended over the slit, while the polymer protects the part of graphene that covers the SiO<sub>2</sub> wafers. Next, the PCA coating is dissolved in chloroform, the assembly is rinsed in methanol and isopropanol (Figure 4.9(c)), and the resulting graphene edge electrodes are imaged using optical microscopy (Figure 4.9(d)). The protective role of the polymer towards the highly reactive hydrogen plasma is confirmed from Raman

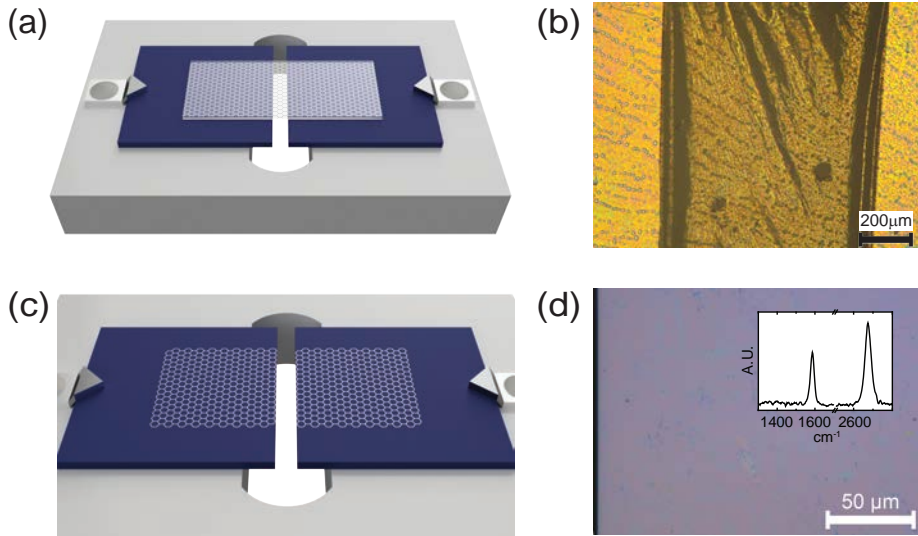


Figure 4.9: **Fabrication of graphene edge electrodes.** (a) Schematic illustration of a graphene layer protected by a polymer coating (white shading covering the graphene) bridging the gap between two Si/SiO<sub>2</sub> wafer halves mounted over the slit of a holder. (b) Optical microscopy image showing the two Si/SiO<sub>2</sub> wafer halves (yellow) bridged by the freestanding polymer-coated graphene (dark yellow). (c) Schematic illustration of the setup after plasma etching and polymer removal. (d) Optical microscopy image of the supported graphene edge (visible at the far left) after polymer removal. The inset shows a Raman spectrum of the graphene after plasma etching and polymer removal.

spectroscopy (see discussion below) by the presence of a strong G peak [26] around  $1590\text{ cm}^{-1}$  and a negligible D peak around  $1340\text{ cm}^{-1}$  (inset in Figure 4.9(d)).

#### 4.5.1. RESULTS AND DISCUSSION

Prior to performing tunneling measurements we characterized the graphene edge electrodes using scanning Raman spectroscopy, scanning electron microscopy (SEM) and atomic force microscopy (AFM), Figure 4.10. The mapping in Figure 4.10(a) overlaps Raman peak intensity distributions over the surface of the electrode near the edge, with the 2D band around  $2700\text{ cm}^{-1}$  shown in green, the G band at  $1590\text{ cm}^{-1}$  shown in blue, and the D band at  $1340\text{ cm}^{-1}$  shown in red. The graphene extends uniformly all over the surface of the SiO<sub>2</sub> substrate, beyond which the mapping appears black (left side of the image). The uniformity of the color scale illustrates the quality of the graphene. Representative single-spot spectra acquired at the edge of the support are shown in Figure 4.10(b). The ratio of the intensities of the 2D and the G peaks is in agreement with the ratio expected for monolayer graphene, while the onset of a D peak at the edge is characteristic of the breaking in the symmetry

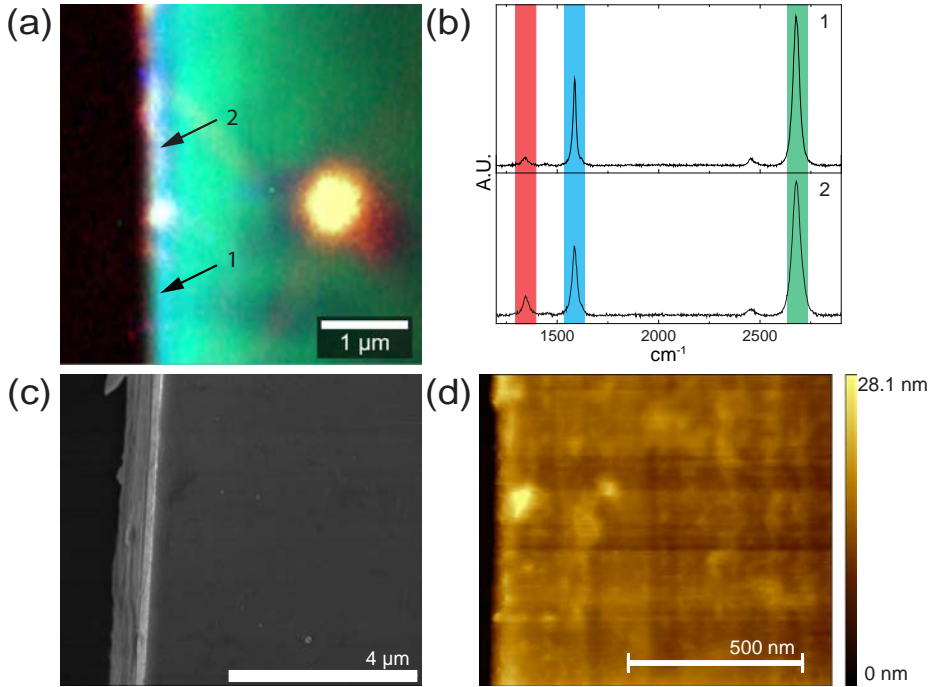


Figure 4.10: **Characterization of the graphene edge.** (a) Overlay of the Raman mapping of the D band ( $1560\text{ cm}^{-1}$ , red tone), G band ( $1580\text{ cm}^{-1}$ , blue tone) and 2D band ( $2667\text{ cm}^{-1}$ , green tone). The large yellow island is a polymer residue. (b) Raman spectra of two single points on the edge, marked with arrows in panel (a). (c) SEM micrograph of the edge electrode. (d) AFM height profile of a graphene edge electrode.

of the graphene lattice [27]. The relative intensity of the D band with respect to the G and 2D bands is an indicator of the uniformity of the graphene lattice [28]. The bright yellow spot at the right side of the image is attributed to a polymer residue. Such polymer residues could be removed by high-temperature annealing. The high temperatures required for cleaning of the surface may, however, induce ruptures of the graphene sheet, displacing the graphene from the edge of the substrate due to differences in thermal expansion coefficients of graphene and Si/SiO<sub>2</sub>. Accordingly, no annealing procedure was performed on the samples.

Figure 4.10(c) shows a SEM micrograph of a graphene edge electrode on a Si/SiO<sub>2</sub> wafer. The small darker regions indicate the formation of local graphene bi-layer islands during the CVD growth [29]. Additionally, small white features are attributed to polymer residues. We observe no variations in the color contrast of the graphene film on top of the SiO<sub>2</sub> in proximity of the edge, suggesting the continuous presence of the film.

Neither SEM nor Raman can resolve the extension of the graphene sheet to the edge of its substrate down to the nanometer scale. We refine the characterization to-

wards higher resolution by performing atomic force microscopy (AFM). Figure 4.10(d) shows a tapping mode AFM topography image of the surface of graphene up to the edge and beyond the wafer support (black area on the left in Figure 4.10(d)). The height profile confirms the extension of the graphene to the edge of the support. The bright areas correspond to higher regions such as graphene bi-layer areas typical of CVD grown graphene, as well as polymer residues accumulated near the edges of the graphene film during the removal of the polymer. We observe uniformity of the color contrast up to the edge of the wafer to within the AFM resolution ( $\sim 5$  nm).

The final test of whether graphene extends to the edge is in the observation of a tunneling current. Tunneling currents decay exponentially with the distance between the electrodes. If the graphene would be displaced from the edge of the support by more than a few nanometers, no tunneling current could be measured. Tunnel junctions between two graphene edges are formed by approaching a pair of edge electrodes using a modified piezo actuator of a scanning tunneling microscope (STM), operating under ambient conditions. The piezo actuator permits the controlled approach into tunneling distance of the graphene layers on the Si supports. The graphene layers are electrically connected by attaching copper wires by a drop of silver epoxy. The wafers are tilted downwards by  $15^\circ$  in order to avoid the Si substrates hampering the approach of the electrodes. A rotation of one of the supports around the Z-axis (Figure 4.11) leads to the formation of a single point of intersection between the two graphene edges. Ideally, two single carbon atoms meet at the intersection, constituting an atomic tunneling junction. Piezo actuator controlled displacements in X and Y directions permit selecting fresh spots for tunneling.

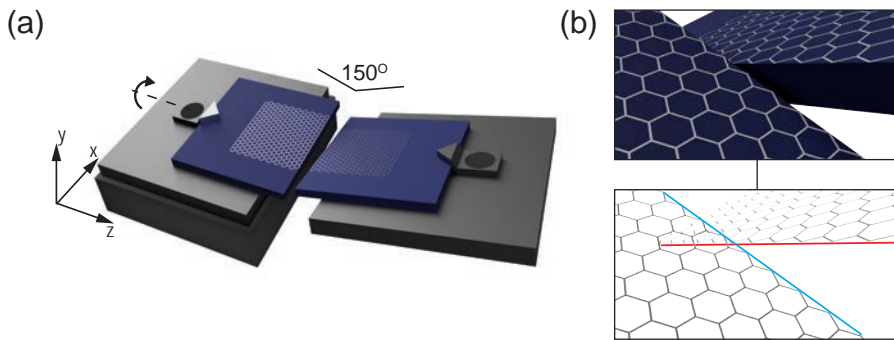


Figure 4.11: **Schematic illustration of the method for producing a dynamically adjustable graphene-graphene junction.** (a) Two independent graphene electrodes, each supported to the atomic edge, can be approached edge-to-edge with sub-atomic precision, creating a junction between two single rows of carbon edge atoms. The electrodes are rotated around the Z-axis and tilted downward in order to form a well-defined intersection point between the two electrodes, and for preventing mechanical contact of the supports. (b) Illustration of the carbon-carbon point contact, formed at the intersection of two graphene sheet edges.

Figure 4.12(a) shows an example of the measured current-voltage ( $IV$ ) dependence of a graphene-graphene tunnel junction, for a bias voltage sweep of  $\pm 1.0$  V. The sigmoidal shape of the curve is a distinctive feature of electron tunneling through a potential barrier. Here, the barrier height is determined by the work function, and the width of the barrier is given by the distance between the graphene edges. We employ the Simmons model for tunneling through symmetric barriers [30] to fit the size of the vacuum gap and the height of the work function (see Appendix). From this fit we obtain a distance of 1.3 nm ( $\pm 5\%$ ), and an effective work function  $\Phi = 1.4$  eV ( $\pm 8\%$ ). The work function is significantly lower than the values reported from Kelvin probe microscopy on the face of graphene sheets, which range from 4.45 to 4.8 eV, depending on the doping [31]. Much lower work functions, ranging from 0.25 to 1.0 eV are typically found from Simmons fits and edge tunneling, as reported for graphene nanogaps obtained from electroburning [2, 3, 5]. In our case, the chemistry of the edges under fabrication conditions influences the work function [32–34]. Since the sample is etched in  $H_2$  plasma, most of the carbon dangling bonds are presumably hydrogenated and this reduces the work function below 4 eV [35]. The presence of chemisorbed and physisorbed species at the edges of the electrodes under ambient conditions is expected to further reduce the work function [3].

The independent positioning of our edge electrodes allows fine adjustment of the gap. Figure 4.12(b) shows a current-distance curve,  $I(z)$ , measured at a bias voltage of  $V = 0.1$  V, black curve. We fit the measured  $I(z)$  curve with an exponential function (in red) using the effective work function  $\Phi$  as obtained from the  $IV$  characteristic

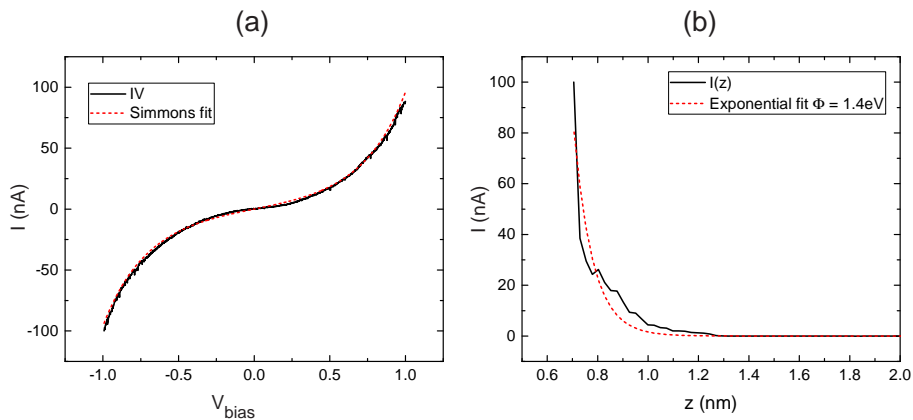


Figure 4.12: **Electrical characterization of a dynamically adjustable graphene-graphene edge tunneling junction.** (a) Black curve: Current-voltage characteristics of the junction in the tunneling regime. Red curve: fit to the Simmons model with a vacuum gap size of  $z = 1.3$  nm and a barrier height of  $\Phi = 1.4$  eV. (b) Current-distance characteristics of the tunnel junction (black line). The red curve is an exponential fit for tunneling as a function of gap size, adopting the barrier height obtained from the fit in (a).

in Figure 4.12(a). Since the shape of the curve is fully determined and only the exponential pre-factor is freely adjustable, the fit provides strong confirmation of the vacuum tunneling origin of the current. We are not aware of any previous methods for recording the tunneling current between the edges of two graphene sheets as a function of their distance. Although the measured curve still has some irregularities due to vibrations and possibly due to fluctuations in adsorbents, the observed exponential dependence confirms that we are able to tune the gap of a tunnel junction with sub-nanometric precision.

Moving the graphene electrodes closer together, the electron transport across the junction transforms from the tunneling to the contact regime. The configuration with sample holders rotated around the Z-axis should lead to an initial point contact between single carbon atoms at the intersection of the two edges of the graphene electrodes. Figure 4.13(a) shows an  $I(z)$  curve for a junction during the transition from the tunnel regime to the point contact regime, at a bias voltage of 0.1 V, black curve. Following the exponential increase of the current in the tunnel regime we observe a kink at about  $3 \mu\text{A}$ , indicating a switch to contact. Pushing the electrodes further into contact increases the current further, approximately linearly. The onset of the linear regime is found at a contact resistance around  $30 \text{ k}\Omega$ , which is of the order of the quantum of resistance expected for atomic point contacts ( $12.9 \text{ k}\Omega$ ). Figure 4.13(b) shows a histogram of the current values observed at the kink, for 29 independent junctions formed. The histogram shows that, statistically, the onset of the linear resistance regime is found at  $R_{\text{total}} = 28 \text{ k}\Omega$ . Note that this resistance is the actual contact quantum point contact resistance  $R_{\text{qpc}}$ , measured in series with the

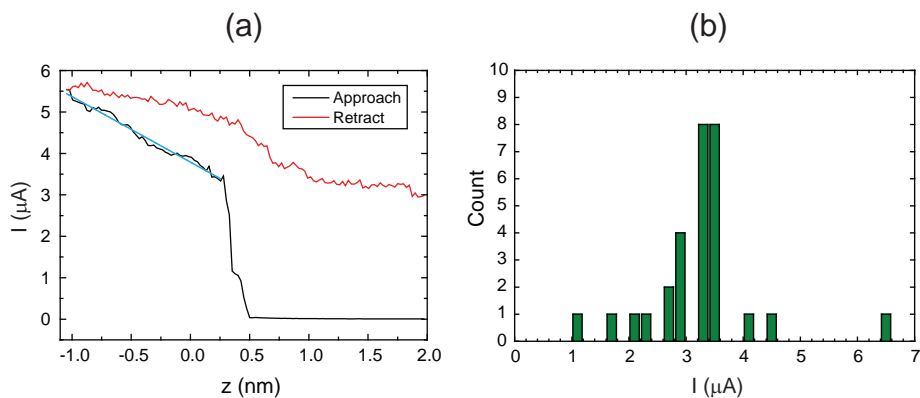


Figure 4.13: **From tunneling regime to point contact.** (a) Black: approach curve obtained for the closing of the nanogap, showing a transition from the exponential tunneling regime to a linear point contact regime (indicated by the blue line fit). Red: retraction curve showing hysteresis attributed to bond formation. (b) Green bars: histogram of the point contact formation (current at the kink in (a)) for 29 junctions, at a bias voltage of 0.1 V.

resistance of the two graphene electrodes,  $R_{2g}$  (see the Appendix for the details). The estimated  $R_{2g}$  value is  $17 \pm 3 \text{ k}\Omega$ , which in return gives the value for  $R_{qpc} = 11 \pm 3 \text{ k}\Omega$ . This is in good agreement with the value calculated for carbon-carbon atomic contacts at low strain [36], and with the quantum of resistance.

The linear trend to higher conductance after the kink suggests that the contact between the edges of the two graphene sheets can be increased by indentation. Note that we are only indenting the electrodes by a few atomic distances. The linear trend in conductance agrees with the 2-dimensional geometry of the graphene sheets, and differs from the nearly quadratic growth of conductance for 3-dimensional metallic contacts [9].

When we retract the electrodes after this indentation, in order to restore the vacuum gap, we observe hysteresis, as shown by the red curve in Figure 4.13(a). During retraction, the conductance remains high, and after a small downward step near the point where the initial contact was formed, the contact is not broken even for further stretching of the junction over several nanometers. The persistence of high conductance suggests that strong bonds have been formed under the influence of the high mechanical pressure, possibly in combination with the potential of 0.1 V applied across the junction. We speculate that carbon-carbon bonds are formed between the graphene sheets during indentation, despite the fact that all carbon bonds should initially be saturated. The long distance over which a high-conductance state survives (up to 3 nm or more) suggests that elongated atomic-chain-like structures are formed in the retraction process, as has been observed previously in transmission electron microscope experiments [36–38], and in first-principles molecular dynamics [16, 39, 40]. The validity of this speculation will need further experiments for detailed evaluation.

#### 4.5.2. CONCLUSION & OUTLOOK

We have presented a system that consists of dynamically adjustable graphene-graphene edge tunneling junctions. The independently supported graphene electrodes uniquely allow the fine adjustment of the gap size. The tunability of the gap is relevant for applications of such junctions, especially in the fields of single-molecule characterization, biosensing, and DNA sequencing. The junction can be adapted for sensing in liquid environments, required for the translocation of molecules such as DNA strands across the gap and recording their electric fingerprint [41]. During the testing of the junctions we have monitored the transition from the tunnel regime to atomic-size contact, and observed a preferred initial contact resistance value of  $R_{pc} = 28 \text{ k}\Omega$ . The presence of hysteresis in the contact formation-and-breaking cycle indicates that bonds are formed between the graphene electrodes under influence of mechanical pressure. With further developments of our system under controlled atmosphere, in liquid environments and at cryogenic temperatures, we believe that our findings will advance molecular electronics research, open the way to research of

atomic-size junctions in graphene and find applications in sensing and biopolymer sequencing.

## REFERENCES

- [1] F. Prins, A. Barreiro, J. W. Ruitenber, J. S. Seldenthuis, N. Aliaga-Alcalde, L. M. K. Vandersypen, and H. S. J. van der Zant. Room-Temperature Gating of Molecular Junctions Using Few-Layer Graphene Nanogap Electrodes. *Nano Lett.*, 11:4607–11, 2011.
- [2] C. Nef, L. Pósa, P. Makk, W. Fu, A. Halbritter, C. Schönenberger, and M. Calame. High-yield fabrication of nm-size gaps in monolayer CVD graphene. *Nanoscale*, 6:7249–7254, 2014.
- [3] K. Ullmann, P. B. Coto, S. Leitherer, A. Molina-Ontoria, N. Martín, M. Thoss, and H. B. Weber. Single-molecule junctions with epitaxial graphene nanoelectrodes. *Nano Lett.*, 15:3512–8, 2015.
- [4] H. Wen, W. Li, J. Chen, G. He, L. Li, M. A. Olson, A. C.-H. Sue, J. F. Stoddart, and X. Guo. Complex formation dynamics in a single-molecule electronic device. *Sci. Adv.*, 2:1601113, 2016.
- [5] C. S. Lau, J. A. Mol, J. H. Warner, and G. A. D. Briggs. Nanoscale control of graphene electrodes. *Phys. Chem. Chem. Phys.*, 16:20398–20401, 2014.
- [6] J. Lagerqvist, M. Zwolak, and M. Di Ventra. Fast DNA Sequencing via Transverse Electronic Transport. *Nano Lett.*, 6:779–782, 2006.
- [7] H. Arjmandi-Tash, L. A. Belyaeva, and G. F. Schneider. Single molecule detection with graphene and other two-dimensional materials: nanopores and beyond. *Chem Soc Rev.*, 45:476–493, 2016.
- [8] J. C. Cuevas and E. Scheer. *Molecular electronics: an introduction to theory and experiment*. World Scientific, New York, 2010.
- [9] N. Agrait, A. Levy-Yeyati, and J. M. van Ruitenbeek. Quantum properties of atomic-sized conductors. *Phys. Rep.*, 377:81–279, 2003.
- [10] M. L. Perrin, C. J. O. Verzijl, C. A. Martin, A. J. Shaikh, R. Eelkema, J. H. Van Esch, J. M. Van Ruitenbeek, J. M. Thijssen, H. S. J. Van Der Zant, and D. Dulić. Large tunable image-charge effects in single-molecule junctions. *Nature Nanotech.*, 8:282–287, 2013.
- [11] M. Paulsson, C. Krag, T. Frederiksen, and M. Brandbyge. Conductance of Alkanedithiol Single-Molecule Junctions: A Molecular Dynamics Study. *Nano Lett.*, 9:117–121, 2009.
- [12] W. Fu, C. Nef, A. Tarasov, M. Wipf, R. Stoop, O. Knopfmacher, M. Weiss, M. Calame, and C. Schönenberger. High mobility graphene ion-sensitive field-effect transistors by noncovalent functionalization. *Nanoscale*, 5:12104, 2013.

- [13] M. Baraket, R. Stine, W. K. Lee, J. T. Robinson, C. R. Tamanaha, P. E. Sheehan, and S. G. Walton. Aminated graphene for DNA attachment produced via plasma functionalization. *Appl. Phys. Lett.*, 100:233123, 2012.
- [14] C. K. Chua and M. Pumera. Covalent chemistry on graphene. *Chem. Soc. Rev.*, 42:3222, 2013.
- [15] Y. Liu, X. Dong, and P. Chen. Biological and chemical sensors based on graphene materials. *Chem. Soc. Rev.*, 41:2283–2307, 2012.
- [16] B. Zhang and T. Cui. An ultrasensitive and low-cost graphene sensor based on layer-by-layer nano self-assembly. *Appl. Phys. Lett.*, 98:73116, 2011.
- [17] G. Xu, J. Abbott, L. Qin, K. Y. M. Yeung, Y. Song, H. Yoon, J. Kong, and D. Ham. Electrophoretic and field-effect graphene for all-electrical DNA array technology. *Nat. Commun.*, 5:4866, 2014.
- [18] H. M. Wang, Z. Zheng, Y. Y. Wang, J. J. Qiu, Z. B. Guo, Z. X. Shen, and T. Yu. Fabrication of graphene nanogap with crystallographically matching edges and its electron emission properties. *Appl. Phys. Lett.*, 96:23106, 2010.
- [19] H. Sadeghi, J. Mol, C. Lau, A. Briggs, J. Warner, and C. J. Lambert. Conductance enlargement in picoscale electroburnt graphene nanojunctions. *Proc. Natl. Acad. Sci. U. S. A.*, 112:2658–63, 2016.
- [20] Y. Cao, S. Dong, S. Liu, L. He, L. Gan, X. Yu, M. L. Steigerwald, X. Wu, Z. Liu, and X. Guo. Building high-throughput molecular junctions using indented graphene point contacts. *Angew. Chemie - Int. Ed.*, 51:12228–12232, 2012.
- [21] G. Binnig, C. F. Quate, and Ch. Gerber. Atomic force microscope. *Phys. Rev. Lett.*, 56:930, 1986.
- [22] C. J. Shearer, A. D. Slattery, A. J. Stapleton, J. G. Shapter, and C. T. Gibson. Accurate thickness measurement of graphene. *Nanotechnology*, 27, 2016.
- [23] W. Jung, J. Park, T. Yoon, T. Kim, S. Kim, and C. Han. Prevention of Water Permeation by Strong Adhesion Between Graphene and SiO<sub>2</sub> Substrate. *Small*, 10:1704–1711, 2014.
- [24] Victor Vollema. Viability of a graphene nanojunction. *Master thesis*, 2016.
- [25] J. D. Wood, G. P. Doidge, E. A. Carrion, J. C. Koepke, J. A. Kaitz, I. Datye, A. Behnam, J. Hewaparakrama, B. Aruin, Y. Chen, H. Dong, R. T. Haasch, J. W. Lyding, and E. Pop. Annealing free, clean graphene transfer using alternative polymer scaffolds. *Nanotechnology*, 26:55302, 2015.

- [26] A. C. Ferrari, J. C. Meyer, V. Scardaci, C. Casiraghi, M. Lazzeri, F. Mauri, S. Piscanec, D. Jiang, K. S. Novoselov, S. Roth, and A. K. Geim. Raman Spectrum of Graphene and Graphene Layers. *Phys. Rev. Lett.*, 97:187401, 2006.
- [27] C. Casiraghi, A. Hartschuh, H. Qian, S. Piscanec, C. Georgi, A. Fasoli, K. S. Novoselov, D. M. Basko, and A. C. Ferrari. Raman Spectroscopy of Graphene Edges. *Nano Lett.*, 9:1433–1441, 2009.
- [28] A. C. Ferrari and D. M. Basko. Raman spectroscopy as a versatile tool for studying the properties of graphene. *Nature Nanotech.*, 8:235–246, 2013.
- [29] X. Li, W. Cai, J. An, S. Kim, J. Nah, D. Yang, R. Piner, A. Velamakanni, I. Jung, E. Tutuc, S. K. Banerjee, L. Colombo, and R. S. Ruoff. Large-Area Synthesis of High-Quality and Uniform Graphene Films on Copper Foils. *Science*, 324:1312–1314, 2009.
- [30] J. G. Simmons. Generalized Formula for the Electric Tunnel Effect between Similar Electrodes Separated by a Thin Insulating Film. *J. Appl. Phys.*, 34:1793–1803, 1963.
- [31] A. Nagashima C. Oshima. Ultra-thin epitaxial films of graphite and hexagonal boron nitride on solid surfaces. *J. Phys. Condens. Matter*, 9:1–20, 1997.
- [32] H. Yuan, S. Chang, I. Bargatin, N. C. Wang, D. C. Riley, H. Wang, J. W. Schwede, J. Provine, E. Pop, Z. X. Shen, P. A. Pianetta, N. A. Melosh, and R. T. Howe. Engineering Ultra-Low Work Function of Graphene. *Nano Lett.*, 15:6475–6480, 2015.
- [33] S. M. Song, J. K. Park, O. J. Sul, and B. J. Cho. Determination of work function of graphene under a metal electrode and its role in contact resistance. *Nano Lett.*, 12:3887–3892, 2012.
- [34] Y. Shi, K. K. Kim, A. Reina, M. Hofmann, L. J. Li, and J. Kong. Work function engineering of graphene electrode via chemical doping. *ACS Nano*, 4:2689–2694, 2010.
- [35] D. G. Kvashnin, P. B. Sorokin, J. W. Brüning, and L. A. Chernozatonskii. The impact of edges and dopants on the work function of graphene nanostructures: The way to high electronic emission from pure carbon medium. *Appl. Phys. Lett.*, 102:183112, 2013.
- [36] O. Cretu, A. R. Botello-Mendez, I. Janowska, C. Pham-Huu, J. C. Charlier, and F. Banhart. Electrical transport measured in atomic carbon chains. *Nano Lett.*, 13:3487–3493, 2013.
- [37] C. Jin, H. Lan, L. Peng, K. Suenaga, and S. Iijima. Deriving Carbon Atomic Chains from Graphene. *Phys. Rev. Lett.*, 102:205501, 2009.

- [38] A. Chuvilin, J. C. Meyer, G. Algara-Siller, and U. Kaiser. From graphene constrictions to single carbon chains. *New J. Phys.*, 11:83019, 2009.
- [39] E. Erdogan, I. Popov, C. G. Rocha, G. Cuniberti, S. Roche, and G. Seifert. Engineering carbon chains from mechanically stretched graphene-based materials. *Phys. Rev. B - Condens. Matter Mater. Phys.*, 83:41401, 2011.
- [40] M. Topsakal and S. Ciraci. Elastic and plastic deformation of graphene, silicene, and boron nitride honeycomb nanoribbons under uniaxial tension: A first-principles density-functional theory study. *Phys. Rev. B - Condens. Matter Mater. Phys.*, 81:24107, 2010.
- [41] H. W. C. Postma. Rapid Sequencing of Individual DNA Molecules in Graphene Nanogaps. *Nano Lett.*, 10:420–425, 2010.

# A

## APPENDIX DIFFUSION OF CO ADATOMS

### A1. 1D RANDOM WALK PROBABILITY DISTRIBUTION FOR CO ON GNR

We assume that an atom makes only nearest-neighbor jumps between sites arranged along a line, and motion to the right or to the left is equally probable and occurs at random moments in time. The probability  $P$  of an atom, initially at position  $x = 0$  at time  $t = 0$  to be at lattice site  $x$  at time  $t$  is given by<sup>1</sup>

$$P_x(v) = Ae^{-2vt} I_x(2vt) \quad (\text{A.1})$$

where  $A$  is the prefactor,  $v$  is the hopping rate and  $I_x$  modified Bessel function of the first order

$$I_x(a) = \sum_{i=0}^{\infty} \frac{1}{i!(i+k)!} \left(\frac{a}{2}\right)^{2i+x}. \quad (\text{A.2})$$

As time  $t$  we take the average duration of the voltage pulse (0.5 sec).

---

<sup>1</sup>J. D. Wrigley *et al.*, Lattice walks by long jumps, J. Chem. Phys. 93, 2885 (1990)

## A2. 2D RANDOM WALK PROBABILITY DISTRIBUTION FOR CO ON AU

The top image in Figure A.1 shows hollow sites on Au(111) which are presumably preferential spots for Co adatoms. The black dot in the center indicates the initial Co position (no displacement), red dots indicate 2<sup>nd</sup>- nearest-neighbor displacement, brown dots indicate 4<sup>th</sup>- nearest-neighbor displacement and so on. The two nearest hollow sites are 1.7 Å apart, which is at the limit of our resolution. In order to simplify the description, we remove half of the hollow lattice sites (small white circles) and introduce two non-orthogonal axes (bottom image). Each hollow site corresponds to a displacement  $d$  and is labeled with a pair of indices, (x,y). Colors indicate category of displacement  $d$  and shade indicates different distances from the initial position (black dot in the center) for a given  $d$ .

For the two-dimensional random walk on a triangular grid the average number of image-to-image diffusion steps for each of the two dimensions is  $\nu t/2$ , where  $\nu$  is the total hopping rate for all four directions. The probability distribution for finding the adsorbate displaced in each of the directions by  $x$  and  $y$  lattice sites is given by<sup>2</sup>

$$P_{xy} = e^{-\bar{N}} I_x\left(\frac{\bar{N}}{2}\right) I_y\left(\frac{\bar{N}}{2}\right) = e^{-\nu t} I_x\left(\frac{\nu t}{2}\right) I_y\left(\frac{\nu t}{2}\right) \quad (\text{A.3})$$

where  $I_x$ ,  $I_y$  are modified Bessel functions of the first order. We calculate the probability for each  $L$  as the sum of all probabilities of the displacements  $d$  (none, 1<sup>st</sup> nearest-neighbor, 2<sup>nd</sup> nearest-neighbor...) of that length  $L$ . For example, the expected probability for Co to be displaced by 0.6 nm is equal to

$$\begin{aligned} P_{L=0.6}(\nu) &= P_{1,-1} + P_{-1,1} + P_{0,2} + P_{0,-2} + P_{2,0} + P_{-2,0} + \\ &+ P_{1,2} + P_{2,1} + P_{-2,-1} + P_{-1,-2} + P_{2,2} + P_{-2,-2} = \\ &= e^{-\nu t} \left[ 2I_{\frac{1}{2}} I_{\frac{1}{2}} + 4I_0 I_1 + 4I_{\frac{1}{2}} I_1 + 2I_1 I_1 \right] \end{aligned} \quad (\text{A.4})$$

This is also illustrated in the table in the lower panel of Figure A.1. As mentioned in subsection 2.8.3, each  $L$  corresponds to a 0.3 nm wide set of values (e.g.  $L = 0.6$  nm takes all values from 0.45 to 0.75 nm). Because of the freely chosen range of data sets, some histogram peaks might be significantly higher/lower than the neighboring ones due to encompassing more/less data points. This explains the sudden drop of the fitted value of probability in Figure 2.28 at 1.2 nm.

<sup>2</sup>J. D. Wrigley *et al.*, Lattice walks by long jumps, J. Chem. Phys. 93, 2885 (1990)

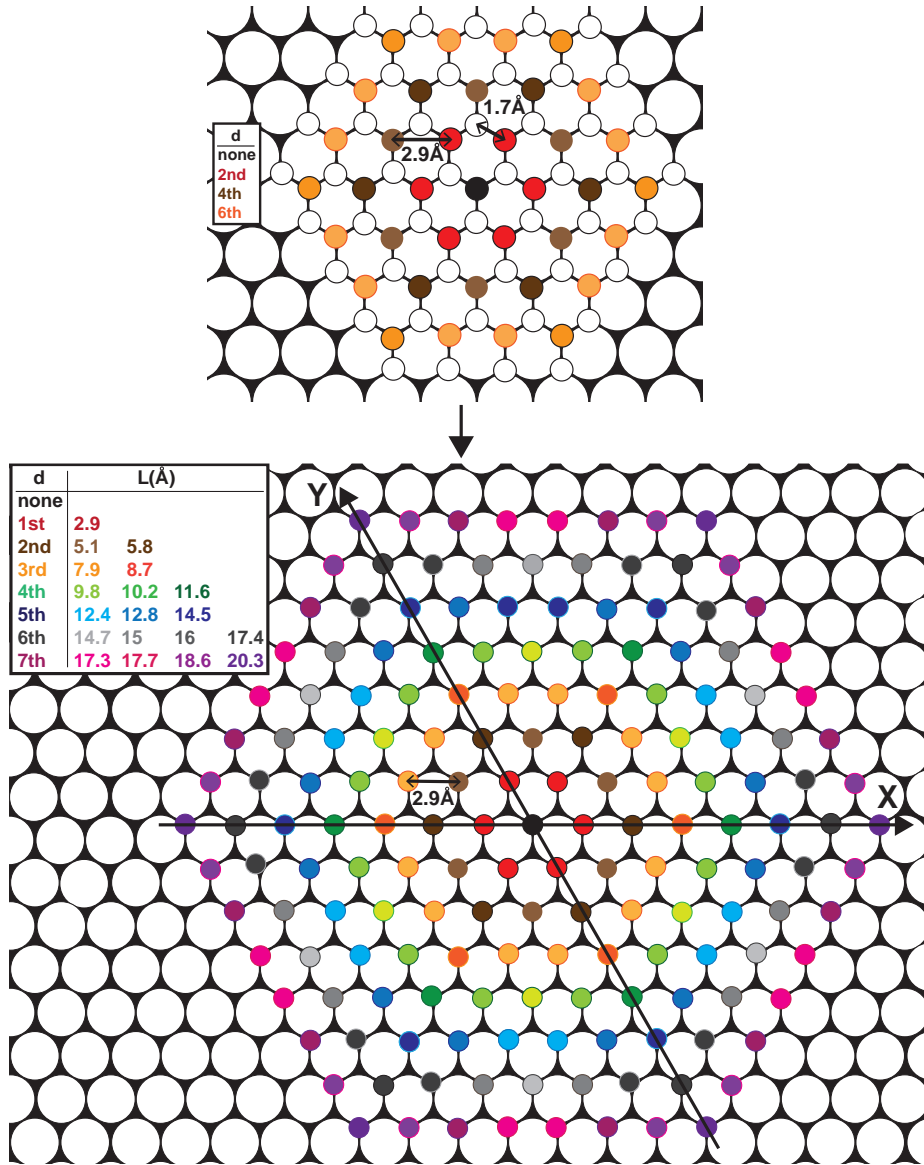


Figure A.1: **Possible displacements for Co on Au(111)**. Top image shows available hollow sites (small circles) which form a hexagonal lattice. The colors indicate the displacement  $d$  (none, 1<sup>st</sup>, 2<sup>nd</sup>...) from the initial position (black circle in the middle). Small white circles indicate sites that cannot be resolved with our resolution. After removing these sites a trigonal lattice is obtained (bottom image). Different color shades indicate different distances from the initial site (black circle) for the same displacement number. The black dot in the center indicates the initial Co position.



# B

## APPENDIX GRAPHENE ELECTRODES

### B1. SIMMONS MODEL FOR SYMMETRIC BARRIER

Considering tunneling through a symmetric barrier, we can approximate the work function  $\phi$  to be the same for both electrodes. The current density in a symmetric tunnel junction with a barrier along the  $z$ -axis (Figure B.1) is described by the Simmons model <sup>1</sup>:

$$J \sim \frac{e}{2\pi\hbar z^2} \left[ (\phi - \mu_L) e^{-\frac{4\pi z \sqrt{2m(\phi - \mu_L)}}{\hbar}} - (\phi - \mu_R) e^{-\frac{4\pi z \sqrt{2m(\phi - \mu_R)}}{\hbar}} \right] \quad (\text{B.1})$$

where  $z = z_1 - z_2$  is the gap size, and  $\mu_L, \mu_R$  are the chemical potentials of the left and the right electrodes, respectively.

Parameters fitted to the Simmons model are the pre-factor  $A$  (which contains the cross-section of the junction), the barrier height  $\phi$  and the gap size  $z$ . The parameters  $A$  and  $\phi$  cannot be fitted completely independently, but with a suitable choice for the pre-factor the barrier height obtained is in agreement with the range of results found in the literature, see the main text. The gap distance  $d$  is more robust and it is estimated with approximately 5% accuracy.

---

<sup>1</sup> J. G. Simmons. Generalized formula for the electric tunnel effect between similar electrodes separated by a thin insulating film. *J. Appl. Phys.*, 34: 1793-1803, 1963.

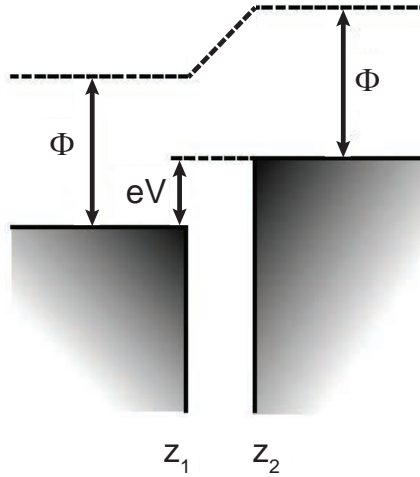


Figure B.1: **Symmetric tunnel junction with barrier height  $\phi$  and barrier width  $d = z_1 - z_2$ .**

## B2. GRAPHENE-GOLD TUNNEL JUNCTION

In order to identify the edge electrodes that extend to the end of their supports, we formed a tunneling junction against a gold sample. This, in first instance, allows easier electrical characterization of the edge electrode and secondly demonstrates the flexibility of our system, capable of employing independent edge electrodes in multiple systems, either symmetric or asymmetric junctions.

Figure B.2(a) illustrates the schematics of the set-up. The graphene edge electrode is mounted on a holder over a piezoelectric actuator (thick grey block on the left) which approaches a thick sample of pure gold. Figure B.2(b) shows the  $I(V)$  tunneling characteristic of the tunnel junction at a fixed distance, sweeping the bias voltage  $V$  between  $-1.5$  V and  $+1.5$  V. The shape of the sigmoidal  $IV$  curve is characteristic of an asymmetric tunneling barrier. This is a result of the different work functions across the two terminals of the junction. Figure B.2(c) shows the tunneling current as a function of distance (black curve,  $I(z)$ ) between the graphene and the gold sample at  $V = 0.48$  V bias voltage. We observe a clear exponential increase (exponential fit red curve) of the current with decreased distance, characteristic of a tunneling regime.

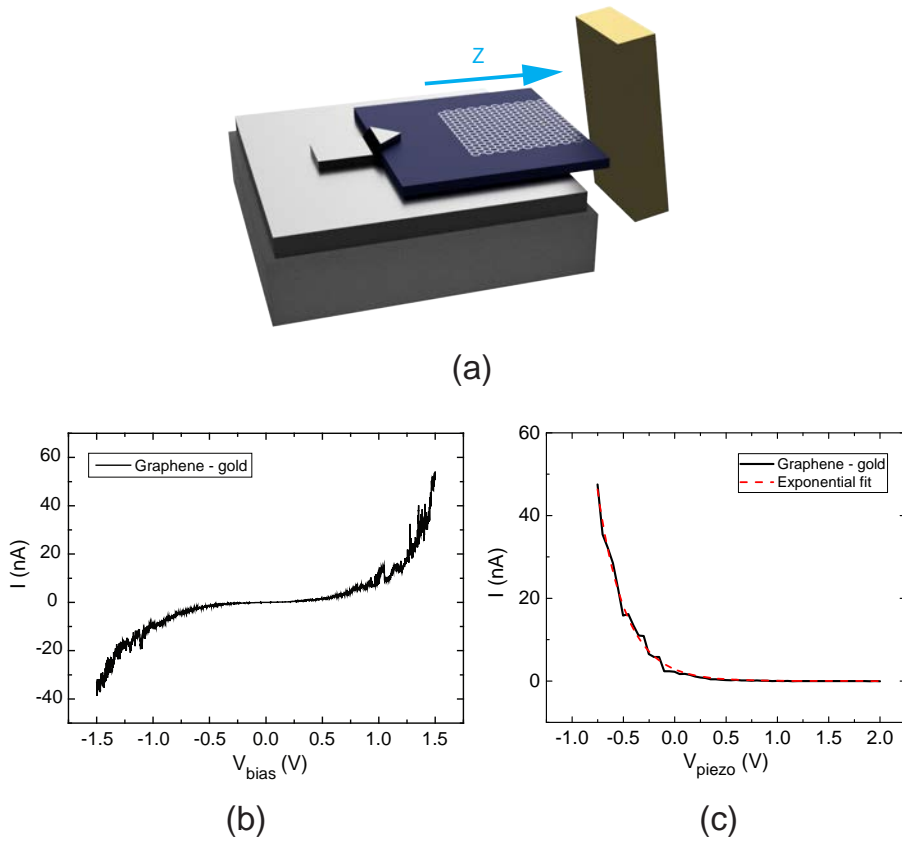


Figure B.2: **Gold-graphene tunnel junction.** (a) Schematics of the gold – graphene tunnel junction. The graphene electrode is mounted on a piezoelectric actuator which moves the sample along the Z axis to approach a gold macro electrode. (b) IV characteristic of the graphene-gold junction. (c) Representative  $I(z)$  characteristic of graphene-gold tunnel junction (black line) fitted to exponential function (red line).

### B3. TUNNELING JUNCTION CONTROLLER

The two graphene sheets are mounted on sample stages at the positions of “sample” and “tip” of an STM scanner. A description of the scanner can be found in PhD dissertation of S. Otte <sup>2</sup>. Graphene was contacted electrically by a drop of silver paint embedding a copper wire attached to the sample stage. A RHK SPM-100 controller was used to supply bias voltage between the samples, as well as the high voltage for Z piezo element that is moving one of the supports. The tunneling current flowing across the junction was amplified using a FEMTO DLPCA-200 current amplifier. The XY motion was controlled by a second piezo element underneath the other support. The voltage applied to the XY piezo element was kept constant during  $I(z)$  and IV measurements.

### B4. SHEET RESISTANCE AND POINT CONTACT RESISTANCE

In contrast to 3D metallic systems the point contact resistance measured here has a large contribution from the sheet resistance of the graphene electrodes that cannot be separated from the measurements. The total measured resistance is the quantum point contact resistance,  $R_{pc}$ , in series with the classical resistance of the sheets,  $R_g$ . The classical resistance  $R_g$  of the sheets on either side of the contact can be estimated as

$$R_g = \frac{1}{\pi\sigma} \int_{l_0}^L \frac{1}{r} dr \quad (\text{B.2})$$

where  $\sigma$  is the sheet conductance,  $L$  is the size of the graphene sample (2 mm), and  $l_0$  is the electron mean free path. Using the semi-classical expression for the sheet conductance:

$$\sigma = \frac{e^2}{h} \frac{2E_F\tau}{\hbar} \quad (\text{B.3})$$

and the linear dispersion of the Fermi energy  $E_f = \hbar v_F k_F$ , and  $k_F = \sqrt{\pi n}$ , we can express the mean free path in terms of the conductivity and the electron density:

$$l_0 = \frac{\sigma}{\frac{e^2}{h}} \frac{1}{2\sqrt{\pi n}} \quad (\text{B.4})$$

Using the conductance of  $\sigma = (11 \pm 2) \frac{e^2}{h}$  found for our samples, and the typical dependence between charge density and conductance in this regime <sup>3,4</sup> we obtain an estimate of  $l_0 = 27$  nm. With this we arrive at an estimated resistance for the sum of the two graphene electrodes of  $17 \pm 3$  k $\Omega$ . Subtracting this value from the measured

<sup>2</sup> S. Otte. Magnetism of a single atom. *PhD thesis*, 2008

<sup>3</sup> K. S. Novoselov, A. K. Geim, S. V. Morozov, D. Jiang, M. I. Katsnelson, I. V. Grigorieva, S. V. Dubonos, A. A. Firsov. Two-Dimensional gas of massless Dirac fermions in graphene. *Nature*, 438: 197-200, 2005

<sup>4</sup> E. H. Hwang, S. Adam, S. Das Sarma. Carrier transport in two-dimensional graphene Layers. *Phys. Rev. Lett.*, 98:186806, 2007.

point contact resistance of  $28 \text{ k}\Omega$ , we find an estimate for the quantum point contact resistance of:

$$R_{\text{qpc}} = R_{\text{total}} - R_{2\text{g}} = 11 \pm 3 \text{ k}\Omega \quad (\text{B.5})$$

# SUMMARY

The initial motivation and the main aim of our research was to investigate electromigration at the atomic scale (**Chapter 2**). Knowledge gained from such experiments would give clues to many unanswered questions about current-induced forces. Graphene on an insulating substrate was the first system to be investigated since the current would be confined within an atomic layer. Electromigration would be observable by the current-induced motion of individual adatoms deposited on the surface, which can be imaged by scanning tunneling microscopy (STM). We used graphene on Si/SiO<sub>2</sub> and that comes with a few limitations that prevented us from observing migration of adatoms with the current densities achievable in our STM. Graphene nanoribbons (GNR) proved to be a good alternative to graphene, although the underlying substrate is conducting and current is not confined within the GNR. We used armchair graphene nanoribbons grown on Au(111), and on top of this substrate we evaporated cobalt atoms. Using an STM tip to send a voltage pulse while in contact with a GNR, we induced one-dimensional motion of Co adatoms on the GNR. We did not observe directional motion of the adatoms which would indicate the presence of current-induced forces, most likely because the current density along the GNR was too small. These results suggest that migration of Co on GNR mainly comes from thermal activation. Temperature-dependent diffusion measurements gave us information on the relative energy barriers for Co adatoms on gold and on GNRs. We expect that current-induced motion can be observed and quantified by this method if most of the GNR's length can be separated from the substrate by an insulating layer.

The study of electromigration is also the subject of the second part of the research presented in this thesis (**Chapter 3**). The recent observation<sup>5</sup> that dragging a droplet along a strip of graphene induces a voltage across the ends of this strip, inspired us to ask the following question: would it be possible to do the opposite and induce motion of the droplet by applying a voltage across the graphene strip? Our experiments have shown that it is, in fact, not possible to do this. In order to understand the role of the adsorption of ions, formation of an electric double layer and the formation of a pseudocapacitor, we investigated several different ionic liquids. Results for an aqueous solution of NaCl showed that the voltage signal is linearly dependent on the speed of the droplet, and that the sign of the voltage depends on the direction of the droplet motion. We also observed that the voltage signal, induced by moving a droplet of 0.01 M concentration, is larger than the signal for an ion concentration of

---

<sup>5</sup> Yin *et al.*, Nature Nanotechnology, **9**, 378 (2014)

0.6 M. Furthermore, we utilized ionic liquids which we assumed will bond strongly to graphene and the underlying polyethylene terephthalate (PET) substrate: sodium benzenesulfonate and benzenesulfonic acid. This led to an interesting discovery: a droplet of distilled water, when moved along the graphene surface after having used these ionic liquids, also induces a voltage. This was an indication that certain types of ions adhere so strongly to graphene that they leave the droplet and form a charged layer on graphene. We concluded that the polarizability of water has a contribution to the voltage signal almost as large as ionic liquids, when moved over such a charged graphene surface.

As it often happens when doing scientific research, looking into certain problems sometimes leads to gaining knowledge (and interest) in concepts that are far from the initial objective. After doing many experiments with graphene, we were motivated to take it a step further and attempt to design atomically thin nanoelectrodes by means of a reproducible and reliable fabrication method. This project, described in **Chapter 4**, was particularly attractive, having a prospect for applications such as electron-transport measurements on single molecules and sequencing of biopolymers. We present a few possible methods for creating graphene electrodes on Si/SiO<sub>2</sub>: the *broken-graphene* and the *etched-graphene* method. While the broken graphene method did not yield usable graphene nanoelectrodes with full graphene coverage up to the edge of the substrate, the etched graphene approach was very successful. All techniques used to characterize etched graphene edges (Raman spectroscopy, SEM, AFM and electrical measurements) unanimously confirmed that graphene reaches up to the edge within respective resolutions of each of the techniques. Using a modified STM and a twisted-sample approach, we have created the first tunable tunneling nanogap between graphene-edge electrodes. By pushing the electrodes closer together, we have been able to form an atomic sized junction between the two edges of graphene.

# SAMENVATTING

De voornaamste beweegredenen en het voornaamste doel van ons onderzoek was om electromigratie op atomaire schaal te begrijpen (**Hoofdstuk 2**). De met deze experimenten verkregen kennis zou aanwijzingen kunnen geven op onbeantwoorde vragen over stroom-geïnduceerde krachten. Grafeen op een isolerend substraat was de eerste keuze voor dit onderzoek, aangezien daarin de stroom geconcentreerd blijft in één enkele laag atomen. Electromigratie zou waargenomen kunnen worden door middel van de stroom-geïnduceerde beweging van individuele adatomen, die zijn gedeponeerd op het oppervlak, hetgeen te zien zou moeten zijn met behulp van een scanning tunneling microscoop (STM). Grafeen op Si/SiO<sub>2</sub> had echter een aantal nadelen die ons belemmerden om de electromigratie van adatomen op het oppervlak waar te nemen bij de stromen die we konden maken met de STM. Grafeen nano-'lintjes' (Graphene nanoribbons, GNR) daarentegen, bleken een goed alternatief te zijn voor grafeen, alhoewel het onderliggende substraat geleidend was en daarmee de stroom niet slechts beperkt bleef tot de GNR. We hebben armchair GNRs gegroeid op Au(111), waarop we cobalt atomen opdampten. Door de naald van de STM te gebruiken om een spanningspuls te sturen terwijl deze in contact is met de GNR, hebben we een één-dimensionale migratie van Co adatomen bewerkstelligd op de GNRs. We hebben geen migratie gezien van adatomen in een specifieke richting, wat zou duiden op stroom-geïnduceerde krachten. Dit komt waarschijnlijk door te lage stroomdichtheden. De resultaten laten zien dat de migratie van Co op de GNR voornamelijk wordt veroorzaakt door thermische activatie. Temperatuurafhankelijke diffusiemetingen hebben ons inzicht gegeven in de relatieve energiebarrières voor Co adatomen op goud en GNR's. Wij verwachten dat met behulp van deze methode stroom-geïnduceerde beweging kan worden waargenomen en gekwantificeerd wanneer de GNR gedeeltelijk gescheiden kan worden van het substraat door een isolerende laag.

Het onderzoek naar electromigratie was ook de motivatie voor het tweede deel van het onderzoek dat in dit proefschrift wordt gepresenteerd (**Hoofdstuk 3**). De recente observatie dat het slepen van een druppel over een strook grafeen een spanning induceert over de uiteinden van de strook, heeft ons geïnspireerd om de volgende vraag te stellen: is het mogelijk om het tegenovergestelde te doen? Experimenten laten zien dat het niet mogelijk is om een druppel te laten bewegen door een spanning aan te leggen over de uiteinden van een strook grafeen. Om de rol van de ionenadsorptie, formatie van een elektrische dubbellaag en formatie van een pseudocondensator te begrijpen, hebben we een aantal ionische vloeistoffen onderzocht. De resultaten voor een waterige NaCl oplossing heeft ons laten zien dat het

spanningssignaal lineair afhankelijk is van de verplaatsings-snelheid van de druppel. Ook is het teken van het spanningssignaal afhankelijk van de richting waarin de druppel zich beweegt. We hebben ook gezien dat het geïnduceerde spanningssignaal door een bewegende druppel groter is bij een 0.01 M concentratie dan bij een 0.6 M concentratie. Daarnaast hebben we gebruik gemaakt van ionische vloeistoffen waarvan we kunnen aannemen dat deze sterk kunnen binden aan grafeen/PET: natriumbenzeensulfonaat en benzeensulfonzuur. Dit leidde tot de interessante ontdekking, dat na het gebruik van deze ionische vloeistoffen op het grafeen, we een geïnduceerde spanning vonden wanneer een druppel gedistilleerd water over het grafeen wordt verplaatst. Dit was een indicatie dat bepaalde types ionen zich zodanig sterk binden aan het oppervlak dat ze de ionische druppel verlaten en een geladen laag vormen op grafeen. We concludeerden dat de polariseerbaarheid van water een bijdrage geeft aan het spanningssignaal, die bijna zo groot is als dat ten gevolge van ionische vloeistoffen, wanneer de waterdruppel over een geladen grafeenoppervlak wordt bewogen.

Zoals vaak het geval is in wetenschappelijk onderzoek, ontstaat er kennis (en interesse) in onderwerpen die zich ver van het initiële onderwerp bevinden. Na het uitvoeren van tal van experimenten op grafeen, waren we klaar om een volgende stap te zetten en te proberen atomair dunne nanoelectrodes te ontwerpen met een reproduceerbare en betrouwbare fabricatiemethode. Dit project, beschreven in **Hoofdstuk 4**, was in het bijzonder aantrekkelijk omdat het perspectief biedt op toepassingen, zoals electrontransportmetingen op enkele moleculen en het uitlezen van de bouwsteenvolgorde van biopolymeren. We presenteren een aantal mogelijke methodes for het maken van grafeenelectrodes op Si/SiO<sub>2</sub>: de gebroken grafeen- en de geëtste grafeenmethode. Terwijl de gebroken grafeenmethode onbruikbare resultaten gaf, was de geëtste grafeenmethode erg succesvol. Alle technieken die gebruikt worden om geëtste grafeenranden te karakteriseren (Raman-spectroscopie, SEM, AFM en elektronische metingen) bevestigden unaniem dat het grafeen tot aan de rand komt binnen de respectievelijke resoluties van elk van de gebruikte technieken. Door gebruik te maken van een gemodificeerde STM en positionering van de grafeen preparaten onder een kleine hoek, hebben we de eerste instelbare tunneljunctie gerealiseerd tussen twee grafeenrandelectrodes. Door de electrodes dichter naar elkaar toe te brengen, zijn we erin geslaagd om een brug te vormen ter grootte van een enkel atoom tussen de twee randen van grafeen.

# CURRICULUM VITAE

## Sasha VRBICA

- 17-06-1986 Born in Belgrade, Serbia
- 2000 – 2004 5th Gymnasium  
Belgrade, Serbia
- 2004 – 2011 BSc. in Theoretical Physics  
Faculty of Physics, Belgrade, Serbia
- 2011 – 2012 MSc. in Experimental Physics  
Institute of Physics, Center for Solid State Physics, Belgrade, Serbia  
*Thesis:* Study of vibrational characteristics of CeO<sub>2</sub> nanocrystals  
*Supervisor:* Prof. Dr. Zoran V. Popović
- 2013 – 2018 PhD in Experimental Physics  
Leiden University, Leiden, The Netherlands  
*Thesis:* Applications of Graphene in Nanotechnology – 1D  
diffusion, Current drag and Nanoelectrodes  
*Supervisor:* Prof. dr. Jan M. van Ruitenbeek

# LIST OF PUBLICATIONS

1. A. Bellunato\*, **S. Vrbica**\*, C. Sabater, E. W. de Vos, R. Fermin, K. N. Kannevorff, F. Galli, J. M. van Ruitenbeek and G. F. Schneider, *Dynamic tunneling junctions at the atomic intersection of two twisted graphene edges*, *Nano Lett.* **18**, 4, 2505-2510 (2018).

\*These authors contributed equally to this work

2. **S. Vrbica**, T. Preis, N. Kocić, J. Repp and J. M. van Ruitenbeek, *One-dimensional diffusion of Co adatoms on graphene nanoribbons*, to be submitted.
3. **S. Vrbica**, T. Vlot and J. M. van Ruitenbeek, *Inducing voltage by moving a droplet of liquid along graphene*, to be submitted.

## Patent applications

1. G. F. Schneider, J. M. van Ruitenbeek, A. Bellunato, **S. Vrbica**, C. Sabater, E. de Vos. *Method of preparing two-dimensional electrically conductive material having atomically sharp supported edges*. Patent application GB 1610187.5

# ACKNOWLEDGEMENTS

I would need to write another book to properly thank all the people who were there for me during these past few years. It was challenging for me to start a new life far from everyone I knew, but you all made it so easy and so wonderful. I will cherish my PhD time in Leiden and remember it with a smile.

First and foremost, I would like to thank the most inspirational, enthusiastic and creative professor that I have come across in my lifetime: Jan van Ruitenbeek. Jan, you were always supportive, open for suggestions, available for discussions and always leaving room for creativity. Your endless patience, wisdom and enthusiasm, along with a great sense of humor motivated me to go the extra mile, every day. You taught me so much about research in general, about how to approach problems, how to remain calm and patient when facing challenges and how to make the best out of every situation. I still have a lot to learn but now I am confident I will do it much faster and better, all as a result of your guidance.

I would like to express my sincere gratitude to all our collaborators. Sander Otte, Ranko Tošković and Marnix Rebergen, thank you for giving me the opportunity to do an experiment in your lab in Delft. It was short but memorable experience. Not only did I learn a lot about STM in those few weeks, but your group created such a wonderful atmosphere that it made all the hard work very enjoyable. Amedeo Bellunato and Grégory Schneider, thank you for a very successful collaboration. I always believed that bringing chemistry and physics together is bound to offer not only interesting possibilities for experiments but also a higher chance for a good outcome. To Jascha Repp, Tobias Preis, Nemanja Kocić and all the others, I cannot thank you enough for giving me a wonderful opportunity to work in your lab in Regensburg. For a couple of months you made me feel like I was a part of your group. I enjoyed every minute of our discussions and experiments, as well as all the laughs at coffee breaks. Working in your lab is an experience that I will never forget.

I had the good fortune to cross paths with Federica Galli and Marcel Hesselberth, two people without whom I would not have gotten this far. Your vast knowledge and expertise on pretty much every subject (scientific or otherwise), mixed with a lot of humor and willingness to teach, made it an absolute pleasure to work with you. Thank you for your guidance, for all the discussions, tutoring, crisis averting (even on weekends) and for all the fun times we had. You made my research more adventurous, you challenged me to do my best and every day you made me feel like I was not far away from home.

I owe a big thank you to Elena Tartaglini for generously offering me her time and expertise in the first weeks of my PhD. It would have been a real struggle without her

help. Christian Pen, your amazing ideas, skills and experience accompanied by quick thinking and readiness to help as efficiently as possible made my research much easier and much more pleasant. Without your expertise my results would not have been half as good as they are now. To everyone in the fine mechanical department, you met all my urgent requests (even on Friday afternoons) and you always brought a good mood along with great ideas, thank you for that! Peter van Veldhuizen, Bert Crama and the rest of the electronics department, thank you for all your efforts and for always helping me out with a smile. Marije Boonstra, thank you for so many well-organized events, conferences and workshops and for always finding a solution when I would come with a problem. Wilfred van der Geest, you were always there to help out with whatever needed fixing or solving, it was very helpful knowing that everything can easily be sorted out when you are around. Ellie van Rijsewijk, Charlotte Laurensse-Griffoen, Ruud Kuyvenhoven, Erik van de Kraan, Annette Bor and the rest of the staff of Leiden University and NWO, I owe you all a big thank you for your professionalism, efficiency and, all-in-all, for making my PhD much less stressful than it would otherwise have been.

I would like to thank all my students Irene, Kim, Eric, Remko, Kirsten, Theo, Jurrien and David, I truly enjoyed working with you. You made me a better teacher and I hope that, in return, I managed to spark your interest in science. Peter Gast, thank you for all your help with my teaching-assistant duties, it was enjoyable working as a TA with you. Kaveh Lahabi and Daniël Geelen, you already know everything. Just keep swimming! Carlos, it was a pleasure having you as a post doc in our group. I wish you and Mary a lot of luck with your future research and hope our paths will cross again in the future. I would like to thank Sense Jan van der Molen and Jan Aarts for all the interesting group discussions during the early stages of my PhD. I also thank Eric Eliel for his feedback and for regularly bringing my attention to useful workshops and scientific events.

My PhD days would have been bland if not for the wonderful people who were always there to brighten the day: Hasan & Huseyin, Edwin, Sumit, Tobias, Victor, Jaco, Jacob, Julian, Mike, Remco, Alexander, Daan, Anikitkat, Jaap, Jo, Vera, Chunhai, Nikita, Stefano, Luigi, Lucia, Jelmer, Gesa, Arthur, Doo, Koen, Marc, Martin, Tom, Amrita, Christian Glass, Christian Wagner, Anne France, Douwe, Timothy, Thomas, Manohar, Chris Smiet, Flavio, Biswajit, Saptaswa, Kirsten, Oliver, Jimmy, Morten, B, Pauline, Kier, Tjerk, Milan, Marcel Rost, Davide, Ignacio and many others. I will always treasure the days I spent with you in the lab, at conferences, courses and outside of work.

I would also like to thank three persons who are very special to me, my elementary school teacher Prof. Nedović, who first sparked my interest in math, and my high school professors Tanja Munižaba and Dinka Todorović. Tanja, you have given me the freedom to express my creativity, and the courage to pursue my dreams, I cannot thank you enough for that. Dinka, you are the reason why I decided to study experimental physics and why I am defending my doctorate today. Your optimism,

passion for physics, patience and willingness to share all your knowledge is what defined my life path. I would not have done any of this without you. Thank you.

I am thankful to all my Balkan PhD friends in the Netherlands: Stefan, Markeša, Marija Mučibabić, Ranko, Dejan, Darko, Miloš Birvalski, Zoki and Marina, Onder and Tanja, you all deserve pages of gratitude each. Thank you for keeping my spirits up. I enjoyed exchanging scientific knowledge and anecdotes with you, as well as Serbian humor and life stories. I wish you all a lot of success in your scientific careers and all your future endeavors. I also thank my friends in Serbia for believing in me and being there for me for more than a decade.

Lastly, I would like to thank the people closest to me, my family. Mama, tata, bako, thank you for all the effort, patience, advice, care, understanding and smiles. Grey sky always looks brighter because you are always with me. To my twin Pajce, my brother in arms, thank you for always being there for me, from day one, and for helping me through all my ups and downs. Good luck with your biology research. I hope you will get to experience the same joy and excitement that I experienced during my PhD. Vladi and Pitri, thank you for being a part of my life (Pitri, I hope you will choose physics over biology as your career when you grow up!)

Asuna, you light up the path you walk on and I was lucky to walk by your side all these years. Thank you for standing by me when I was facing challenges, and for helping me thrive in everything I do. As we now continue our adventure down the road less traveled by, I am excited to see where it will take us!

